The generation and manipulation of low energy positron beams.

Clarke, Jonathan

THE GENERATION AND MANIPULATION OF LOW ENERGY POSITRON BEAMS

by

Jonathan Clarke

MPhys (Hons) (Swansea)

Submitted to the University of Wales in fulfilment of the requirements for the Degree of Doctor of Philosophy

University of Wales Swansea

2005

ProQuest LLC.
789 East Eisenhower Parkway
P.O. Box 1346
Ann Arbor, MI 48106 – 1346

Abstract

A laboratory based low energy positron beamline has been constructed and tested. The techniques underlying this device are described, as are modifications and improvements which were made to the conventional operation of such apparatus. The use of this beamline in conjunction with a novel positron accumulator using a two-stage buffer gas cooling method is discussed. Its ability to operate in the 1 – 10 Hz range, providing bursts of ~ 10^5 positrons with a time width of ~ 20 ns is described. The deviation from the expected ideal behaviour of this accumulator is recorded, and the efficacy of this departure in detecting performance problems presented. A number of applications of the positron apparatus are described. A series of simulations on a positron time-bunching apparatus are expounded. Agreement with the observed timing resolution was found only when non-ideal processes occurring within the device were considered. Suggestions towards possible optimization of these non-ideal processes to further improve the timing resolution of such an apparatus are put forward.

DECLARATION

This work has not previously been accepted in substance for any degree and is not being concurrently submitted in candidature for any degree.

Signed ..... (candidate)

Date ..... 1/9/05 .....

STATEMENT 1

This thesis is the result of my own investigations, except where otherwise stated.

Other sources are acknowledged by footnotes giving explicit references. A bibliography is appended.

Signed ..... (candidate)

Date ..... 1/9/05 .....

STATEMENT 2

I hereby give consent for my thesis, if accepted, to be available for photocopying and for inter-library loan, and for the title and summary to be made available to outside organisations.

Signed ..... (candidate)

Date ..... 1/9/05 .....

Contents List

List of Figures

List of Tables

Acknowledgements

The author wishes to thank the staff of the following institutions for helping him to get where he is today, namely St. Thomas Primary School (1983 - 1990), Cefn Hengoed Community School (1990 - 1995), Swansea College (1995 - 1997), and of course, the University of Wales Swansea (1997 - 2005). He offers particular thanks to Professor Michael Charlton, Dr. Dirk Peter van der Werf, Professor Helmut Telle, Dr. David Beddows, Julian Kivell, Hugh Thomas, Ben Griffiths, Peter Watkeys and Daniel Mitchard for their help in his PhD.

He also thanks his family, for their love and support, without which he would not have been able to accomplish the goals that he has.

To

Helen Ceri, Mitzi, Molly, and Shirley

"Everything in moderation, including moderation."

- Harvey Steiman

One of the major fields of physics in the twenty-first century seems set to be the further study of anti-matter. Advances in the latter decades of the twentieth century made it possible for the first anti-atoms to be produced, in sufficient quantities for detailed investigation to be carried out regarding the difference (if any) of the structure and behaviour of matter and anti-matter. This knowledge has great relevance when attempting to explain behaviour in the early universe, and how it shaped the universe we see today. Observations imply that the local part of the cosmos is matter-dominated, and it seems unlikely that large amounts of anti-matter could have distanced themselves from quantities of matter quickly enough within the early universe to prevent mutual annihilation, and form anti-matter dominated regions of the cosmos today. This implies that the matter dominance we observe today may extend further across the cosmos, and hints at the presence of a small imbalance in quantities of matter and anti-matter within the early universe, which produced the conditions we see today via mutual annihilation.

The positron stands as the true forerunner in the anti-matter field, it being the first anti-particle to be proposed, detected, and subsequently harnessed for use in science and technology. Due to its low mass, it is relatively easy to produce, and thus has played a major role in the study of anti-matter to this day, and this will no doubt remain true for the future. It is therefore vitally important that positron research continues, and apparatus used to produce and utilize this particle be developed and improved. It is with this aim in mind that the work in this thesis is presented.

The existence of the positron, the anti-matter equivalent of the electron, was postulated by Dirac (1930), who proposed that the negative energy solutions to his

theory of the electron had physical relevance. This conjecture was validated when the positron was discovered by Anderson (1933), during his cloud-chamber experiments. This discovery was confirmed by Blackett and Occhialini (1933), and the theory of the transformation of energy into matter was validated via observation of pair production. Thibaud (1933, 1934) and Joliot (1933, 1934) later independently showed the positron annihilated in the presence of matter. This annihilation event was studied by Klemperer (1934), who proved that two gamma rays were emitted in coincidence in approximately opposite directions.

Subsequent work by DeBenedetti and co-workers (1949, 1950) showed that the two gamma rays were not in fact emitted in opposite directions, as expected for a positron and electron at rest, and that the angle between them was determined by the motion of the bound electrons in the material within which the positron had annihilated. DuMond and co-workers (1949) also showed that the energy width of the annihilation gamma-ray line was larger than measurement resolution, which they attributed to Doppler broadening arising from electron motion in the material. These two discoveries constitute an important milestone in the history of the positron, for they suggested that the particle may be used as a tool to measure the internal characteristics of materials.

The quasi-stable bound state of a positron and an electron, namely positronium (Ps), proposed by Mohorovičić (1934), was discovered by Deutsch (1951a,b). Positronium has a vacuum binding energy of ~ 6.8 eV, and may exist in two distinct spin states, namely the singlet state para-positronium (p-Ps) where the spins of the electron and positron are antiparallel, and the triplet state ortho-positronium (o-Ps) where the spins are parallel. Para-positronium has a vacuum lifetime of ~ 125 ps, and decays predominantly into two gamma rays of energy ~ 511

keV. Ortho-positronium has a vacuum lifetime of ~ 142 ns, and decays in vacuum into three or more gamma rays. The number of gamma rays n_γ resulting from the annihilation of each positronium state is fixed by applying angular momentum conservation and CP (charge and parity) invariance (Yang 1950; Wolfenstein and Ravenhall 1952), such that

$$(-1)^{n_\gamma} = (-1)^{L+S}, \qquad (1.1)$$

where the positronium atom is in a state with orbital angular momentum L and spin S. Thus, the annihilation of ground state para-positronium ($L = S = 0$) must result in the emission of an even number of gamma rays, whilst the annihilation of ground state ortho-positronium ($L = 0$; $S = 1$) must result in an odd number of gamma rays being emitted. The annihilation of free positronium resulting in zero or one gamma ray being emitted is forbidden. Thus, in both o-Ps and p-Ps cases, annihilation proceeds in the most part via the lowest order process available (i.e. 2γ for p-Ps, and 3γ for o-Ps), though Matsumoto and co-workers (1996) have reported that the 5γ decay of ortho-positronium has been observed. The presence of the two lifetimes of positronium was discovered by Bell and Graham (1953), with the short mean lifetime attributed to p-Ps annihilation (or annihilation of free positrons), and the longer mean lifetime attributed to o-Ps annihilation.

The development of laboratory based low energy positron beam-lines was born with the discovery by Cherry (1958) that the irradiation of a chromium-on-mica surface by a ^{64}Cu beta particle spectrum resulted in the greater emission of positrons in the energy range 0 – 5 eV relative to equal ranges at higher energies. This conversion of high energy to low energy positrons, known as moderation, is now at

the heart of all low energy positron beam apparatus. The efficiency of conversion achieved by Cherry was ~ 10^{-8}, which was superseded by the smoked MgO positron moderator of Canter and co-workers (1972), which had a moderation efficiency of ~ 3 x 10^{-5}. The most efficient positron moderators currently in use are the rare gas solids [Mills and Gullikson (1986)], with thin films of solid neon boasting moderation efficiencies of ~ 10^{-2} [Khatri *et al.* 1990].

The developments made in the field of positron physics described above now allow for increasingly ambitious applications of the humble particle. These include: the accumulation of very large numbers of positrons within a multi-cell device, with the ultimate goal of producing a portable source of ~ 10^{15} particles [Surko and Greaves (2003)]; anti-matter wave interferometry with positronium, to study the gravitational force on a purely leptonic and anti-matter system [Oberthaler (2002)]; and Bose-Einstein condensation of positronium, and the stimulated emission of annihilation photons [Mills (2002)]. These follow goals already accomplished, such as the production of low energy anti-hydrogen atoms [Amoretti *et al.* (2002); Gabrielse *et al.* (2002)].

The generation of a laboratory based low energy positron beam will be further described in chapter 2, where specific characteristics of the apparatus developed at Swansea will be presented. An unexpected beam strength anomaly observed during the growth of a solid neon moderator will be reported in section 2.3.1, together with attempts to characterise its source. Though not entirely understood, this phenomenon is of particular interest with regards to possible future developments in positron moderation.

Due to the stochastic nature of the disintegration of the ^{22}Na radio-isotope used to produce the high energy beta spectrum to irradiate a moderator, the resulting

low energy beam is made up of positron particles spaced arbitrarily with respect to one another along the beam axis. If one requires a pulse of positrons with a narrow time width of ~ ns, it is necessary to 'time-bunch' the distribution of particles in flight. This process will be explained in chapter 3, with specific attention paid to the non-ideal characteristics that a time-bunching device may have, and how these affect its performance.

One may instead wish to collect the positrons as they enter a specific volume of the apparatus, and accumulate these particles to produce a dense ensemble, which may be subsequently used for further experimentation. An accumulation process to fulfil this will be described in chapter 4, as well as a novel innovation in the design and application of an accumulator device. A number of interesting observations made during device diagnostics will be presented.

Various applications of the positron beam and/or accumulator at Swansea will be presented in chapter 5, and a summary of the reported work will be offered in chapter 6. For further reading, reference should be made to Charlton and Humberston (2001) which gives an overview of the field of positron physics, Coleman (2000) which gives a review of positron beams and their applications, and Schultz and Lynn (1988) which details the interaction of positron beams with surfaces, thin films and interfaces.

2.1 Introductory Considerations

The radioactive decay of the sodium-22 isotope produces high-energy positrons (β^+) via the following process

$$^{22}\mathrm{Na} \rightarrow {}^{22}\mathrm{Ne}^{*} + \beta^{+} + \nu_e \rightarrow {}^{22}\mathrm{Ne} + \gamma . \qquad (2.1.1)$$

The energy of these particles spans the range $0 - 5 \times 10^5$ eV, which is not suitable for precise experimentation where near mono-energetic distributions are necessary. Thus, a process of energy moderation is required to minimise the β^+ energy distribution as far as possible.

The moderation process relies on the physical interactions which occur when a positron is incident upon materials with certain physical properties, as will be elucidated. High energy positrons implanted into a metallic sample will lose a large fraction of their energy via ionising collisions, with further interaction channels being available at low energies. This abundance of energy-loss opportunity results in thermalisation of the positrons within a few ps, and for a large percentage, eventual annihilation. However, any particles which diffuse to the surface of the metal within the mean lifetime of ~ 100 ps may be re-emitted.

The work function of any surface with regards to electrons (φ_-) or positrons (φ_+) may be written as

$$-\varphi_{\pm} = \mu_{\pm} \pm D , \qquad (2.1.2)$$

where μ represents the chemical potential experienced by the particle within the bulk of the material, via interactions with electrons and ion cores, and D represents the surface dipole potential, mostly due to the tailing off of the electron distribution away from the surface into the vacuum. It is this distribution which is responsible for φ_+ being negative for some metals. The main possible fates of a positron implanted into a metallic surface are presented in fig. 2.1.1, where the particle is either lost due to annihilation in the bulk of the material, trapped at the surface with thermal energy, or emitted from the surface as a free particle with energy equal to or greater than the positron work function, or bound to an electron as positronium.

Using these principles, samples such as tungsten have been used as positron

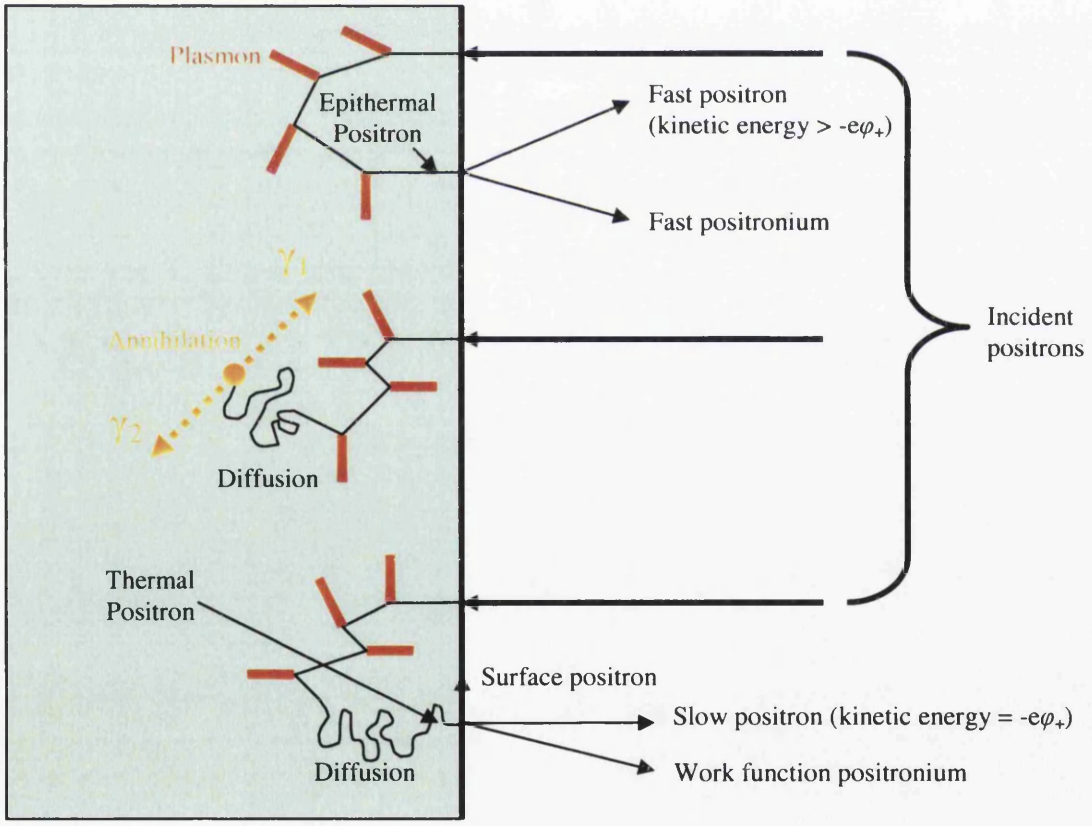

Figure 2.1.1: A schematic representation (after Mills 1983) of the main possible fates of a positron incident on a metallic surface: thermal emission, epithermal emission, annihilation, or surface trapping. Note that in the case of insulators, positrons lose energy via electron-hole pair creation, and phonon interaction.

moderators for many years, and indeed still are, due to their moderation efficiency of 10^{-3} – 10^{-4}, and relatively simple preparation and installation into laboratory based apparatus. However, these materials have been superseded by the rare gas solids (RGS), which have moderating efficiencies reaching 10^{-2} and above.

The application of a wide-band-gap insulator for this purpose initially seems counter-intuitive, for there are no free electrons near the surface of a RGS film, resulting in D being far smaller, and φ_+ being positive. However, at energies below that of the band gap, one cannot create electron-hole pairs within an insulator. Therefore, the energy loss mechanism in this energy range is solely mediated by the creation of acoustic phonons (a quantum of vibrational energy within a lattice) in the case of the rare gas solids, which differs from the case of metals, where the electron-hole pair excitation channel is available down to energies approaching zero. This makes it more likely for a positron to be of epithermal energy if it encounters a surface during its diffusion through the rare gas solid lattice. The concentration of electrons within a rare gas solid is small compared to metals, and as such, positron lifetimes within such solids are longer. This therefore translates to longer positron diffusion lengths within rare gas solids compared to metals, and a greater probability of a positron encountering a surface. This increased exposure of the surface to epithermal positrons results in the copious emission first seen by Mills and Gullikson (1986). Further improvements in the method have since been introduced, refining the geometry of the neon film [Khatri *et al.* 1990], as well as drift enhancement by applied electric fields [Merrison *et al.* 1992], as shown in Table 2.1.1. It should be noted that the moderator efficiencies presented are those quoted by the stated authors, and may not be directly comparable due to differences in calculation

TABLE 2.1.1: EXAMPLES OF REPORTED MODERATION EFFICIENCIES FOR VARIOUS SUBSTANCES.

Author	Moderator	Moderation Efficiency
Khatri *et al.* (1990)	Conical s-Neon	$1.4 (\pm 0.2) \times 10^{-2}$
Mills and Gullikson (1986)	Cylindrical s-Neon	$7.0 (\pm 0.2) \times 10^{-3}$
Merrison *et al.* (1992)	Cup s-Argon (charged)	6×10^{-3}
Khatri *et al.* (1990)	Cylindrical s-Neon	$5.3 (\pm 0.9) \times 10^{-3}$
Greaves and Surko (1996)	s-Neon	5×10^{-3}
Mills and Gullikson (1986)	Flat s-Neon	$3.0 (\pm 0.2) \times 10^{-3}$
Merrison *et al.* (1993)	s-Argon (charged)	2×10^{-3}
Merrison *et al.* (1992)	Flat s-Argon (charged)	2×10^{-3}
Jääskeläinen *et al.* (1997)	s-Krypton	$1.2 (\pm 0.1) \times 10^{-3}$
Weng *et al.* (2002)	Tungsten (111) (annealed)	1.0×10^{-3}
Jääskeläinen *et al.* (1997)	s-Argon	$9.5 (\pm 1.0) \times 10^{-4}$
Merrison *et al.* (1992)	Flat s-Argon (not charged)	7×10^{-4}
Hugenschmidt *et al.* (2002)	Tungsten (100) (annealed)	5×10^{-4}
Weng *et al.* (2002)	N-doped (1.71×10^{18} cm^{-3}) 4H-SiC	1.6×10^{-4}
Weng *et al.* (2002)	N-doped 6H-SiC (1.1×10^{18} cm^{-3}) (annealed)	1.43×10^{-4}
Massoumi *et al.* (1991)	s-Xenon	1.1×10^{-4}
Hugenschmidt *et al.* (2002)	Nickel (polycrystalline)	3.7×10^{-5}
Canter *et al.* (1972)	Smoked MgO	3×10^{-5}
Hugenschmidt *et al.* (2002)	Platinum (polycrystalline)	2.47×10^{-5}
Hugenschmidt *et al.* (2002)	Tantalum (polycrystalline)	5.09×10^{-6}

procedure. For more details, please refer to the relevant paper of interest.

As will be elaborated in section 2.3.1, several compelling observations have been made during the moderation of β^+ particles by thin films of solid neon. The most dramatic of these recorded large fluctuations in slow positron yield, which existed well beyond counting statistics. Following detailed measurements, a link was found between the presence of these fluctuations and the purity of the neon vapour used to form the film, suggesting that the absence of impurities within the crystal lattice was of importance. These transient instabilities in moderation efficiency were not detrimental to final yield however. Indeed, it was seen that an increase in neon purity would result in a larger final slow positron flux, and a more durable moderator over time.

For a general review of positron beams, please refer to Charlton (1998).

2.2 Apparatus

The design of the low energy positron beam at Swansea was based around that successfully used in the ATHENA (AnTiHydrogEN Apparatus) collaboration at CERN, Geneva [Amoretti *et al.* 2004]. A 56 mCi ^{22}Na radioactive source was mounted onto the end of a cold finger, cooled cryogenically using a closed cycle helium refrigerator, on top of which was installed a conical copper extension. At the base of this copper cup, cooled to a temperature of ~ 7 K and biased at + 50 V, a thin titanium window allowed the majority of β^+ particles emitted from the source to propagate into the chamber. To generate the low energy beam required for experimentation, neon vapour was admitted into the conical volume at a rate necessary to maintain a chosen pressure, which was monitored using a cold cathode gauge mounted within the same chamber as the cold finger (see fig. 2.2.1). In early experimentation, the neon gas was fed directly into the chamber from the source canister. However, this method was adapted in later experimentation, as described in section 2.3.1, with the addition of a purification stage, as shown in fig. 2.2.2.

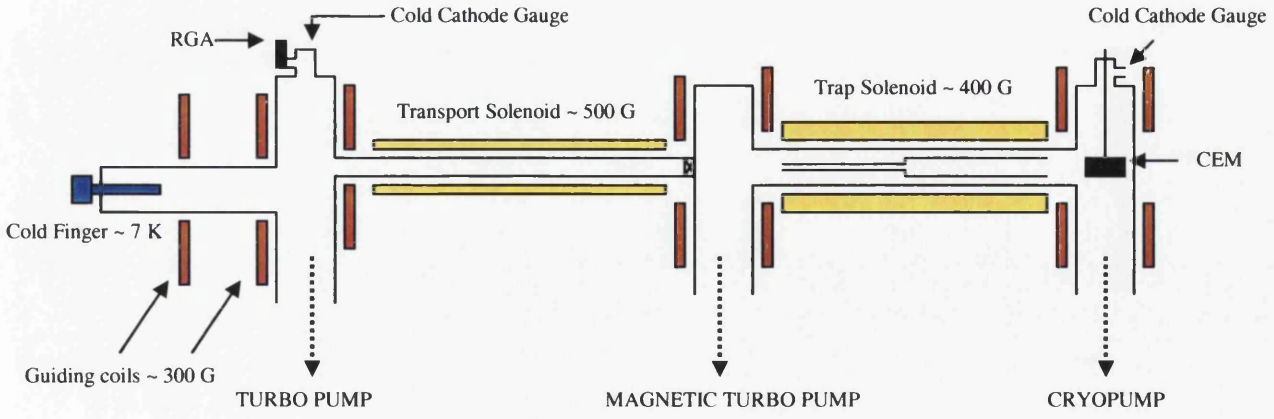

Figure 2.2.1: A schematic diagram of the apparatus used at Swansea to generate a beam of low energy positrons, and to subsequently manipulate the energies of these particles to produce a pulse of ~ 20 ns FWHM resolution. The Residual Gas Analyser (RGA) was used to measure neon purity, while the Channeltron Electron Multiplier (CEM) was used to measure beam intensity.

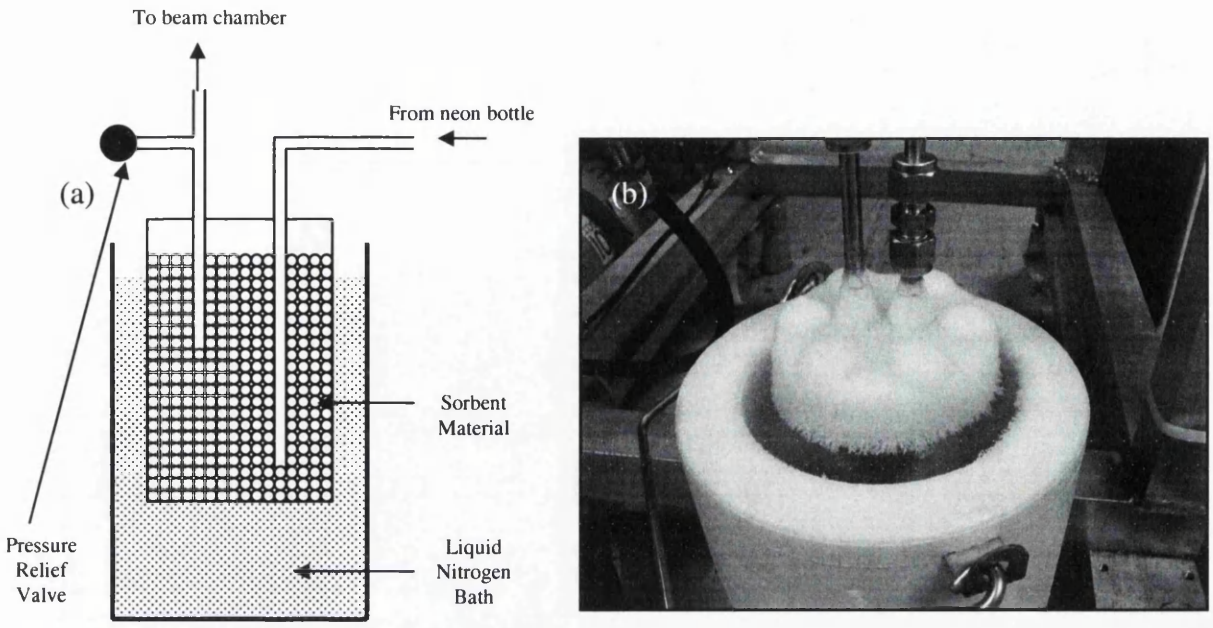

Figure 2.2.2 (a) Schematic diagram of the purifier cross section; and (b) a picture of the actual purifier during use. One may note the formation of ice on the upper surface of the purifier due to its cooling.

The purification device consisted of a standard feedthrough flange bolted onto a tubular insert piece that had been welded shut at the non-flange end. The resulting chamber was filled with zeolite sorbent material, a highly porous silicate with large internal surface area, which, when cooled, removed certain impurities from the neon vapour (as will be shown in fig. 2.3.1.9), as it passed through. A piece of cleaned glass wool was placed into both the gas inlet and outlet tubing, to prevent any dust from the sorbent material from being carried into either the main apparatus chamber, or the neon supply canister. The purifier was then cooled in a bath of liquid nitrogen, to lower the temperature of the chamber such that any impurities within the input vapour which condense at temperatures of ~ 77 K are adsorbed by the sorbent material, and thus prevented from entering the main apparatus. This necessitated the introduction of a pressure relief valve, for prior and during the growth of a moderator, the gas inlet system (including the cooled purifier) was pressurised by the neon vapour to 1 bar. This of course meant that when the moderator growth was

concluded, the gas inlet isolated from the main system, and the purifier allowed to slowly return to room temperature, the pressure within this system would increase. As such, the pressure relief valve was set to vent the system when the pressure reached ~ 1.5 bar.

The rate that the neon was allowed into the chamber was regulated via a computer controlled piezo-electric valve, using the pressure measured by the cold cathode gauge as a feedback input in a PID algorithm (see section 4.2). The neon vapour in the chamber condensed onto the inner surface of the cup, forming a thin film within which incident β^+ particles were slowed via moderation, as described in section 2.1. The low energy positrons ejected from the film were transported using axial magnetic fields generated by a series of guiding coils, which steered the particles around a small kink in the beam-line, which acted as a crude velocity selector by reducing the number of β^+ particles able to traverse through into the main apparatus. It also took the detectors used later in the apparatus out of line of sight of the source, which would otherwise provide a large background signal in all measurements.

During moderator growth, which typically lasted ~ 45 minutes with the neon chamber pressure held at 5×10^{-4} mbar, the positron beam was incident on a gate valve located approximately 1.5 m from the source. The valve was situated immediately after a long drift tube, within which the particles were axially confined by a soleniodal field of ~ 500 Gauss. The resulting annihilation events were monitored throughout the growth cycle using a CsI photo-diode detector, positioned on the outside wall of the apparatus next to the valve. When the number of counts per unit time was seen to reach some maximum intensity, the piezo-electric valve was closed, and the pressure in the chamber quickly fell back to a base level of ~ 5×10^{-10}

mbar. The neon film was annealed to ~ 10 K by switching off the compressor unit in the cryogenic system, and allowing the copper cup to warm to the desired temperature.

When a beam of low energy positrons of the required intensity had been formed, the gate valve was opened, and the particles were able to propagate into the accumulation region. The accumulator device will be described in chapter 4.

2.3 Results

2.3.1 Beam Intensity Anomaly

Throughout early optimisation tests of the moderator growth procedure, before the in-line purification stage was added, an unexpected phenomenon involving apparent moderator efficiency fluctuations occurred. An example of such an anomaly is highlighted in fig. 2.3.1.1, which is a combination of a scanned screen capture of an early count rate measurement, with relevant axes added later. The count rate plot shows an initial constant background count rate, caused by a

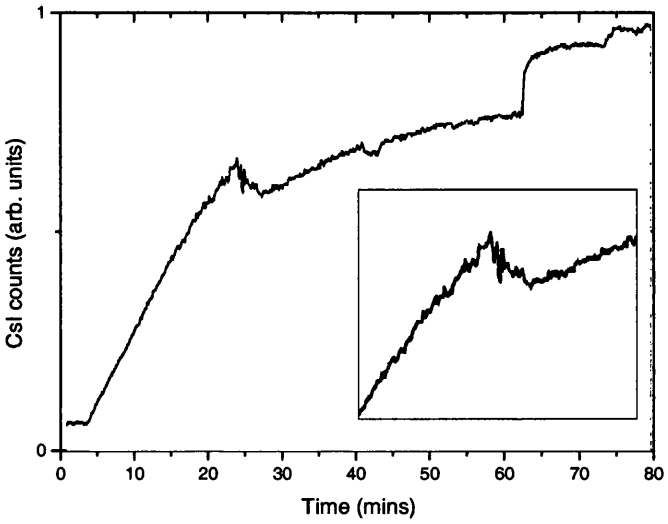

Figure 2.3.1.1: The variation in count rate with time, as measured by a CsI photo-diode detector during moderator growth at 10^{-4} mbar, with the anomalous count rate behaviour expanded within the inset.

combination of external gamma radiation sources, the ^{22}Na source itself, and the effect of mechanical vibrations on the detector. As the neon gas is admitted to the chamber, the count rate is seen to rise as a neon film begins to condense in the cold conical cup, and high energy positrons from the source are moderated. This increase in counts should continue throughout the growth of the moderator, slowing gradually with time, until levelling off at some maxiumum yield. At the point where the film thickness becomes a significant fraction of the β stopping coefficient within the material, a decrease in measured counts would be expected, due to fewer of the particles being able to reach the surface of the film and escape. Therefore, the maxiumum yield at which the count rate levels off at is considered as the optimum film thickness. Thus, the neon input is terminated, resulting in an immediate increase in counts, as the remaining neon in the chamber is pumped out, and attentuation of the low energy positrons leaving the moderator is reduced to zero.

It can be seen however that the slow increase in counts expected during the growth of the moderator is interrupted at ~ 20 minutes, where large fluctuations begin to occur (a factor of five times larger than that expected by counting statistics alone), and the count rate actually begins to fall. This phenomenon lasts for ~ 10 minutes, after which the increase in counts continues, though the rate of this increase seems to be smaller. It is important to note that this phenomenon was seen many times, and at varying input neon pressures.

It is clear that some mechanism is at work to cause these large disturbances in the count rate measured by the detector. To understand the source of this effect, it is first useful to describe the output of the detector, N_{counts}, in an expression that includes all of the factors that have a direct effect upon it,

$$N_{counts} = \varepsilon_s \varepsilon_w \varepsilon_m \varepsilon_t \varepsilon_d N_0 . \qquad (2.3.1.1)$$

Here, ε_s is the efficiency of the source to emit the positrons generated within its bulk (as opposed to self absorption for example), ε_w is the transmission efficiency of the source window, ε_m is the efficiency of the moderator to absorb the incident high energy particles and subsequently emit low energy positrons, ε_t is the efficiency of transporting the low energy particles from the moderation region to the point of annihilation via the guiding magnetic fields, ε_d is the efficiency of the detector to measure all of the annihilation events taking place and N_0 is the activity of the ^{22}Na source. It will be assumed that the attentuation by the neon vapour within the chamber of the low energy beam during transport is contained in the ε_t term. Thus, if some mechanism is occuring which leads to the fluctuations in the measured count rate, then it follows that at least one of the terms described above must be producing this effect.

The position of the detector is unchanged during the moderator growth, and care was taken in subsequent observations not to introduce unnecessary mechanical or electrical noise. Thus, it seems unlikely that a fluctuation in its efficiency that was so reproducible in time was taking place, especially since the variations are larger than that expected by statistics alone.

It seems equally unlikely that the number of positrons entering the moderation region from the source per unit time was fluctuating by such a large degree, in such a predictable fashion, and only during a moderator growth cycle. This eliminates the possibility of the terms ε_s, ε_w, and N_0 being responsible for the anomaly observed.

This leaves only the efficiency of the transportation of the particles from the moderation region, and the efficiency of the moderator itself, as possible sources of the fluctuation seen. During moderator growth cycles, the neon gas pressure was carefully monitored, and no substantial variation was seen as the anomaly was occuring. This raises doubt as to whether a pressure related attentuation mechanism is responsible. The low energy positrons leaving the moderation region are especially sensitive to the strength and direction of the axial magnetic guiding fields, particularly since they have to navigate the bend in the beam-line described in section 2.2. The output of the supplies that powered the coils and solenoid used to produce these fields was carefully monitored, and was shown to vary slightly over time, but these variations were not seen to be coincident with the onset of the count rate phenomenon, seeming instead to be more random. It is thus doubtful that the transport efficiency had variations large enough, and synchronised enough, to produce the phenomena seen.

This leaves only one possible explanation, that of the efficiency of the neon moderator itself. The formation of the neon film to produce the low energy positron beam is a highly dynamic process, and as such it was not possible to investigate fully using the apparatus available. Dedicated studies into the adsorption of neon onto a substrate typically use a less dynamic method to produce the film, where the test region is filled with the gas before the chamber walls are cooled. The neon film is also typically not subject to any form of extreme external stimulus, while in the case described here, it is irradiated with large fluxes of β^+ particles and gamma radiation. As such, characterisation of the phenomenon is unlikely to be achieved within the present apparatus. However, some interesting measurements were made that further

highlighted the possible role of the moderator in the production of the count rate anomaly.

The time for the anomaly to occur after the introduction of the neon to the chamber, t_a, was recorded for a number of moderator growths, at various neon gas pressures, as shown in fig. 2.3.1.2. The trend of $t_a \rightarrow \infty$ as $P \rightarrow 0$ shown would be expected, for the growth rate of the moderator would become infinitely slow. However, the immediate assumption that $t_a \rightarrow 0$ as $P \rightarrow \infty$ is less obvious in the figure, which seems to suggest t_a tending to a non-zero value at the high pressure limit.

To test whether exponential or inversely proportional behaviour were being displayed with respect to pressure, the quantities $\ln(t_a)$ and Pt_a were plotted with varying pressure, from the numbers shown in fig. 2.3.1.2. If the time for the phenomenon to occur was indeed proportional to an exponential term containing the neon gas pressure, then one would expect $\ln(t_a)$ to show linear behaviour with respect to P. This is not seen in the corresponding fig. 2.3.1.3 (top). If t_a was inversely proportional to the neon gas pressure, then one would expect the quantity Pt_a to be a

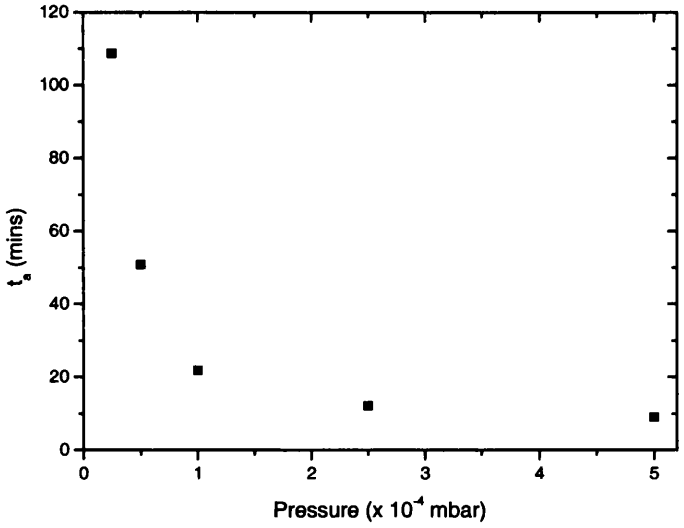

Figure 2.3.1.2: The change in occurrence time t_a of the anomaly with varying moderator growth pressure.

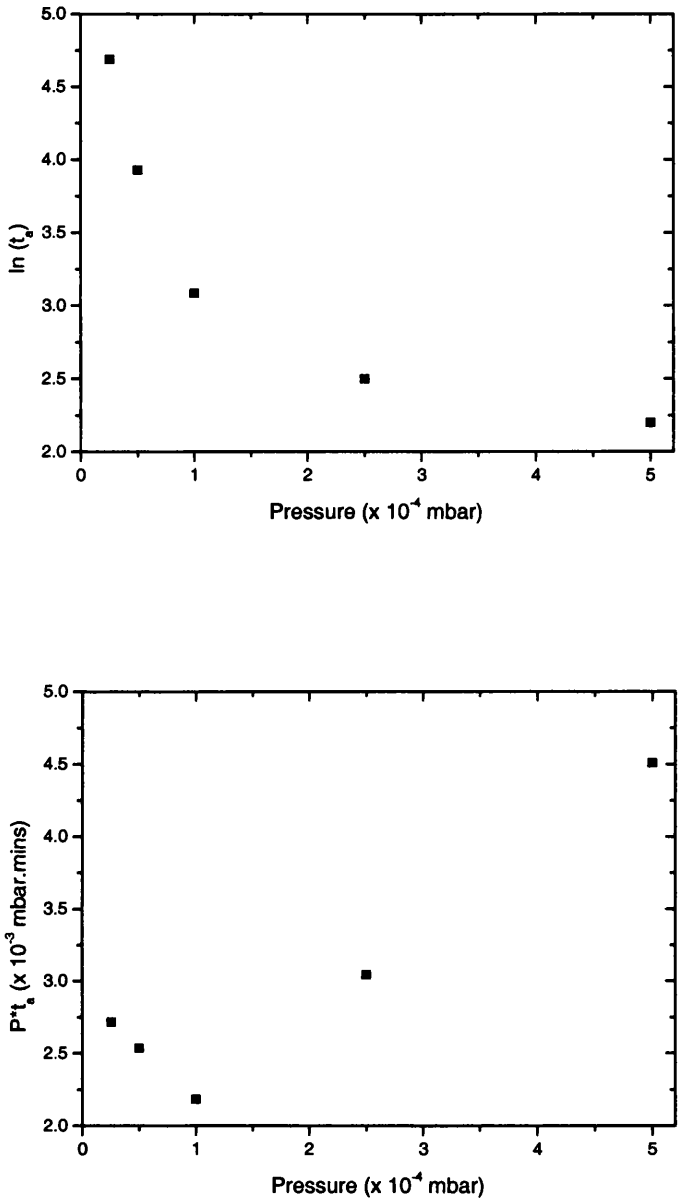

Figure 2.3.1.3: (top) The change in $\ln(t_a)$ with varying moderator growth pressure, which does not show linear behaviour; and (bottom) the change in Pt_a with varying moderator growth pressure, which may imply a constant value at low pressures.

constant value across all pressures. It can be seen from fig. 2.3.1.3 (bottom) that this is not the case either, though a minimum can be seen at small P. To explore this turning point further, the original data shown in fig. 2.3.1.2 was fitted with the general equation

$$t_a = aP^n + t_0, \qquad (2.3.1.2)$$

where a, n and t_0 are fitting constants. The inclusion of the t_0 parameter was made due to empirical observations. The data was successfully fitted when a = 18.04 (± 2.42) minutes.mbar^{-1}, n = -1.26 (± 0.09) and t_0 = 6.05 (± 2.07) minutes. The large error in t_0 may be explained by the lack of measurements made at high pressures, which would have given more information regarding the nature of the high pressure limit of t_a. To test the validity of the fitting constants, the pressure at which the minimum occurs in the Pt_a plot shown in fig. 2.3.1.3 was calculated. This was achieved by modifying equation (2.3.1.2) by multiplying through by P to give

$$Pt_a = aP^{n+1} + t_0 P. \qquad (2.3.1.3)$$

At the turning point, the curve is of zero gradient, and as such

$$\frac{d}{dP}(Pt_a) = (n+1)aP^n + t_0 = 0, \qquad (2.3.1.4)$$

which implies that at the minimum

$$P = \left(\frac{-t_0}{a(n+1)}\right)^{1/n}. \qquad (2.3.1.5)$$

By inserting the fitted values found above, this equation predicts the minimum should occur at ~ 8.2 x 10^{-5} mbar, which is consistent with that shown in fig. 2.3.1.3,

as would be expected.

We now move on to consider the source of the relationship between the time for the anomaly to occur and the moderator growth pressure, as shown in fig. 2.3.1.2, by attempting to characterise the physical processes involved. Let us consider a line of length l drawn between the tip of a cone and a point A on the edge of the cone's base, and a line drawn between the tip and a point B, which is a distance δC away from A on the circumference of the base, as shown in fig. 2.3.1.4. The surface area bounded by the lines OA, OB, and the segment of the circumference AB can be approximated as a triangle, if δC is small. Thus, the whole of the conical surface area may be approximated by iterating around the circumference of the base, and approximating the surface area segments with triangles,

$$\text{Area} = \oint_C \frac{l\delta C}{2} = \int_0^{2\pi} \frac{l\delta C}{2} = \pi r l \,. \qquad (2.3.1.6)$$

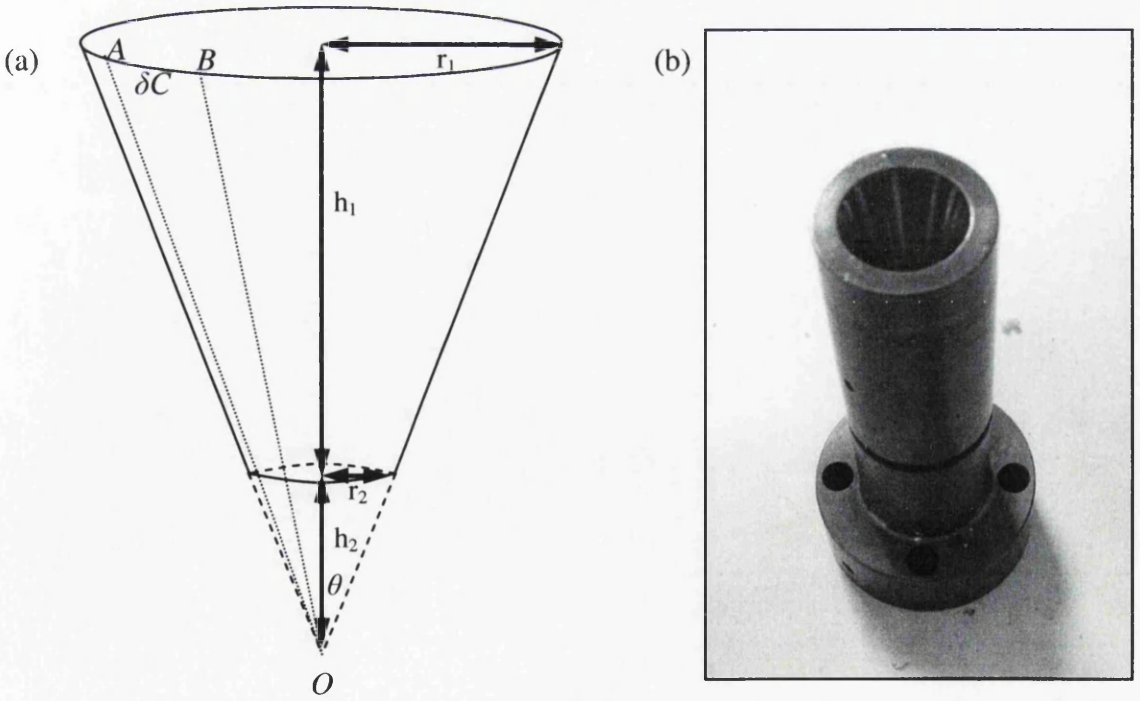

Figure 2.3.1.4: (a) a representation of the moderator growth region, and (b) a photograph of the actual conical cup assembly.

The surface area of the moderator growth region can thus be described by

$$\textit{Moderator Area} = \left(\textit{Area of Large Cone} - \textit{Area of Small Cone}\right) + \textit{Cup Base}$$

$$= \left(\pi r_1 \sqrt{\left(r_1^2 + (h_1 + h_2)^2\right)} - \pi r_2 \sqrt{\left(r_2^2 + h_2^2\right)}\right) + \pi r_2^2, \qquad (2.3.1.7)$$

where the flat bottom of the source/moderator assembly has also been considered as a valid growth region. The h_2 parameter cannot be physically measured, due to the conical shape considered not extending all the way down to its tip, as shown in fig. 2.3.1.4. However, the parameter can be calculated using trigonometric considerations. From the smaller triangle, $\tan\theta = r_2/h_2$, and from the larger triangle, $\tan\theta = r_1/(h_1 + h_2)$, and by combining these two expressions, one finds that

$$h_2 = \frac{r_2 h_1}{(r_1 - r_2)} \quad . \qquad (2.3.1.8)$$

Thus, by applying this to equation (2.3.1.7), we now have

$$\text{Moderator Area} = \left(\pi r_1 \sqrt{\left(r_1^2 + \left(h_1 + \frac{r_2 h_1}{(r_1 - r_2)}\right)^2\right)} - \pi r_2 \sqrt{\left(r_2^2 + \left(\frac{r_2 h_1}{(r_1 - r_2)}\right)^2\right)}\right) + \pi r_2^2 . \qquad (2.3.1.9)$$

The physical dimensions for the actual moderator assembly were measured and found to be r_1 = 7.13 mm, r_2 = 2.88 mm, and h_1 = 19 mm. By inserting these into equation (2.3.1.9), the moderator area is found to be 6.39 x 10^{-4} m^2.

The rate of neon adsorption per unit area on the copper growth surface is governed by the rate of arrival of neon atoms at the surface, and the proportion of these atoms which undergo adsorption,

$$\text{Rate of Adsorption} = R_a = sF\,, \qquad (2.3.1.10)$$

where F is the flux of atoms incident on unit area of the surface, and s is the probability of adsorption of an atom. This probability is strongly dependant on the specific site of incidence on the surface and, as such, is affected by the physical properties of the site. Langmuir (1918) considered that the surface forces acting on the adsorbate are extremely short range, resulting in only atoms incident on the bare surface being able to be adsorbed, with those incident on an atom already adsorbed being elastically reflected back into the gas phase. As such, the adsorption rate per unit surface area [Brunauer *et al.* (1967)] will be

$$R_a = \alpha_0 F(1-\theta), \qquad (2.3.1.11)$$

where θ is the fraction of the surface covered with adsorbed atoms, and α_0 is the ratio of interactions between atom and bare surface that result in adsorption to the total number of interactions. The strike rate can be found using the kinetic energy of gases as

$$F = \frac{P}{\sqrt{2\pi mkT}}\,. \qquad (2.3.1.12)$$

Here P and T are the pressure and temperature of the neon vapour respectively, and m is the mass of a neon atom.

The rate of evaporation of adsorbed atoms from the surface, R_e, is dependent on the binding energy between the surface and the gas atom. If q is the heat absorbed when an atom binds with the surface, then it follows that only an atom that acquires an energy equal to or greater than q may desorb. Thus,

$$R_e = k_0 \exp\left(-\frac{q}{kT}\right), \qquad (2.3.1.13)$$

where k_0, a function of temperature, is dependant on the entropy of adsorption, such that constant R_e implies a constant free energy of adsorption. The rate of desorption per unit surface area is therefore

$$R_d = \theta R_e . \qquad (2.3.1.14)$$

The rate of adsorption and desorption will be equal at equilibrium, such that from equations (2.3.1.11) and (2.3.1.14), it can be said that

$$\alpha_0 F(1-\theta) = \theta R_e . \qquad (2.3.1.15)$$

The solution of equation (2.3.1.15) for θ leads to

$$\theta = \frac{\alpha_0 F}{R_e + \alpha_0 F} = \frac{\alpha_0 P \exp(q/kT)}{\left(k_0\sqrt{2\pi mkT}\right) + \left(\alpha_0 P \exp(q/kT)\right)}, \qquad (2.3.1.16)$$

which can be written in the form of Langmuir's equation

$$\theta = \frac{bP}{1+bP}, \qquad (2.3.1.17)$$

where

$$b = \frac{\alpha_0 \exp(q/kT)}{k_0\sqrt{2\pi mkT}}. \qquad (2.3.1.18)$$

Langmuir's treatment of adsorption only incorporates the formation of an adsorbate monolayer on the surface, as can be seen in equation (2.3.1.11) as $\theta \rightarrow 1$. This assumption is not valid in our case, such that the more detailed theorem of Branauer, Emmett, and Teller (1938) should be applied. The so-called BET theorem extends that of Langmuir by assuming that gas atoms may adsorb on top of atoms already deposited, and each layer of atoms obeys its own Langmuir equation.

Let the surface area covered by 0, 1, 2,..., i,... layers of adsorbed atoms be represented by s_0, s_1, s_2,..., s_i,... [Brunauer *et al.* (1967)]. At equilibrium, the rate of condensation on the bare surface must be equal to the rate of evaporation from the first layer, such that

$$a_1 s_0 P = b_1 s_1 \exp(-E_1/RT), \qquad (2.3.1.19)$$

where a_1 and b_1 are constants, E_1 is the heat of adsorption in the first layer, and R is the universal gas constant, equivalent to $N_A k$, where N_A is the Avogadro constant. At equilibrium, the rate of condensation on s_1 plus the rate of evaporation from s_1 must

be equal to the rate of condensation on s_0 plus the rate of evaporation from s_2, such that

$$a_2 s_1 P + b_1 s_1 \exp(-E_1/RT) = a_1 s_0 P + b_2 s_2 \exp(-E_2/RT). \quad (2.3.1.20)$$

It follows from equation (2.3.1.19) that

$$\begin{aligned} & a_i s_{i-1} P = b_i s_i \exp(-E_i/RT), \\ \Rightarrow\ & s_i = (a_i/b_i) s_{i-1} P \exp(E_i/RT). \end{aligned} \quad (2.3.1.21)$$

The total surface area A of the absorbent is given by $\sum_{i=0}^{i=\infty} s_i$, and the total volume adsorbed V is given by $V_0 \sum_{i=0}^{i=\infty} i s_i$, where V_0 is the volume of gas adsorbed on unit surface area when it is covered by a complete monolayer. It therefore follows that

$$\theta = \frac{V}{AV_0} = \frac{V}{V_m} = \sum_{i=0}^{i=\infty} i s_i \Big/ \sum_{i=0}^{i=\infty} s_i , \quad (2.3.1.22)$$

where V_m is the volume of gas necessary to cover the entire adsorbent surface with one layer of adsorbate.

It is now assumed that $E_2 = E_3 = \ldots = E_i = E_L$, and $b_2/a_2 = b_3/a_3 = \ldots b_i/a_i = g$, where E_L is the heat of liquefaction of the gas, and g is a constant. This assumption dictates that the atoms in the second layer or higher have condensation properties similar to those of the liquid state. The surface elements $s_{1 \to i}$ can now be expressed in terms of s_0

$$s_1 = ys_0; s_2 = xs_1; s_3 = xs_2 = x^2 s_1$$
$$\Rightarrow s_i = xs_{i-1} = x^{i-1}s_1 = yx^{i-1}s_0 = \xi x^i s_0, \qquad (2.3.1.23)$$

where

$$x = (P/g)\exp(E_L/RT)$$
$$y = (a_1/b_1)P\exp(E_1/RT) \qquad (2.3.1.24)$$
$$\xi = y/x = (a_1 g/b_1)\exp((E_1 - E_L)/RT).$$

Using these in equation (2.3.1.22) leads to

$$\frac{V}{V_m} = \frac{\xi s_0 \sum_{i=1}^{i=\infty} ix^i}{s_0\left(1+\xi\sum_{i=1}^{i=\infty} x^i\right)}, \qquad (2.3.1.25)$$

where the summations only have physical applicability when $x < 1$, for V/V_m tends to infinity when $x = 1$ is reached. The summation in the denominator is an infinite geometric progression, such that for $x < 1$, it may be replaced by

$$\sum_{i=0}^{i=\infty} x^i = \frac{x}{1-x}, \qquad (2.3.1.26)$$

while the summation in the numerator can be replaced by

$$\sum_{i=1}^{i=\infty} ix^i = x\frac{d}{dx}\sum_{i=1}^{i=\infty} x^i = \frac{x}{(1-x)^2}. \qquad (2.3.1.27)$$

By combining equations (2.3.1.26) and (2.3.1.27) with (2.3.1.25), one gets

$$\frac{V}{V_m} = \frac{\xi x}{(1-x)(1-x+\xi x)}. \qquad (2.3.1.28)$$

If adsorption takes place on a free surface, then at the saturation gas pressure P_0, an infinite number of layers can be adsorbed onto the surface. This implies that $V \rightarrow \infty$ when $P = P_0$, which from equation (2.3.1.28) subsequently implies that $x = 1$ in this case. Therefore, it follows from equation (2.3.1.24) that

$$\begin{aligned} &(P_0/g)\exp(E_L/RT) = 1 \ ; \\ &\text{and} \quad x = P/P_0 \, . \end{aligned} \qquad (2.3.1.29)$$

It is conventional to convert equation (2.3.1.28) to a linear form, such as

$$\frac{x}{V(1-x)} = \frac{1}{V_m \xi} + \left(\frac{\xi - 1}{V_m \xi}\right) x, \qquad (2.3.1.30)$$

from which important parameters may be quantified by plotting the function of x and V on the left hand side against x, provided ξ is a constant within the range considered. By applying equation (2.3.1.29), equation (2.3.1.30) may be rearranged to give

$$\frac{1}{V} = \left(\frac{1-\xi}{V_m \xi P_0}\right) P + \left(\frac{\xi - 2}{V_m \xi}\right) + \left(\frac{P_0}{V_m \xi}\right) \frac{1}{P}. \qquad (2.3.1.31)$$

This relation must be adapted to take into consideration the time over which the adsorption process is taking place, so that it may be applied to the data shown in fig. 2.3.1.2. This may be achieved by making the assumption that the number of atoms adsorbed during the moderator growth, N_a, may be approximated by

$$N_a \approx R_a t_a A \approx \alpha_a F t_a A = \frac{\alpha_a t_a AP}{\sqrt{2\pi mkT}}, \qquad (2.3.1.32)$$

where α_a represents the mean of all ratios of interaction between neon atom and surface during moderator growth which result in adsorption, and A is the surface area of the moderator growth region. The total volume absorbed is therefore the number of atoms adsorbed multiplied by the volume of each of these atoms, giving

$$V_a = N_a\left(\frac{4\pi r^3}{3}\right) = \frac{\alpha_a t_a AP}{\sqrt{2\pi mkT}}\left(\frac{4\pi r^3}{3}\right). \qquad (2.3.1.33)$$

This approximation can be applied to equation (2.3.1.31) to give

$$\frac{1}{t_a} = \frac{4\pi r^3 \alpha_a A}{3V_m \xi\sqrt{2\pi mk}\sqrt{T}}\left(P_0 + P(\xi - 2) + \frac{P^2(1-\xi)}{P_0}\right). \qquad (2.3.1.34)$$

The packing fraction of neon atoms to form a complete monolayer can be calculated by considering the face-centred arrangement shown in fig. 2.3.1.5. If each monolayer unit cell has a length and breadth of $4r/\sqrt{2}$, and height $2r$, then the unit volume is simply $16r^3$. There is the equivalent of two whole atoms within each of these cells,

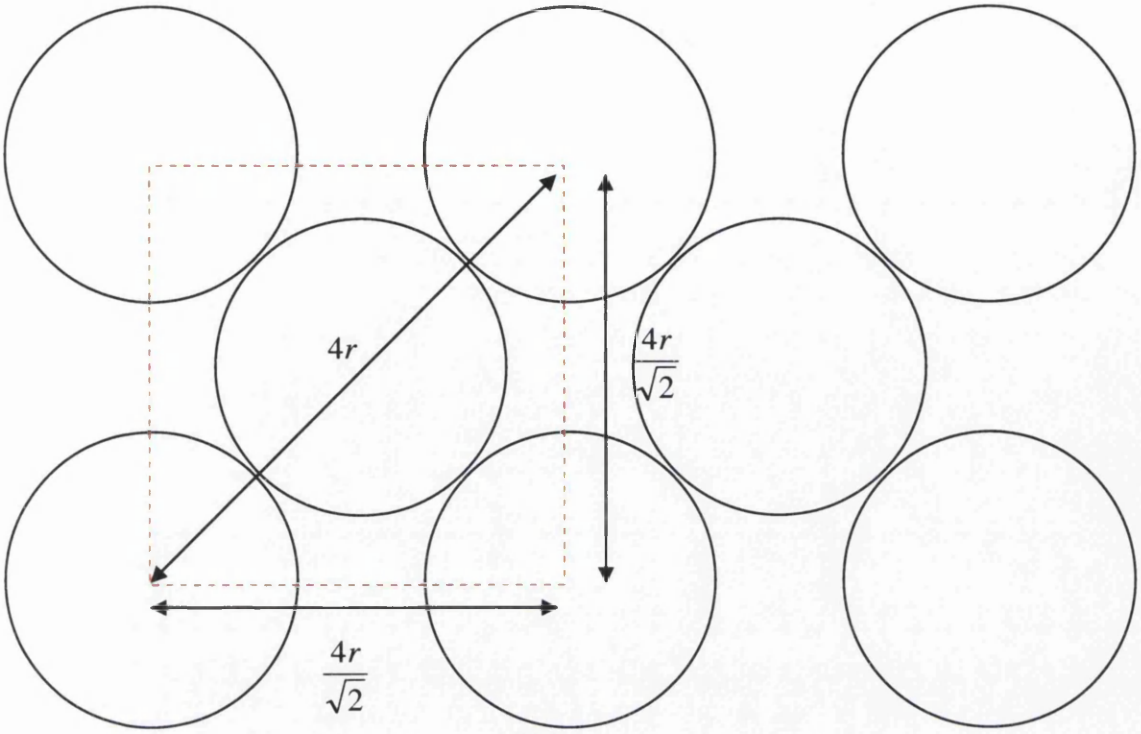

Figure 2.3.1.5: A representation of the first layer to be formed on the adsorbent surface, as viewed from above. The unit cell boundary is shown in red.

which therefore entails a packing fraction of $\pi/6$. This suggests that a full monolayer coverage of the surface made up of these unit cells must have a volume of $A\times 2r\times\pi/6$. This volume is equivalent to V_m, and as such, the quantity A/V_m in equation (2.3.1.34) can be simplified to $3/\pi r$. Therefore, the full expression is modified to

$$\frac{1}{t_a}=\frac{4r^2\alpha_a}{\xi\sqrt{2\pi mk}\sqrt{T}}\left(P_0+P(\xi-2)+\frac{P^2(1-\xi)}{P_0}\right), \qquad (2.3.1.35)$$

within which α_a, ξ, T, and P_0 are all unknown, and r has been left undefined. As shown in fig. 2.3.1.6, it was possible to achieve a loose fit to the anomaly information gained from a number of moderator growth cycles at differing pressures

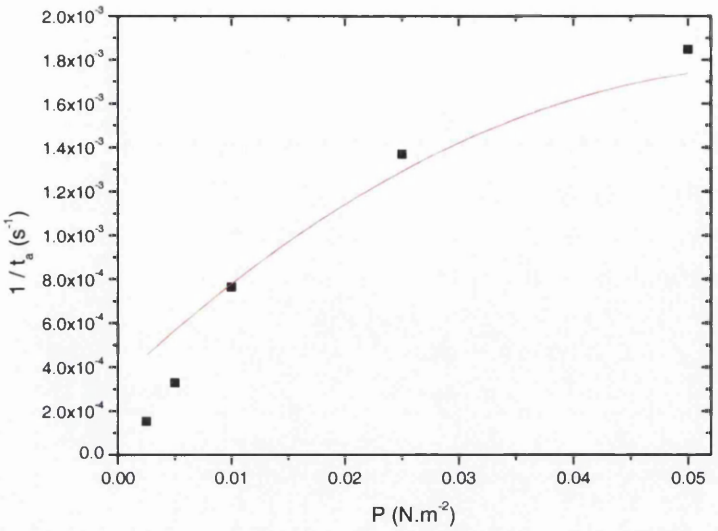

Figure 2.3.1.6: A plot of $1/t_a$ with varying P, fitted by equation (2.3.1.35) with $\alpha_a = 4.63 \times 10^{-7}$, $r = 1.5 \times 10^{-10}$ m, $\xi = 20$, $T = 4.80$ K, and $P_0 = 0.13$ N.m^{-2}.

with equation (2.3.1.35). The large degree of freedom which the number of free parameters introduced is a likely explanation for the difficulty in fitting to the anomaly information more closely. The ξ parameter was constrained to an upper limit of 20 [Brunauer *et al.* (1967)], but closer fits were achieved when the parameter was allowed to increase to non-physical values of more than 10^9. The BET equation is known to fit the majority of experimental vapour adsorption isotherms in the range $0.05 < P/P_0 < 0.35$, where ξ is constant. It is unlikely that this is the case here. A more general approach to quantify some of the physical properties describing the moderator growth will now be considered. It has been shown that the packing fraction of the neon atoms making up the first adsorbed layer on the adsorbent surface is $\pi/6$. Therefore, the number of atoms needed to cover the surface is

$$N_m = \frac{\left(\frac{\pi}{6}\right)2rA}{\frac{4\pi r^3}{3}} = \frac{A}{4r^2}. \qquad (2.3.1.36)$$

The number of atoms adsorbed during the moderator growth, N_a, may be calculated by applying equation (2.3.1.32), and as such, the number of layers formed during the moderator growth, L, may be approximated by dividing N_a by N_m

$$L = \frac{\alpha_a t_a PA}{\sqrt{2\pi mkT}} \times \frac{4r^2}{A} = \frac{4r^2 \alpha_a t_a P}{\sqrt{2\pi mkT}}. \qquad (2.3.1.37)$$

The thickness of an adsorbed film consisting of L layers may be calculated by first considering a monolayer only, and subsequently building more layers at top, as shown in fig. 2.3.1.7. For $L = 1$, the thickness of the film is simply $2r$. In the case of $L = 2$, one must consider a line connecting the centre of a monolayer atom, with the centre of an atom positioned on top of it. By using simple trigonometric considerations, it is easy to show that the vertical distance between these two points is $2r/\sqrt{2}$, and as such, that the full thickness of the two-layer film is then

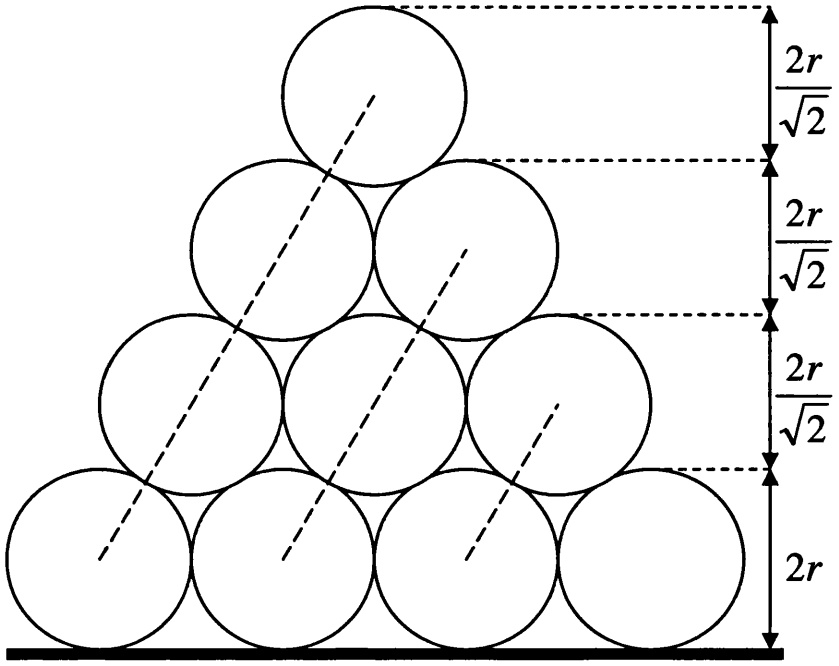

Figure 2.3.1.7: A schematic representation of the thickness of the film as additional atoms are adsorbed on top of the monolayer.

$2r+\left(2r/\sqrt{2}\right)$. By adding more layers, it is clear to see a pattern forming, with $L = 3$ giving a thickness of $2r+\left(4r/\sqrt{2}\right)$, and $L = 4$ giving a thickness of $2r+\left(6r/\sqrt{2}\right)$, leading to the general expression for the thickness d of a film made up of L layers as

$$d = 2r\left(1+\frac{(L-1)}{\sqrt{2}}\right). \qquad (2.3.1.38)$$

For $L >> 1$, equation (2.3.1.38) can be simplified to $2rL/\sqrt{2}$, and combined with equation (2.3.1.37) to give an approximate value for the thickness of film adsorbed during the moderator growth procedure as

$$d_a = \frac{4r^3\alpha_a t_a P}{\sqrt{\pi mkT}} \approx \left(1.2\times10^{-4}\right)\frac{\alpha_a}{\sqrt{T}} \text{ m}, \qquad (2.3.1.39)$$

where r, half the internuclear separation between the atoms, is taken as 156.5 pm [Sutton (1965)], P and t_a are taken from fig. 2.3.1.1 as 10^{-2} N.m^{-2} and 16 minutes respectively, while α_a and T are not precisely known. The thickness of an efficient solid neon moderator is typically of the order of a few positron diffusion lengths within the neon matrix, which fixes d_a at ~ several μm, and subsequently gives an estimate of ~ 10^{-2} K$^{-1/2}$ for $\alpha_a/\sqrt{T}$. This is not consistent with the fit values output in fig. 2.3.1.6, which yield a value of ~ 10^{-7} K$^{-1/2}$, suggesting that no useful physical information may be found from the simplified form of the BET theory in this case, for there is not enough information available from the experiment itself. It should be noted that the interactions between the surface and an incident neon atom are strongly dependent on the adsorbate coverage on the adsorbent. The ratio of

interactions between atom and the surface that result in adsorption to the total number of interactions will therefore gradually decrease as more neon is adsorbed, and as such will depend upon P and time elapsed. Thus, it may be inappropriate to assume that an average value for this parameter, α_a, over the moderator growth time-scale will result in an accurate estimate for the final film thickness. This is also the case for T, where an average value over all temperatures has been implicitly taken. The adsorption of neon from the vapour state to surfaces other than those in the conical cup need not be considered in this case, if it is assumed that the vapour pressure in the cup region is reasonably constant.

The count rate phenomenon shown in fig. 2.3.1.1 was also found to be dependent on the purity of the neon used to produce the moderator. This was discovered when the initial neon supply (99.999% purity at bottle) was drained, and had to be replaced with a source of 98.8% purity within the chamber. The count rate anomaly was not seen in moderator growths using this supply, as shown in fig. 2.3.1.8. The slow steady increase in positron yield here as the neon is administered

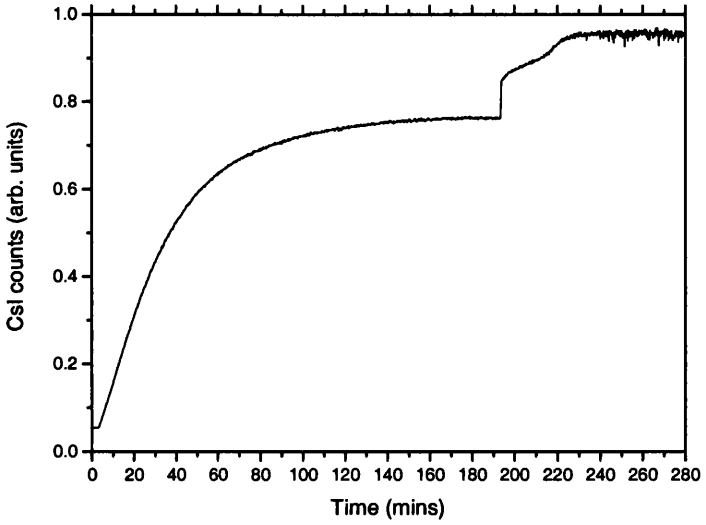

Figure 2.3.1.8: The variation in count rate with time, as measured by a CsI photo-diode detector during moderator growth at 10^{-4} mbar, with a neon supply less pure (98.8%) than that used in the moderator growth shown in fig. 2.3.1.1.

is of the form initially expected from the previous moderator growths within the apparatus. However, a new curious count rate behaviour is seen for this specific neon purity when the gas supply is closed. A fast initial increase in counts is seen as the remaining neon is pumped from the chamber and attentuation effects are eliminated, which is to be expected. However, this is then followed by an added slow increase, which cannot be attributed to the longer time scales required to pump out any impurities left in the chamber from the neon supply. This increase may be due however to a gradual relaxation of the film after the bombardment by the incident neon atoms has ceased, or possible charging behaviour. Within the moderator growth shown in fig. 2.3.1.8, small fluctuations in the count rate formed once this slow increase had ceased. These fluctuations were also seen in other growths using this neon supply when the film was annealed, which persisted long after the film was returned to base temperature. These fluctuations could not be accounted for by counting statistics, and closely resembled those seen in the higher purity moderator growths. This suggests that the mechanism behind the formation of the original anomaly was based on the structural state of the neon film.

To explore this link between neon purity and presence of the count rate phenomenon further, the in-line purification stage described in section 2.2 was added to the apparatus, to ensure that the neon sample entering the chamber was as pure as possible. Before and after the stage was added, a residual gas analyser (RGA) was used to determine the purity of the neon within the moderator growth chamber. It should be noted that these measurements were taken with a fresh supply of neon, rated as 99.999% pure at the bottle. Since the RGA can only operate at relatively low pressures, the neon was vented into the chamber at ~ 1.4×10^{-5} mbar, and not at pressures typically used for moderator growth. The partial pressure measurements for

each constituent of the gas were taken with the conical cup at room temperature, with the purifier not present, as well as present and cooled with liquid nitrogen. The changes in the partial pressures for the main constituents resulting from the introduction of the cooled purifier are shown in fig. 2.3.1.9. The purity of the admitted neon sample with no purification stage in place was found to be ~ 99.47 %, with the addition of the purification raised this to ~ 99.78 %, which was improved further to ~ 99.85 % when the purifier was cooled in a bath of liquid nitrogen. The effect of this added purification stage on the count rate behaviour recorded during moderator growth is shown in fig. 2.3.1.10, where a moderator has been grown with the purifier cooled in liquid nitrogen. It can be seen that ~ 30 minutes into the growth, fluctuations in the count rate begin to form, though they are not of the same general form as those described earlier.

Due to the limitations of the apparatus set-up, this tantalising phenomenon

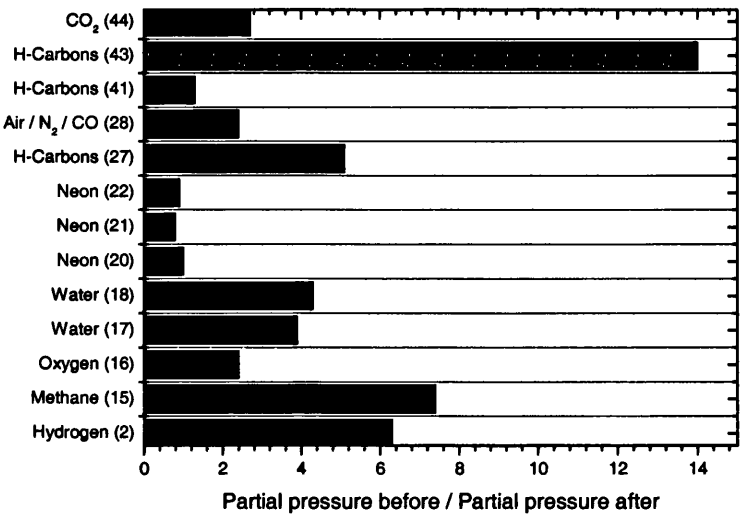

Figure 2.3.1.9: The effect of the addition of the cooled purification stage on the partial pressures of the constituents of the neon gas supply.

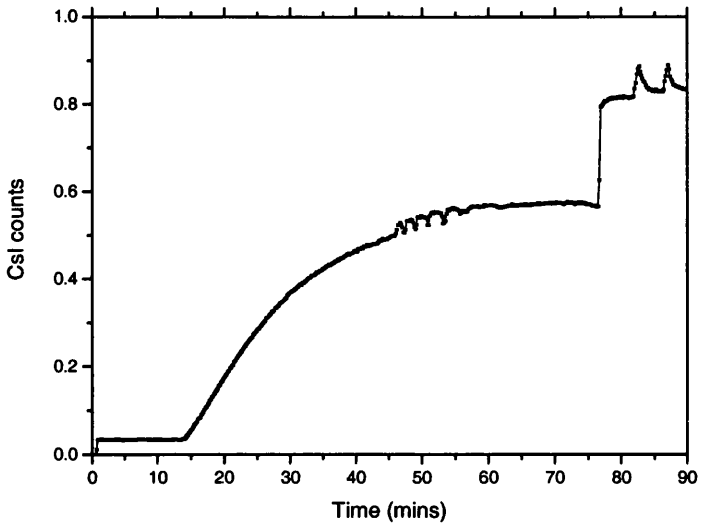

Figure 2.3.1.10: The variation in count rate with time, as measured by a CsI photo-diode detector during moderator growth at 5 x 10^{-4} mbar, with a neon supply purified using the liquid nitrogen cooled assembly. The two peaks occurring after ~ 80 minutes are due to annealing of the moderator.

could not be fully characterised and explained. As the fluctuations were not a permanent feature of the positron flux once the moderator was grown, and no marked reduction in final positron yield was recorded when these fluctuations were present, there was no immediate motivation to study them further. However, one possible explanation of these fluctuations may be tentatively put forward, relating to the long-standing rare gas "crystal structure problem" [Niebel and Venables (1976)]. This problem centres around theoretical calculations on the stability of pure rare gas crystals, which predicted that a hexagonal close-packed (hcp) structure would be energetically favourable over a fcc structure. However, this was not seen experimentally, though the presence of impurities within the lattice was shown to stabilise the hcp structure. With the addition of higher order effects being considered into the theory, the fcc structure was found to be favourable, but with the relative energy difference $(E_{fcc} - E_{hcp})/E_{fcc}$ of only ~ 10^{-4}. This small energy difference raises the possibility of a transition between structural phases occuring during moderator growth, which would likely reduce the mean diffusion length of a positron within the

lattice, and thus cause a decrease in the number able to escape from the film. One can see from fig. 2.3.1.1 that the positron yield is indeed reduced during the time-scale of the anomaly, and that the rate of increase in counts over time directly before and after the anomaly occurs are markedly different. It would thus be extremely interesting to ascertain the structure of the solid neon lattice during the moderator growth, a task that could be fulfiled by careful redesign of current positron beamlines.

If one considers equation (2.3.1.1) once more, it should be noted that the factor governing the flux of low energy positrons in the beam with most scope for improvement is ε_m. As described earlier in the chapter, solid neon films currently stand as the most efficient moderator of high energy positrons, yet their efficiency is still only ~ 10^{-2}. Therefore, any observation which seems to show a dramatic change in the moderation efficiency of a neon film should be of great interest, for it could lend possible insight into new procedures which could further optimise the effectiveness of this technique.

A potential method of studying the moderation process further is to introduce a more manageable technique of growing solid neon films. This could be achieved by adapting the present apparatus by simply installing a gate valve above the turbo pump used to evacuate the moderator growth chamber (see fig. 2.2.1). The new technique of growing a moderator would proceed as follows. First, the chamber would be evacuated to base pressure using the turbo pump, at which stage the gate valve would be closed. The compressor unit of the cryogenically cooled cold finger would be switched off, and the copper cup allowed to warm up. The purified neon vapour would then be allowed slowly into the chamber, to raise the pressure to that desired. This could be achieved by computer control as before, but would require far

more precision, for there is now no pumping speed to combat. Once the desired pressure is reached, the chamber would be isolated from the neon input, and the compressor unit would be switched back on. The pressure in the chamber would then be carefully monitored, as the temperature of the copper cup would drop and adsorption would begin. Unlike the previous method of moderator growth, a direct measurement could be made of the number of atoms leaving the vapour state and being adsorbed onto an adsorbent surface.

It may be assumed that if low enough gas pressures are used, the neon vapour would behave as an ideal gas, and as such, when the chamber is filled to the desired pressure, p_1, the number of atoms within the vapour state before the compressor is switched on, n_1, can be described by

$$n_1 = \frac{p_1 V_c}{kT}, \qquad (2.3.1.40)$$

where V_c is the volume of the chamber. When the compressor unit is switched back on, and neon atoms are adsorbed onto the cold surface, the number of atoms in the gaseous state is reduced, to n_2 say, and so the pressure measured in the chamber decreases, to p_2 say. Thus, at any time during moderator growth, the number of adsorbed atoms may be calculated as

$$N_a = n_1 - n_2 = \frac{V}{kT}(p_1 - p_2), \qquad (2.3.1.41)$$

which raises the possibility of a real-time measurement of the number of atoms adsorbed as the moderator is forming, from which a film thickness may be

calculated, if it can be ascertained what fraction of atoms leaving the vapour state are adsorbed by the moderator growth surface itself. This film thickness information would become invaluable if fluctuations in the measured count rate as reported here were seen.

The main possible source of error using this method would be neon adsorption onto sites which are not irradiated with incident β^+ particles, thus leading to a loss of atoms in the vapour state being falsely attributed to moderator growth. This error would be minimised if the temperature of all parts of the moderator assembly could be measured, to facilitate an estimate of the total effective adsorbent surface area onto which the neon may condense. Information on the variation of temperature within the chamber would also allow added detail in the variation of α across differing adsorption sites within the chamber, which may assist in a more formal analysis of the adsorption mechanisms occurring.

Another source of error using this method would be the increased level of background impurities within the chamber (from sources of outgassing for example), due to the lack of evacuation provided by the turbo pump. This could become problematic with regards to moderator purity if relatively low neon pressures are used. It would also introduce an increase in the measured pressure that was independent of the moderator growth.

The volume of the chamber would also have to be carefully measured, to be sure of accurate calculations of adsorption rates. This could be achieved by filling a chamber of known volume to a desired pressure with a gas, and then carefully venting this chamber into the moderator growth region. The changes in pressure within the two regions could then be used to calculate the volume of the moderator growth chamber, by applying the ideal gas equation.

2.3.2 Beam Diagnostics

Beam Strength

The flux of positrons within the beam was calculated via the application of a coincidence circuit, as shown in fig. 2.3.2.1. When a positron annihilates, there is typically a non-zero probability that a detector used to measure this event will not do so, either due to it not being able to process the input signal (if it is already processing a signal), or if no signal is registered (for example, if none of the annihilation photons are incident upon it). Also, any signals detected by the detector cannot be distinguished absolutely as being due to the positron annihilations of interest, and may be due to any number of background gamma photon sources.

However, if two detectors are used to measure the same event, then a real positron within the apparatus may cause corresponding coincident signals to be measured within each detector. If these signals, spaced from each other by a time *t* say, are applied to a coincidence circuit such as that shown in fig. 2.3.2.1, an output

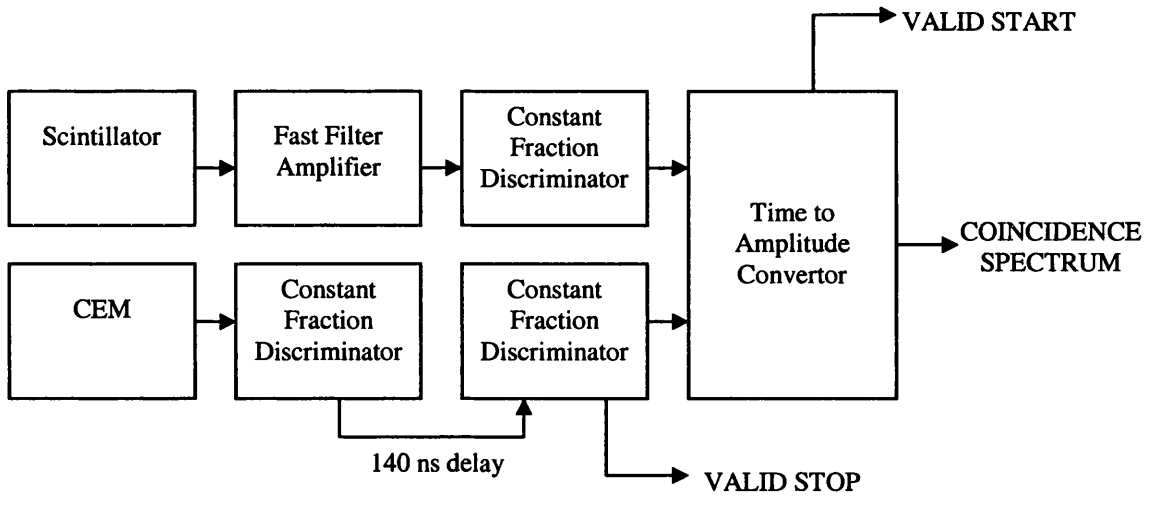

Figure 2.3.2.1: The system of measurement to calculate the positron beam strength using the coincidence technique (see text for details).

signal with amplitude A_t directly proportional to t may be obtained from a time to amplitude converter (TAC) unit. It must be noted that there is a chance of two background counts accidentally being coincident within the time window set for the TAC, and triggering an output pulse from the unit. These so-called accidental counts are considered a background signal from the coincidence circuit, and are factored out by comparing the output to that when the low energy positron beam is not present. The method for removing the positron beam will be explained later.

The resolution of the apparent coincidence of the annihilation signals in time is dependent on the time window set on the TAC device, within which both signals must arrive. A time window of width 1 μs was used in this case. A 140 ns delay was achieved by sending the stop signals through a long length of coaxial cable, which then required an additional constant fraction discriminator unit to be used, to regenerate the signals so that they could trigger the TAC unit.

In the beam measurements, the positrons were detected by a Channeltron Electron Multiplier (CEM) (see fig. 2.2.1) onto which they were incident, and by a scintillation crystal which monitored the resulting annihilation photons. It is clear to see that the detector within the beam-line would be more efficient than the detector on the outside of the apparatus, since the annihilation photons spread out isotropically from the annihilation point. Thus, the scintillator line was used as the start channel for the TAC unit, which would thus have less dead time than if the CEM signal had been used as the start channel.

The beam was generated with the moderator biased at + 50 V, giving a yield composed of moderated, as well as the high energy unmoderated, positrons. The count rate outputs from the valid start and valid stop channels were measured, and a coincidence spectrum taken for 300 seconds. The moderator was then biased at – 50

V, and the procedure repeated. In this second moderator set-up, the moderated positrons would be unable to escape the moderator region, so the beam yield was made up entirely of the higher energy unmoderated positrons, which could thus be factored out of the first measurements. This resulted in the true CEM count rate to be measured as 845,233 s^{-1}, while the true scintillator count rate was measured as 10,467 s^{-1}. The coincidence spectra measured for the two moderator biases are shown in fig. 2.3.2.2. It can be seen that the background counts before and after the coincident peak are of differing numbers. This is due to more start signals being converted by random background triggers in the stop channel to a coincident output in the time before the true stop signals arrive, than after they arrive. Therefore, to get an approximation of the background count to subtract from the coincident peak, an average was taken across the two background levels, in each moderator bias case. In other words, if, for example, the base of the coincident peak was *j* channels wide, then the approximate background to subtract from it would be the average of *j* channels from either side of the peak. Thus, by inspection of the coincidence spectra, it was found that the coincident count rate was 2,565 s^{-1}. If the efficiency of the CEM

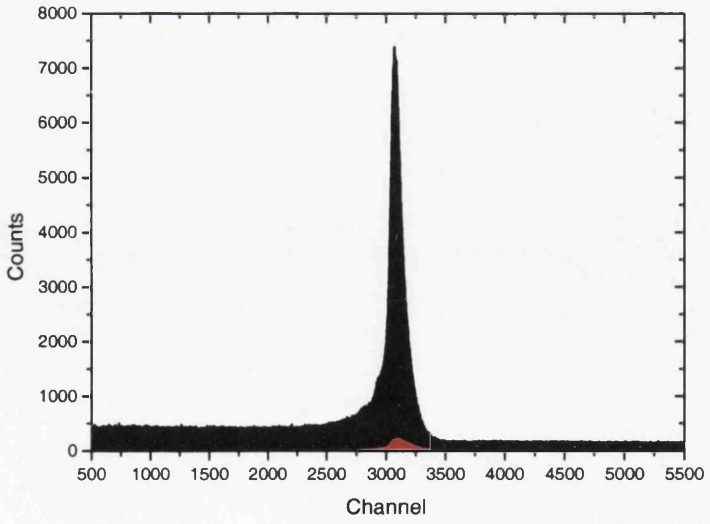

Figure 2.3.2.2: The coincidence spectra measured with moderator biases of + 50 V (shown in black), and – 50 V (shown in red).

detector is denoted by ε_{CEM}, and the efficiency of the scintillation detector by ε_{SCINT}, then the count rate of coincident signals N_C may be described by

$$N_C = \varepsilon_{CEM}\varepsilon_{SCINT}N, \qquad (2.3.2.1)$$

where N is the actual beam count rate which the two detectors are monitoring. Therefore, as the CEM detector efficiency is simply N_{CEM}/N, and the scintillation detector efficiency is N_{SCINT}/N, equation (2.3.2.1) may be rewritten as

$$N = \frac{N_{CEM}N_{SCINT}}{N_C}. \qquad (2.3.2.2)$$

From this expression, the true low energy positron flux was calculated as ~ 3.4 x 10^6 s^{-1}. At the time of measurement, the ^{22}Na source had decayed to an activity of ~ 30.5 mCi. As such, equation (2.3.1.1) may be applied to give an estimate of the typical moderation efficiency ε_m of the solid neon film

$$\varepsilon_m = \frac{3\times10^{-3}}{\varepsilon_s\varepsilon_w\varepsilon_t}. \qquad (2.3.2.3)$$

The transport efficiency, ε_t, may be approximated as unity, the transmission efficiency of the source window, ε_w, may be approximated as ~ 0.9, while the efficiency of the source to emit the positrons generated within its bulk, ε_s, may be approximated as the multiplication of the β branching ratio (~ 0.9) and the total number of these going forward and backscattering (~ 0.75). These approximations

yield an estimate for ε_m of ~ 5 x 10^{-3}, in accord with that reported by other groups using solid neon moderators (see Table 2.1.1), though a factor of 2 smaller than that seen by Khatri *et al.* (1990) who also used a conical geometry. This may be due to an over-estimation of the ε_s term in the approximation above.

Beam Energy

The kinetic energy of the particles parallel to the guiding magnetic fields, $E_{\|}$,

$$E_{\|} = E_T \cos^2 \theta_P, \qquad (2.3.2.4)$$

(with E_T describing the total kinetic energy of the particles, and θ_P being the pitch angle trajectory in the guiding magnetic fields) was measured by placing the CEM detector into the path of the particles, and recording the count rate whilst varying a positive bias placed upon a grid situated in front of the detector. As the retarding bias was increased, only the positrons with enough energy to overcome the repulsion were able to enter the device and be detected. This was steered via LabVIEW control, with manual input taking the form of the range across which to vary the retarding bias, and the time window within which to measure the number of counts for each bias setting. In this case, the retarding bias range was set at 50 to 60 V, with 40 measurements being taken of 1 second each, as shown in fig. 2.3.2.3 (top). This integral spectrum was then differentiated with respect to the varying retarding bias, to produce a beam profile centred at 55.5 eV, of width 2.96 eV (FWHM), as shown in fig. 2.3.2.3 (bottom). This result suggested that the moderated positrons leave the neon film with an average $E_{\|}$ of ~ 5.5 eV, which could be investigated further by repeating the measurement, but now grounding the moderator instead of biasing it at

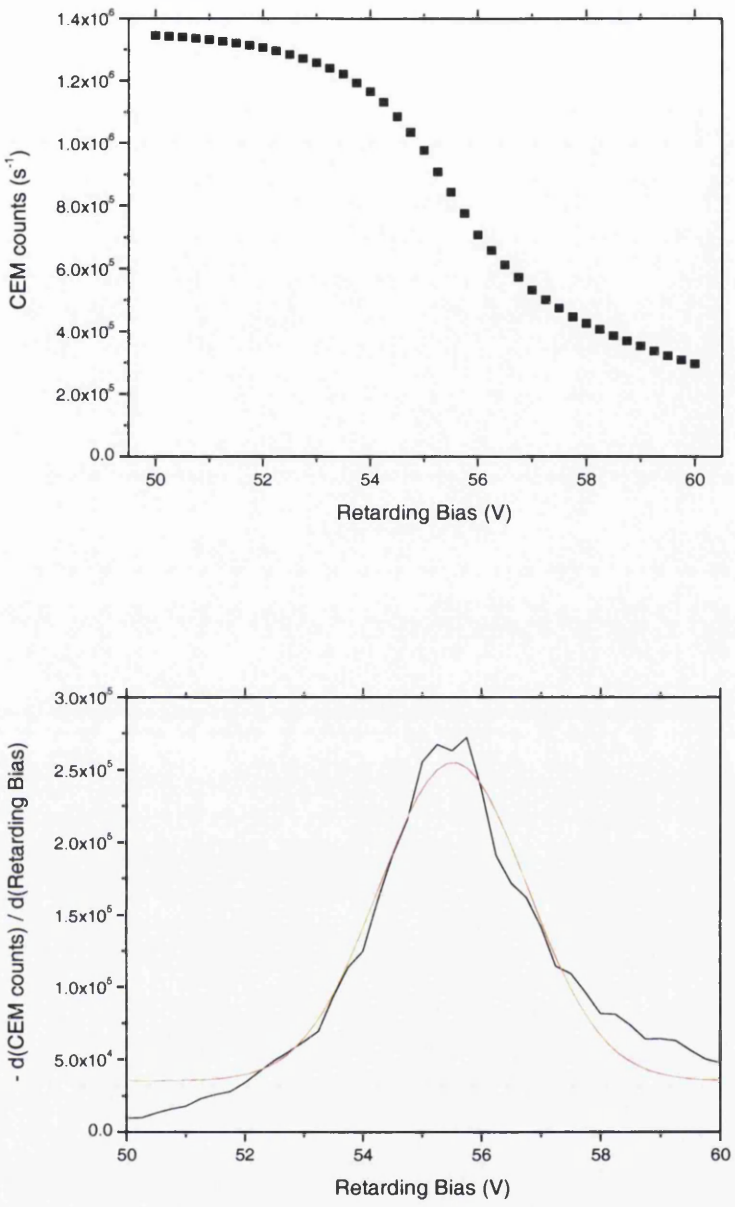

Figure 2.3.2.3: (top) the change in CEM counts with varying retarding bias; (below) the resulting beam energy profile, fitted by a Gaussian function (shown in red) with FWHM = 2.96 (± 0.14) V.

+ 50 V. The resulting beam profile for this case was calculated with 20 measurements of ½ a second each being recorded for retarding biases between 0 and 10 V, as shown in fig. 2.3.2.4. It can be seen that the spectrum is peaked at ~ 6 eV as expected.

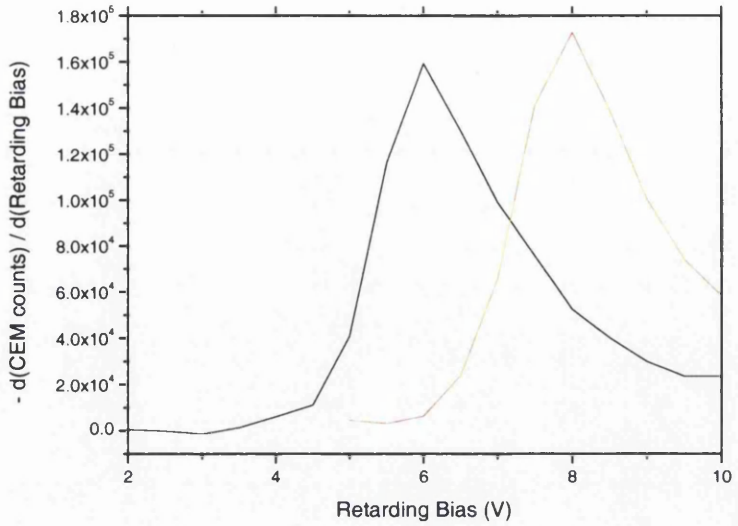

Figure 2.3.2.4: The beam energy profile measured when the neon film moderator is grounded (shown in black), and with the bias cable not connected (shown in red).

The data series for the grounded moderator was only taken over a period of 10 seconds (compared to 40 seconds for the + 50 V case), because the position of the beam energy peak in this case was not constant over time. This was highlighted by removing the cable used to supply the bias to the neon film, so that the moderator was essentially electrically isolated. A beam profile was measured for this scenario, with a retarding bias range of 5 to 15 V, also shown in fig. 2.3.2.4. It can clearly be seen that the beam energy around which the spectrum is centred is increased by ~ 2 eV when the moderator is isolated, which was accompanied by a ~ 9 % increase in measured beam intensity, suggesting some form of charging is occurring within the film. The most likely mechanism causing this effect is the secondary electrons caused by the slowing down of the β^+ particles being able to escape from the film, which cannot be replaced due the electrical isolation of the conical cup. This would produce a global positive charge on the moderator.

Beam Dimension

The physical width of the beam was measured by incrementally lowering a target plate into its path, which was mounted within the final cross-piece of the apparatus (see fig. 5.2.1), and biased at + 60 V. This bias was necessary to distinguish between the particles that missed the target and annihilated on the back wall of the apparatus, and those which would be incident upon the target if they had enough energy to overcome the retarding potential. A CsI photo-diode detector, which was situated on the external wall of cross-piece, was used to monitor the number of annihilation events occurring per unit time. The displacement of the target was controlled using the actuator assembly onto which the target was mounted. The resulting measured annihilation rate at differing target positions was then differentiated in the same fashion to that for the retarding bias measurements, and showed the spatial resolution of the beam to be ~ 4.6 (± 0.1) mm (full width at half maximum), as shown in fig. 2.3.2.5.

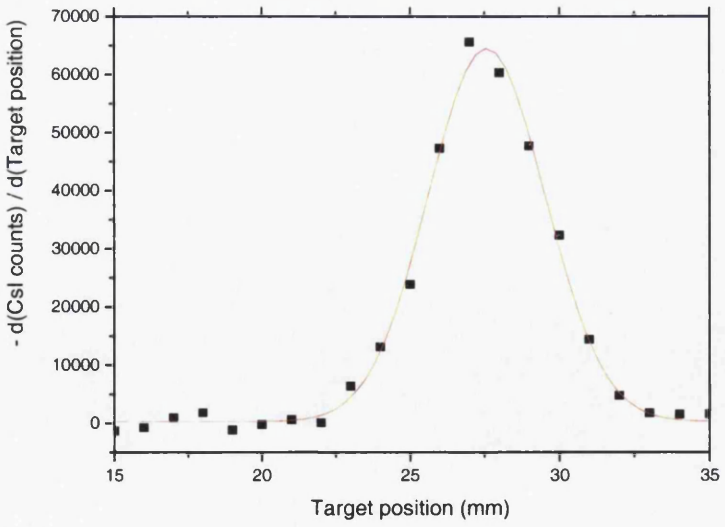

Figure 2.3.2.5: The spatial resolution of the beam (dots) resulting from differentiation of the raw annihilation measurements, fitted by a Gaussian distribution (red line), with full width at half maximum of 4.6 (± 0.1) mm.

3.1 Introduction and Theoretical Considerations

There are many motivations behind the refinement of the time resolution of a distribution of positrons (known as "bunching") generated from a d.c. source, mostly involving experimentation where positrons within an ensemble incident on a sample surface must have the same arrival times, so that the resulting lifetime of the particles within the sample may be ascertained (e.g. Triftshäuser *et al.* (1997)). In the case of a pulsed source (e.g. a target irradiated by pulsed relativistic electrons leading to pair producton), which produces bursts of positrons, it can be used to further minimise the pulse width (e.g. Stoeffl *et al.* (1999)).

There are two methods with which one may bunch a positron beam [Mills (1980)]: by using a time-varying, or a spatially-varying, potential. Each produces the required bunching effect by accelerating a string of positrons in such a way that particles at the tail end of the distribution are given enhanced acceleration in relation to those at the head of the distribution. This leads to a compression of the distribution as it travels down a beam-line, such that at some point a minimum time resolution is reached.

The spatially-varying potential is chosen to be harmonic along the axis of the region within which the bunching will occur, such that the force applied to the particles by the bunching field is linearly dependant on their position relative to the potential minimum. This method of bunching was successfully used at the positron facility of the University of Aarhus, Denmark, with a number of simulations of this device being presented later in this chapter. As such, this bunching technique will be

further elucidated. The following analysis is similar to that of Mills (1980) and Hulett *et al.* (1991), and produces equivalent results.

A positron, of mass m with unit charge e, within an electric field of strength E, will be subject to an acceleration as described by Newton's second law of eE/m. By using the one dimensional analogue of $\underline{E} = -\nabla V$, this acceleration may be rewritten as

$$\frac{d^2x}{dt^2} = -\frac{e}{m}\frac{dV}{dx}, \qquad (3.1.1)$$

where the potential difference dV exists across the distance dx. A buncher based on the spatially-varying potential method may have an electric field that originates from a harmonic potential difference bounded by $V\ (x = 0) = 0$, and $V(x = -\ l) = V_b$, as shown in fig. 3.1.1. As such, the potential at any point between these boundaries may be described by

$$V(x) = V_b\left(\frac{x}{l}\right)^2, \qquad (3.1.2)$$

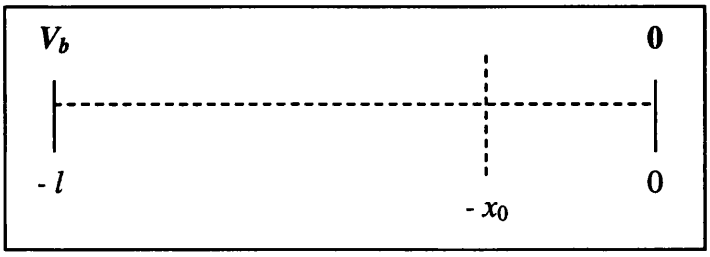

Figure 3.1.1: A schematic diagram to illustrate the boundary cases within a spatially-varying potential bunching device.

which therefore leads to

$$\frac{dV}{dx} = \frac{2xV_b}{l^2}, \qquad (3.1.3)$$

which when combined with equation (3.1.1) gives

$$\frac{d^2x}{dt^2} = -\frac{2xeV_b}{ml^2} = -\omega^2 x, \qquad (3.1.4)$$

where ω is the angular frequency of the harmonic motion. A solution to equation (3.1.4) may take the general form

$$x = A\sin(\omega t) + B\cos(\omega t), \qquad (3.1.5)$$

which therefore gives

$$\frac{dx}{dt} = A\omega\cos(\omega t) - B\omega\sin(\omega t). \qquad (3.1.6)$$

At time $t = 0$, equation (3.1.5) reduces to simply B, which must correspond with the initial position of the particle, - x_0 say. Equation (3.1.6) reduces to $A\omega$ at $t = 0$ however, which must correspond with the initial velocity of the particle along the axis, v_0 say. Thus, a general solution for equation (3.1.4) is

$$x = \frac{v_0}{\omega}\sin(\omega t) - x_0\cos(\omega t). \qquad (3.1.7)$$

The time taken, t_f, for a particle to reach the focus point $x = 0$ can now be found via rearrangement of equation (3.1.7), to give

$$t_f = \frac{1}{\omega}\tan^{-1}\left(\frac{x_0\omega}{v_0}\right). \qquad (3.1.8)$$

The initial velocity of the particle may be found by considering the initial kinetic energy of the particle V_e, such that

$$v_0 = \sqrt{\frac{2eV_e}{m}}. \qquad (3.1.9)$$

Therefore, by combining equations (3.1.4), (3.1.8) and (3.1.9), a general expression for the time of flight for a particle from its initial position in the region considered to the focussing point may be found to be

$$t_f = \frac{1}{\omega}\tan^{-1}\left(\frac{x_0}{l}\sqrt{\frac{V_b}{V_e}}\right). \qquad (3.1.10)$$

If one considers the case of a particle starting initially at rest, then by inspection of equation (3.1.10), one can see that the resulting time of flight is described by

$$t_f(V_e = 0) \rightarrow \frac{\pi}{2\omega} = \frac{\pi d}{2}\sqrt{\left(\frac{m}{2eV_b}\right)}, \qquad (3.1.11)$$

which is a constant. This implies that theoretically the output timing spectrum should be of zero width when all particles within the device are at rest when the bunching field acts upon them.

3.2 Apparatus

The positron bunching apparatus developed at the University of Aarhus [Merrison *et al.* (2003)] consisted of an array of 47 cylindrical electrodes, of length 20 mm, and internal diameter 50 mm. The electrodes were separated using 1 mm ceramic spacers, which also electrically isolated them from each other. The whole array was mounted on three ceramic rods, and installed within a cylindrical vacuum tube, which was integrated into the beam-line system. Each electrode was wired individually using copper wire, all of which were kept to approximately the same minimum length.

The biases for these electrodes were to follow the desired parabolic behaviour, to induce a time bunching effect on the particles within. The electric potentials of the first 33 electrodes were generated via a pulsed input bias being divided as appropriate as it propagated down a series capacitor chain, with the remaining electrodes being dc biased and wired using a resistor chain. The use of a capacitance chain over the more conventional resistance chain was devised to reduce the propagation time of the pulsed bias down the chain, and to allow operation at higher frequencies. The calculation of the appropriate external capacitances to be

placed between each of the electrodes electrically required careful measurement of the intrinsic capacitance between each electrode pair, and the capacitance of each electrode to ground. These exhaustive measurements allowed any variation in the positions of the electrodes with respect to each other, and the grounded vacuum tube within which they were mounted, to be taken into account. The final two components in the capacitor chain of n elements are represented in fig. 3.2.1, where V_n represents the necessary bias to be placed on the nth electrode, C_n represents the effective capacitance between the nth and (n - 1)th electrodes, and C_n^g represents the measured capacitance to ground of the nth electrode.

The absolute value of the charge q on either plate of a capacitor of capacitance C, at a potential difference V, may be expressed as

$$q = CV\,. \qquad (3.2.1)$$

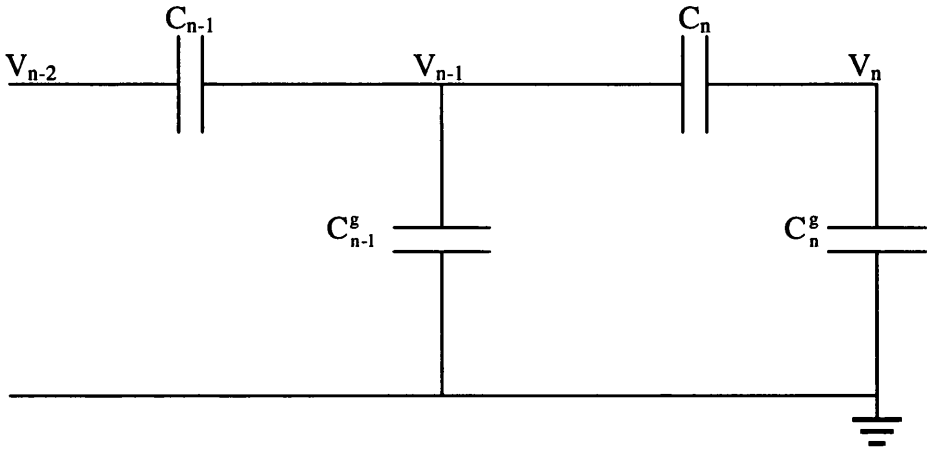

Figure 3.2.1: A schematic representation of the final two components in the capacitance chain.

If we consider the junction coinciding with the (n - 1)th electrode in fig. 3.2.1, then the charge entering this junction must be equal to that leaving the junction. Therefore, it follows that

$$C_{n-1}(V_{n-2}-V_{n-1})=C_n(V_{n-1}-V_n)+C^g_{n-1}V_{n-1},$$
$$\Rightarrow C_{n-1}=\frac{C_n(V_{n-1}-V_n)+C^g_{n-1}V_{n-1}}{(V_{n-2}-V_{n-1})}. \qquad (3.2.2)$$

The capacitance C_n may also be calculated, by applying equation (3.2.1) to the junction corresponding to the nth electrode in fig. 3.2.1

$$C_n(V_{n-1}-V_n)=C^g_nV_n,$$
$$\Rightarrow C_n=\frac{C^g_nV_n}{(V_{n-1}-V_n)}. \qquad (3.2.3)$$

A computer program was used to apply these equations to calculate the required capacitances C_n to generate the parabolic distribution of biases down the electrode chain, and also to calculate the biases expected to be measured at each electrode using a probe of known input capacitance. The deviation of the measured bias from the ideal bias necessary for the parabolic distribution was found to be less than 1 % at each electrode, which was acceptable for the experiments planned.

The length of the capacitance chain was measured as 2.21 m, which fixed a lower limit on the propagation time of the bias pulse down this chain at ~ 7.37 ns, using the speed of light in vacuum. When a test bias of 300 V was pulsed down the chain, it was found to take 10 ns to propagate from the first electrode in the array to the 33rd. The rise times for these electrodes were found to vary linearly along the

array, with the first electrode taking ~ 30 ns to reach its maximum bias, and the 33rd taking ~ 10ns. This implied that the total activation time for the bunching field was ~ 30 ns, with electrode 33 being to first to reach its maximum bias, 20 ns after the initial bias was pulsed into the capacitance chain.

The positron beam used to load the bunching device was generated using a solid argon film to moderate the β^+ spectrum output from a 1.5 GBq ^{22}Na radioactive source. The beam, of energy centred at approximately 5 eV with a similar energy spread, was allowed to enter the buncher volume when the capacitance chain was inactive, and travel towards the end electrodes which were dc biased. The field generated by these electrodes acted as a retarding potential, and repelled the particles back towards the entrance of the buncher. At the moment of initialisation of the bunching field, any of these positrons travelling towards the entrance or exit of the device would be subsequently harnessed, and as such, the effective active length of the device was ~ 1.4 m, twice that of the capacitively coupled section. The particles which were ejected from the device were detected by a ceratron electron multiplier detector.

A voltage of 1 kV applied to the capacitance chain resulted in a bunched positron burst from the device of 1.2 ns (FWHM), or 2.0 ns (10% - 90% width). This temporal width was an unexpected result, for it does not agree with the resolution expected by theory, as described by equation (3.1.11). This expression was solved for the two extreme points of the pulsed buncher region, namely $x_0 / l = 0.3$ and 1, to give $t_f(0.3) \sim 71.5$ ns, and $t_f(1) \sim 80.1$ ns. This expected full width of ~ 8.6 ns was not seen, indicating that a hitherto unconsidered effect was at work within the device.

The source of this extra mechanism was found by considering the effect of the propagation of the pulse bias down the capacitance chain. The theoretical model

of the bunching device, described in the previous section, considered the bunching field to be present within the device volume with no delay after activation. However, in reality, the initial pulse bias has to travel down the capacitance chain, and activate each of the first 33 electrodes independently, resulting in particles located near the entrance of the device at the moment of activation being acted upon before those nearer the exit of the device. This would result in a simple shift in the times of flight for the particles, as those nearer the exit of the device have an added time after activation of the buncher before they actually experience the bunching field. There is no added time for those particles at $x_0 / l = 1$, for this is where the capacitance chain is activated. From this point on however, there is an added time, which would increase up to the full 10 ns for those particles at $x_0 / l = 0.3$, which is where the capacitance chain ends. If we assume that the activation times of the first 33 electrodes varies linearly, then a modified version of equation (3.1.10) gives

$$t_f = \frac{1}{\omega}\tan^{-1}\left(\frac{x_0}{L}\sqrt{\frac{V_b}{V_e}}\right)+\left(14.3\times10^{-9}\times\left(1-\frac{x_0}{l}\right)\right), \qquad (3.2.4)$$

which now gives $t_f(0.3) \sim 81.5$ ns, while $t_f(1) \sim 80.1$ ns. The effect of the pulsed bias propagation delay can be more clearly seen in fig. 3.2.2, which shows equations (3.1.11) and (3.2.4) solved for a number of different points within the device. This predicts positron arrival times at the potential minimum of full width resolution ~ 3.5 ns, in better agreement with the measured result.

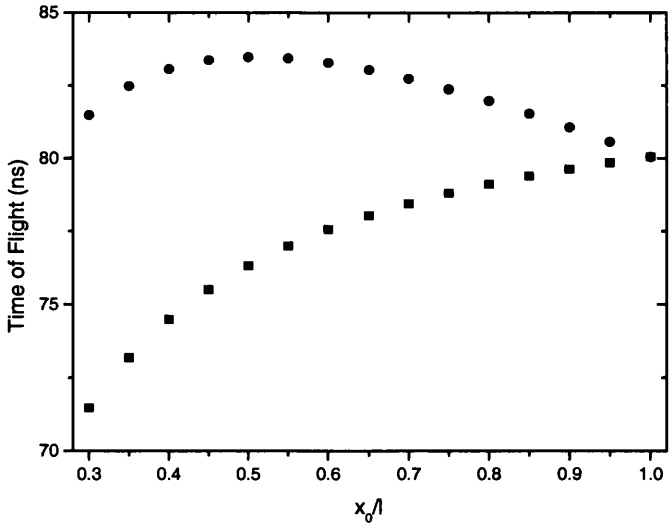

Figure 3.2.2: The expected times of flight for 5 eV positrons ejected from a 1 kV bunching field, from various starting positions, as dictated by conventional theory (shown as squares), and considering bias pulse propagation delay (shown as circles).

3.3 The Simulation Procedure

The SIMION v7.0 ion optics simulation package [Dahl 2000] allowed detailed investigation to be made into the processes taking place during the bunching of positrons within the Aarhus apparatus. SIMION is a simulation program that models ion optics problems with two-dimension symmetrical and/or three-dimension asymmetrical electrostatic and/or magnetic potential arrays, with a workbench volume of up to 8 km^3. The package makes use of potential arrays that define the potentials and geometry of electrodes and magnetic poles. The potentials of points outside electrodes and poles are determined by solving the Laplace equation by finite difference methods, labelled as 'refining' the array within the package. These refined arrays can then be projected into a workbench volume, within which ions can be flown, their trajectories subject to the fields of the potential array. A potential array within the package may define electrostatic or magnetic fields, but not both. In the

case of a simulation necessitating both electric and magnetic fields, these must be superimposed in the workbench volume using separate potential arrays. More precise details on the functioning of the SIMION software package can be found in the operation manual.

The Aarhus electrode pieces were modelled by creating a geometry file, which was used to define the apparatus in two dimensions (x,y). This was then processed by the SIMION package, which applied cylindrical geometry to produce the three dimensional space shown in fig. 3.3.1, which was saved as a potential array. The geometry file was also used to define the first 33 electrodes as being adjustable during ion simulations, which allowed the bias pulse propagation delay, and the rise time of each of these electrodes, to be modelled. The remaining electrodes were

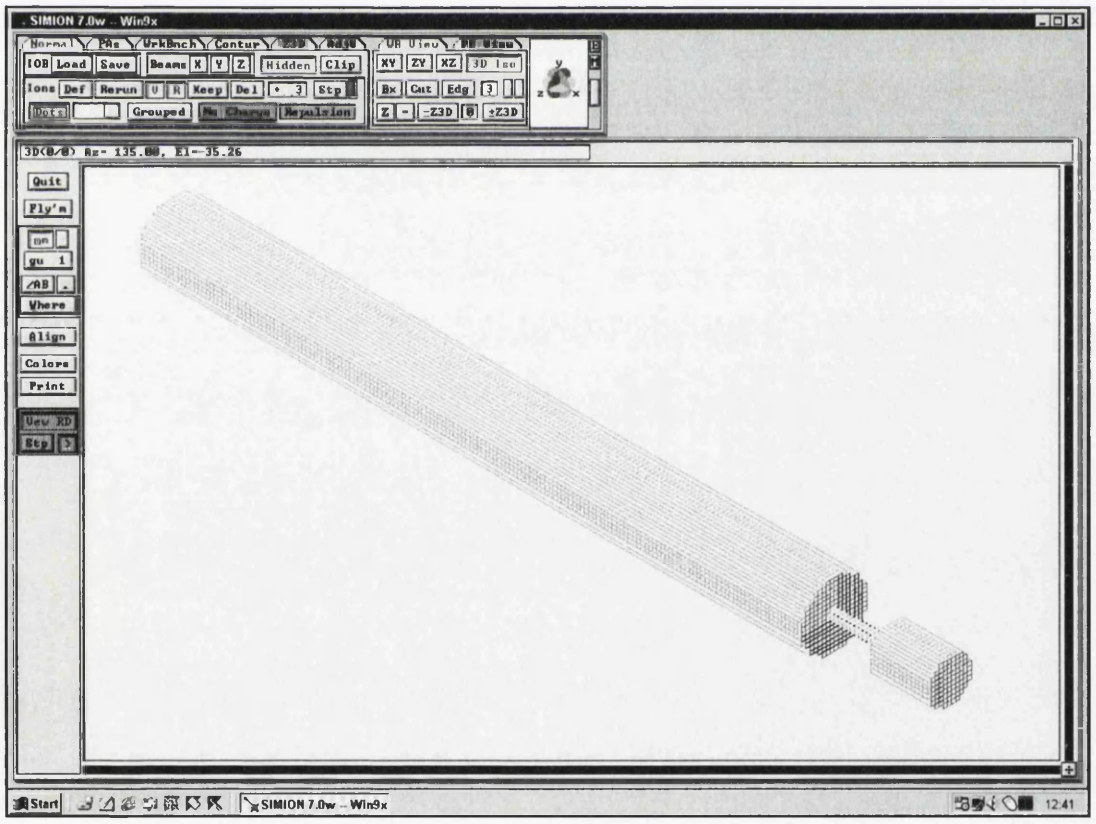

Figure 3.3.1: A screen capture showing the SIMION v7.0 ion optics simulation package running within the Microsoft Windows environment. A three dimensional isometric rendering of the external surface of the simulated bunching device is displayed. The second chamber seen in the bottom right of the figure is an additional acceleration stage fitted to the physical apparatus, which was not considered within the simulations.

defined as static, meaning that the bias upon them throughout the simulations would be constant.

Once the potential array had been refined, simulations could be conducted. The SIMION package itself allowed for simple controls over the simulation process, such as the mass, charge, and number of the particles to be simulated, and their starting positions etc. For more complex control over the simulated particles and electrodes however, a program file had to be written, which SIMION would access before each simulation run. This allowed several physical processes such as pulse propagation delay, electrode rise time, randomised starting energies, randomised drift time, and non-harmonic potentials to be simulated. For further details on the program files, please refer to the Appendices. The parameters required for output to a data file were either specified within the relevant control window within the software package, or were output via the user program file. These data were then processed by the most suitable software package for the specific case, for example Mathematica v4.2, Origin v7.0, or Microsoft Excel 2002.

3.4 Results

3.4.1 The effect of discrete electrodes

The theoretical description of the expected time of flight of a positron within the apparatus assumes a uniform bunching field, which varies quadratically with axial position. However, this uniformity is difficult to produce in reality, and it should be expected that there will be imperfections in the bunching field generated within the apparatus, due to the discrete nature of the electrodes used. The effect of these imperfections on the resulting performance of the apparatus to produce

focussed pulses of positrons can be clearly seen in fig. 3.4.1.1, in which an idealised case has been considered, where there is no delay for the bias pulse to travel down the capacitance chain, and the electrodes initialise to their chosen bias immediately. The particles were started at rest on the central axis, and bunched from the apparatus using a 1 kV potential difference. The time of flight for a particle was measured from the moment of initialisation of the bunching field, to the moment it reached the potential minimum, which coincided with the central point of the last electrode in the array. The expectation for this idealised case is that all positrons would take the same amount of time to reach the potential minimum of this bunching field. Thus, it would be naively assumed that the resulting variation in times of flight for particles starting from differing positions would be zero, as each would have taken the same amount of time to reach the potential minimum. It can be seen however in fig. 3.4.1.1 that this is not the case, and that highly ordered oscillations about a slowly increasing time of flight are present. By inspection of the number of these oscillations and their positions, it was found that they coincided with the 1 mm gaps present between the

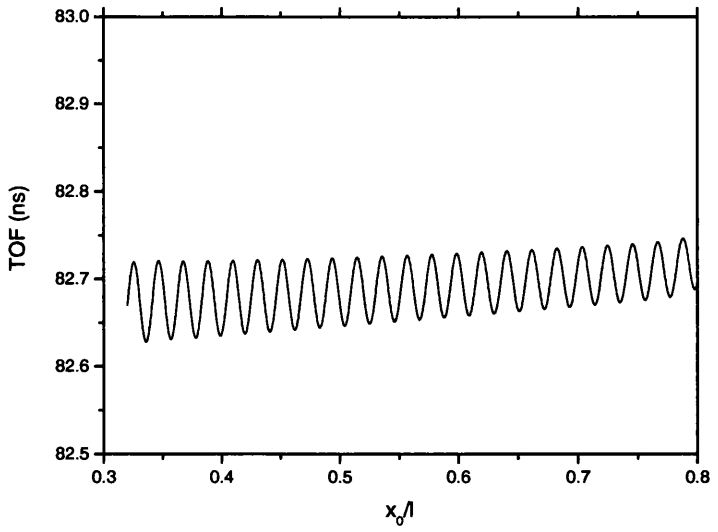

Figure 3.4.1.1: The times of flight for particles, initially situated at rest at various distances x_0 along the central axis of the apparatus, of length l, to reach the minimum of the 1 kV bunching potential difference. The bias pulse propagation delay, and the rise times of the electrodes were not considered.

electrodes. This should be expected of course, for the field is altered in these gap regions due to leakage out to the grounded vacuum tube. This has the effect of slightly lowering the effective potential on axis in these regions, when compared to an ideal case. Thus, particles which start in the vicinity of one of these gaps are delayed, for they first have to navigate over the small potential step present. As these particles then travel towards the buncher exit, they have to pass through more of these imperfections, which now however cause less of a delay, for the particles have acquired greater kinetic energy. These slight delays though will add up as the particle moves towards the potential minimum, which may be an explanation for the positrons starting at high x_0/l positions having slightly greater times of flight than those initialised at smaller x_0/l.

A map of the distribution of potentials, and resulting electric field magnitude, within the apparatus was output to confirm this hypothesis, by placing test charges at equidistant positions on the x,y plane within the simulated device (where the z axis is that of the apparatus), and recording the potential and field experienced. An array of potentials and field magnitudes were recorded in each case, which could then be plotted within the Mathematica software package, to produce a three dimensional contour plot of the distributions within the buncher, as shown in fig. 3.4.1.2.

The distributions resulting from these simulations reveal a great deal of information about the field variations within the device. It can be clearly seen in the potential distribution that there are slight variations present on the outer edges of the region considered, which produce large variations in the field magnitude distribution. These variations coincide with the spacing between neighbouring electrodes, as expected, and extend inwards towards the central axis, explaining the time of flight behaviour seen in fig. 3.4.1.1. The large increase in field magnitude seen at low x

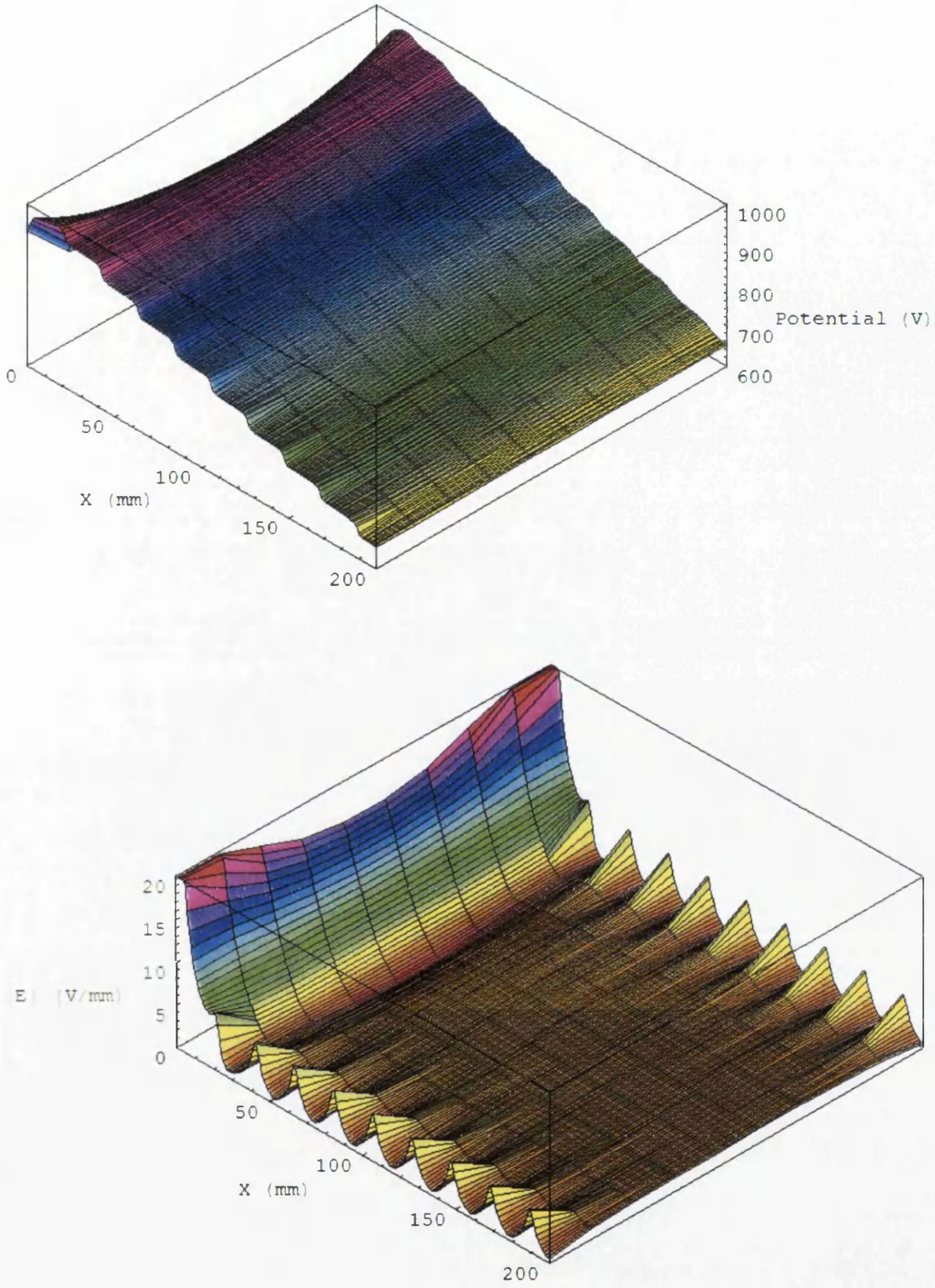

Figure 3.4.1.2: A three dimensional plot of: (top) the variation of potential on the x,y plane generated by the electrode array; and (bottom) the variation in the magnitude of the electric field generated by the electrode array on the x,y plane. The x axis represents the distance along the cylindrical axis, the origin of which coincides with the start of the electrode array. The y axis represents the physical internal diameter of the device. Note that the x and y axes have been plotted out of proportion with one another to aid the eye.

values can be understood by remembering that the first electrode in the chain is biased at 1 kV, with the chamber walls outside the bunching device being held at ground. Thus, there is significant field leakage out of the buncher volume, resulting in a reduction of potential. This partially negates the effectiveness of the first electrode in the chain entirely, for the resulting potential on axis is not the required harmonic distribution. The field leakage from the entrance of the device also leads to a trough in the field distribution extending approximately 30 mm into the device, which coincides with the brow of the potential distribution.

The effect of geometric distortions of the bunching field from the perfect quadratic distribution due to the use of discrete electrodes has been reported previously [Hulett *et al.* (1991)], though no illustration of these distortions was presented. This present result is an important one, for it introduces a limit on the resolving power of a bunching apparatus using a large array of discrete electrodes. In the case of the Aarhus apparatus, the simulation of an idealised case as described above demonstrated fluctuations of ~ 90 ps in the output time of flight resolution. This limit may not at present severely restrict the experimentation possible using such a bunching device, but the possible future creation of sub-100 ps wide bursts of positrons would be hampered.

The initial energy of the positrons when the bunching potentials are activated was considered, by repeating the above time of flight simulation, but now starting the particles with a kinetic energy of 5 eV. The resulting times of flight are shown in fig. 3.4.1.3, and display lower time resolution than for the particles starting at rest. The particles starting closer to the exit have smaller times of flight than those further away, since the initial kinetic energy of these low x_0/l particles is of the order of that

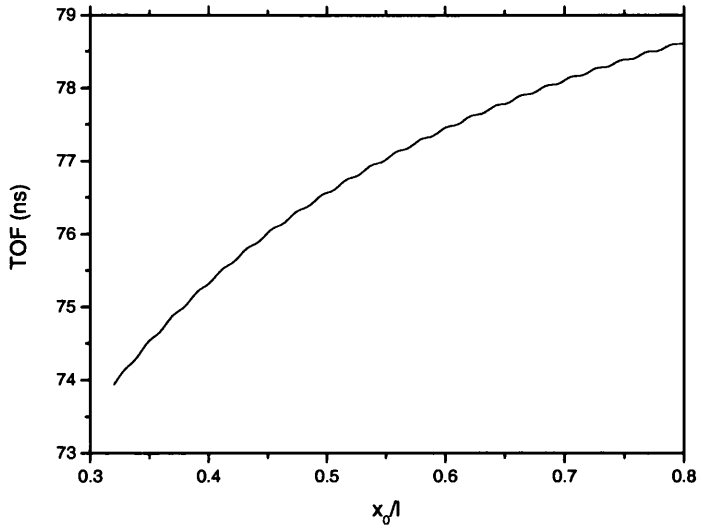

Figure 3.4.1.3: The times of flight for 5 eV particles, initially situated at various distances along the central axis of the apparatus, to reach the minimum of the 1 kV bunching potential difference. The bias pulse propagation delay, and the rise times of the electrodes, were not considered.

gained via the bunching potential difference they are subject to. The particles closer to the buncher entrance however have initial energies that are small compared to the potential difference experienced, and thus the kinetic energy enhancement produced for these particles is much smaller than that for the low x_0/l case. This effect leads to a larger spread in times of flight for positrons within the bunching volume compared to the case of the positrons starting at rest.

3.4.2 The effect of bias pulse propagation delay (PPD) and rise time

The idealised case of the particles starting at rest on axis was simulated once again, but now the initialisation of each electrode was delayed by the propagation of the bias pulse. The rise times for the electrodes were not yet considered. The result of this simulation is shown in fig. 3.4.2.1, and displays a spread in times of flight of ~ 11 ns, far larger than the associated case with no pulse propagation delay considered

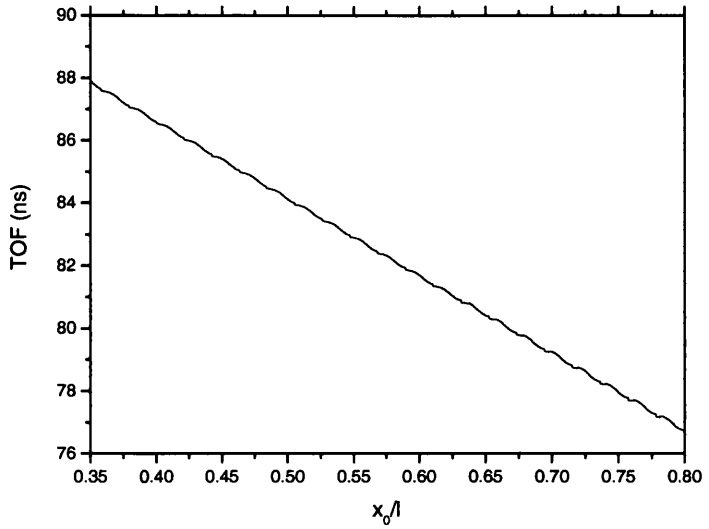

Figure 3.4.2.1: The times of flight for particles, initially situated at rest at various distances along the central axis of the apparatus, to reach the minimum of the 1 kV bunching potential difference. A pulse propagation delay of 10 ns was considered, while the rise times for the electrodes in the array were not.

(as shown in fig. 3.4.1.1). There are several important features of this time of flight spectrum that need to be explored.

First, the data clearly show that the positrons starting at larger x_0/l reach the focussing point far quicker than those starting closer to the buncher exit. This is due to these positrons being acted upon by the bunching field sooner than those particles further down the apparatus. The second feature of note is the times of flight for particles starting at high x_0/l positions. These are smaller than those seen in the case of no propagation delay, where the average time of flight was ~ 82.68 ns. Naively, this would not be expected, for the particles should see no difference between the two instances, for they are acted upon almost immediately in both cases. However, it is the very existence of the propagation delay in the second case which generates the smaller times of flight, for the electrodes are being initialised one at a time. Therefore, in the time it takes for the signal bias to travel from one electrode to the next electrode in the chain, there will be an enhanced potential gradient between the

two, for the second electrode is still at ground. This temporary high field has the effect of giving any particles within this region a momentarily higher acceleration. This phenomenon has a larger effect on the particles starting at high x_0/l positions, where the potential difference between the active and inactive electrodes will be greater, due to the quadratic variation of the electrode potentials down the apparatus. The particles starting at low x_0/l positions will also experience this extra acceleration, though the delaying action of the pulse propagation delay has more of an effect on the times of flight of these particles. Hence they take longer to reach the potential minimum than in the case of no pulse propagation delay. The final feature of note is that the oscillations in the times of flight are still present, suggesting that the addition of PPD does not mask this phenomenon.

As described in section 3.2, the rise time for each electrode was measured for the Aarhus apparatus, and found to vary linearly with respect to the electrode position within the chain. These rise times were next considered within the simulation procedure, with the times of flight recorded plotted in figure 3.4.2.2. The pulse propagation delay was not considered in this case, to separate out the individual effect that the rise times of the electrodes have on the output time of flight resolution. When comparing with the idealised case described by fig. 3.4.1.1, it can be seen that the introduction of the rise times leads to the times of flight for particles starting at low x_0/l positions to increase by ~ 10 ns, and those for the particles starting at high x_0/l positions to increase by ~ 20 ns. This implies that the particles starting nearer to the potential minimum have to wait for the full rise time of the electrodes in this region before they can traverse the restraining wall generated by the static electrodes. However, with the rise times of the electrodes near to the buncher

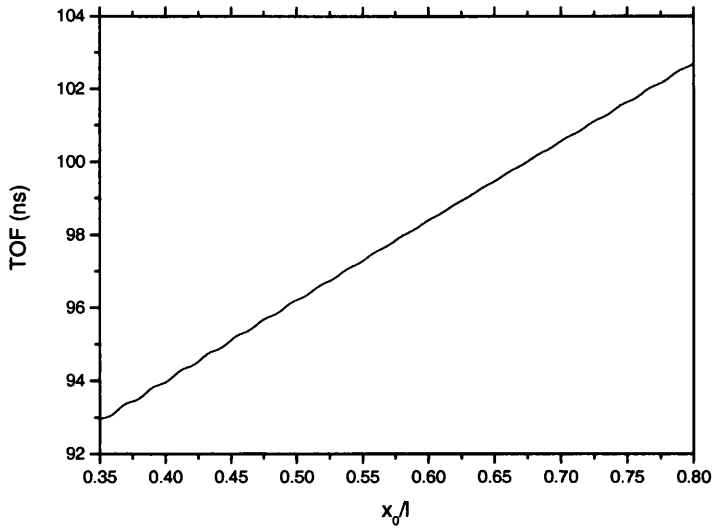

Figure 3.4.2.2: The times of flight for particles, initially situated at rest at various distances along the central axis of the apparatus, to reach the minimum of the 1 kV bunching potential difference. The rise times for the electrodes in the array were considered, but the bias pulse propagation delay was not.

entrance being ~ 30 ns, the time of flight data suggests that the particles starting in this region do not have to wait for the full length of time before moving closer to the potential minimum, as expected.

This simulation was repeated with a pulse propagation delay of 10 ns now included, generating the time of flight output presented in fig. 3.4.2.3. As seen previously, the addition of the PPD lowered the times of flight for particles starting at high x_0/l positions, and raised those for particles starting at low x_0/l positions. This skewing of the variation in times of flight improves the timing resolution of the output positron pulse from ~ 10 ns to ~ 2 ns, and highlights the dramatic effect that the bias pulse propagation delay can have on the capabilities of the buncher device. The result also raises the tantalising possibility of using the pulse propagation delay to 'tune' the device, to optimise the time width of the output positron bunches. As can be seen from the time of flight data presented in fig. 3.4.2.2 and fig. 3.4.2.3, when a pulse propagation delay of 10 ns is added to the system, the change in time of

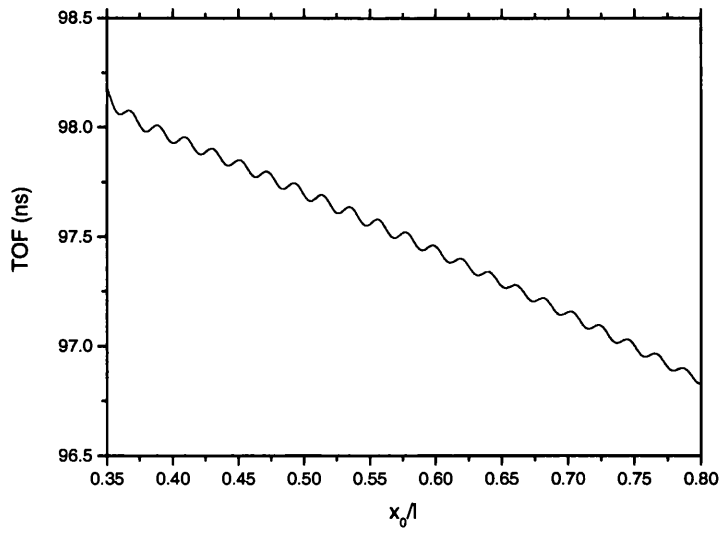

Figure 3.4.2.3: The times of flight for particles, initially situated at rest at various distances along the central axis of the apparatus, to reach the minimum of the 1 kV bunching potential difference. A pulse propagation delay of 10 ns, and the rise times for the electrodes in the array, was considered.

flight with varying x_0/l is skewed, and passes through a distribution with minimal time width. This is of course a feature of the desired timing resolution, where all of the particles have comparable times of flight independent of their position within the device when the bunching field is initialised. Thus, a pulse propagation delay in this case which is slightly smaller than 10 ns would produce a bunched output with enhanced timing resolution from the device. It is important to note that if a resistive chain had been used for the apparatus, the propagation time for the bias pulse down this chain would have been greater than 10 ns, and the time of flight data shown in fig. 3.4.2.3 would be skewed even further, leading to poorer timing resolution.

3.4.3 The effect of initial kinetic energy

It has been shown that the rise time for each of the electrodes, and the pulse propagation delay before which each of these electrodes is initialised, affect the

resulting timing resolution of an output positron bunch. Within this non-ideal apparatus, simulations were now carried out with the particles being started with an initial kinetic energy of 5 eV. The time of flight spectrum output is presented in fig. 3.4.3.1. This spectrum exhibits a temporal width of ~ 2.5 ns, and markedly different behaviour to that seen in fig. 3.4.2.3. The addition of initial kinetic energy for the particles has reduced the times of flight for all of the particles within the buncher volume, with those starting at low x_0/l positions taking ~ 8 ns less time, for these particles are now able to travel towards the potential minimum in the time it takes the bunching field to reach them. This also produces the small turning point seen at low x_0/l positions, where the particles are able to travel far enough along the axis to interact with the field generated by the static electrode biases (i.e. electrodes 33 to 47). The positrons starting at high x_0/l positions have their time of flight reduced by ~ 5 ns, less than that for the low x_0/l particles, for they see little difference in having a small initial velocity, which is quickly superseded when the bunching field accelerates them.

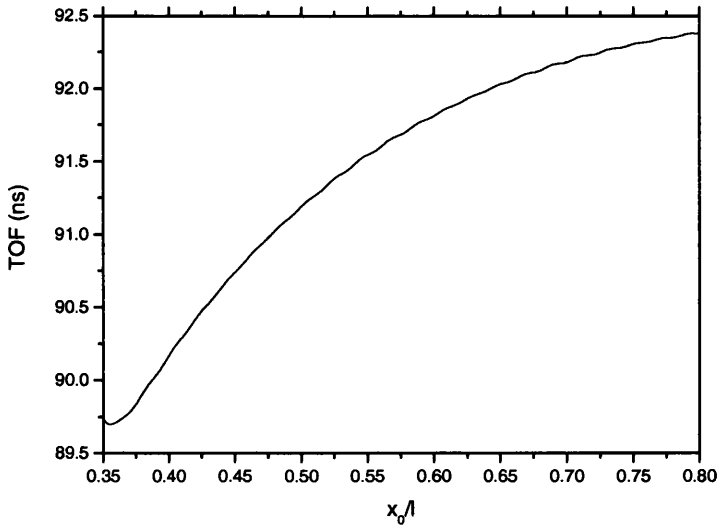

Figure 3.4.3.1: The times of flight for particles, initially situated at various distances along the central axis of the apparatus with 5 eV kinetic energy, to reach the minimum of the 1 kV bunching potential difference. A pulse propagation delay of 10 ns, and the rise times for the electrodes in the array, were considered.

It is important to note that so far in this discussion of the buncher simulation results, it has been assumed that the particles will be travelling towards the buncher exit should they have any initial kinetic energy. However, as was mentioned earlier, the device was designed to harness any positrons present within its volume at the moment of initialisation of the bunching field. This implies that there is an equal likelihood that particles travelling back towards the buncher entrance, having reached the restraining wall generated by the static electrodes, will be present within the bunched output.

Thus, the simulation of the non-ideal buncher was repeated, but now with the particles having an initial kinetic energy of 5 eV towards the entrance of the device, as opposed to towards the exit of the device as before. The times of flight for particles started at various points to reach the potential minimum were recorded, and are presented in fig. 3.4.3.2. The time of flight spectrum shows a different trend when compared to that of fig. 3.4.3.1, which can be understood by considering the mechanisms necessary to bunch the particles in this case.

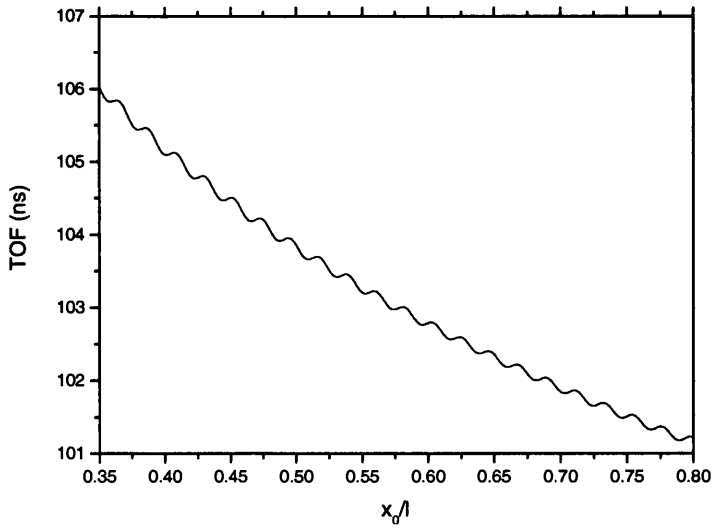

Figure 3.4.3.2: The times of flight for particles, initially situated at various distances along the central axis of the apparatus with 5 eV kinetic energy away from the buncher exit, to reach the minimum of the 1 kV bunching potential difference. A pulse propagation delay of 10 ns, and the rise times for the electrodes in the array, were considered.

To remove the backward travelling particles from the device when the bunching field has been initialised, they must first be brought to rest, before being accelerated towards the potential minimum. The time required to bring the particles to rest will vary with their starting point on axis. Those initialised at high x_0/l positions will quickly be subject to the bunching field, while those starting at low x_0/l positions have free travel away from the potential minimum until the bunching field reaches them. When this field does reach them, it will take longer to bring these particles to rest compared to those at high x_0/l positions, due to the much lower potential gradient they experience. When the particles are brought to rest, it may be assumed that the bunching field has reached them, so there is no pulse propagation delay to consider. It is likely that the electrodes will not be at their maximum bias however, so there is still some rise time to consider. If this is assumed to be small however, then the bunching of the particles from the apparatus, once they have been brought to rest, essentially takes the form of the idealised case previously considered, characterised by the time of flight spectrum shown in fig. 3.4.1.1. It would thus be reasonable to assume that the time of flight spectrum for these particles travelling away from the buncher exit will take the form of the bunching spectrum from the idealised case superimposed onto a slowing spectrum, characterised by decreasing times of flights with increasing x_0/l. It can be seen from fig. 3.4.3.2 that this indeed seems to be the case.

If the case of the particles starting with 5 eV towards the buncher entrance in the idealised case of no bias pulse propagation delay, and the electrodes initialising immediately, is now considered, it can be reasoned that a time of flight spectrum of the form shown in fig. 3.4.3.2 will be output once more, but with reduced times of flight. This is due to the times necessary to slow the particles to rest still being

dependent on the position of the particle on axis, due to the harmonic nature of the bunching potentials, but there being no delay time before this bunching field acts on them. This case was simulated, and the results presented in fig. 3.4.3.3 confirm this.

It was shown in the previous section that the timing resolution of the output bunch made up of the particles initially travelling towards the potential minimum when the bunching field is activated could be tuned by varying the bias pulse propagation delay. To explore whether this would be possible for the particles initially travelling away from the potential minimum, the above simulations were repeated with no pulse propagation delay present, but with the rise times of the electrodes still considered. The output time of flight spectrum is presented in fig. 3.4.3.4, and shows that the particles starting near to the potential minimum are now those with the smallest times of flight, for they no longer have free unrestrained travel away from the buncher exit while the bias pulse propagates down the capacitance chain. The particles starting at high x_0/l take the shortest time to be brought to rest, though this slowing time is longer than that in the case of 10 ns pulse

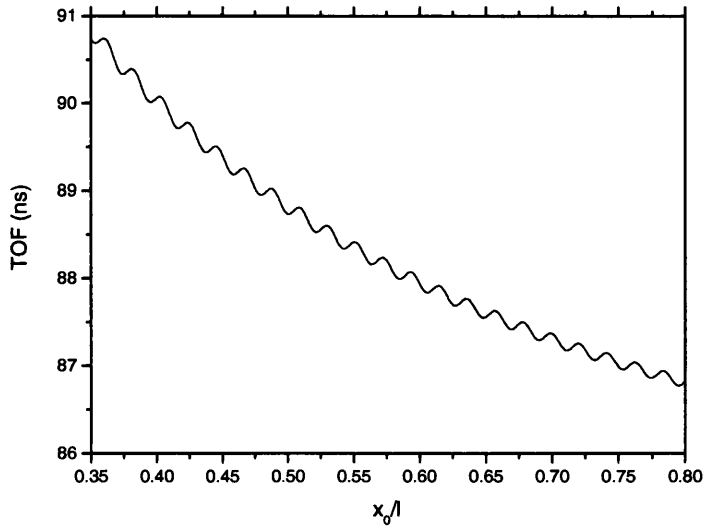

Figure 3.4.3.3: The times of flight for particles, initially situated at various distances along the central axis of the apparatus with 5 eV kinetic energy away from the buncher exit, to reach the minimum of the 1 kV bunching potential difference. The bias pulse propagation delay, and the rise times for the electrodes in the array, were not considered.

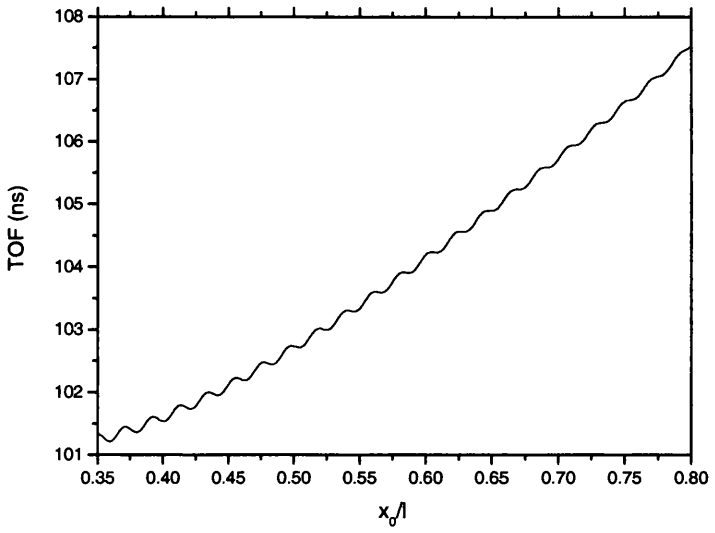

Figure 3.4.3.4: The times of flight for particles, initially situated at various distances along the central axis of the apparatus with 5 eV kinetic energy away from the buncher exit, to reach the minimum of the 1 kV bunching potential difference. The bias pulse propagation delay was not considered, though the rise times for the electrodes in the array were.

propagation delay, for the enhanced acceleration effect described in the previous section does not occur. Thus, the change in time of flight with varying x_0/l is skewed by the introduction of the pulse propagation delay, as seen before for the particles initially travelling towards the potential minimum. However, in this case, the introduction of 10 ns propagation delay modifies the timing resolution from ~ 6 ns, to ~ 5 ns. This suggests that the optimum timing resolution would occur for a pulse propagation time of less than 7.4 ns, which is not physical, for the reason stated in section 3.2. It is thus unlikely that the tuning ability in this case will be as successful as for that of the particles initially travelling towards the buncher exit.

It has been suggested [Xu *et al.* 1997] that the particles which are initially travelling away from the exit of the device when the bunching field is initiated, will synchronously arrive at a point located before the potential minimum. This theory was tested by simulating positrons initially travelling in this direction with a kinetic energy of 5 eV, with the rise time of the electrodes and a pulse propagation delay of

10 ns considered, and the time of flight to reach a number of points on axis measured. These points were distributed at intervals of 0.1 m around the potential minimum, to produce a series of data plots describing the evolution of the timing resolution of the positron bunch as it exited the device. These plots are shown in fig. 3.4.3.5, and clearly corroborate the suggestion of Xu *et al.* (1997), with a timing width of ~ 700 ps being found at a point 0.1 m before the potential minimum. This change in timing resolution is due to the variation in velocities of the particles within the bunched distribution, with those starting at higher x_0/l positions travelling faster as they leave the device than those which start at lower x_0/l positions. This produces a 'catching up' effect, as can be seen in fig. 3.4.3.5, with the particles starting nearer to the exit of the device being the first to reach the point 0.2 m before the potential minimum, but reaching the potential minimum itself last. This skewing of the data will of course at some point minimise the variation in the times of flight, and as such the bunched output will have an optimum timing resolution at this position on axis.

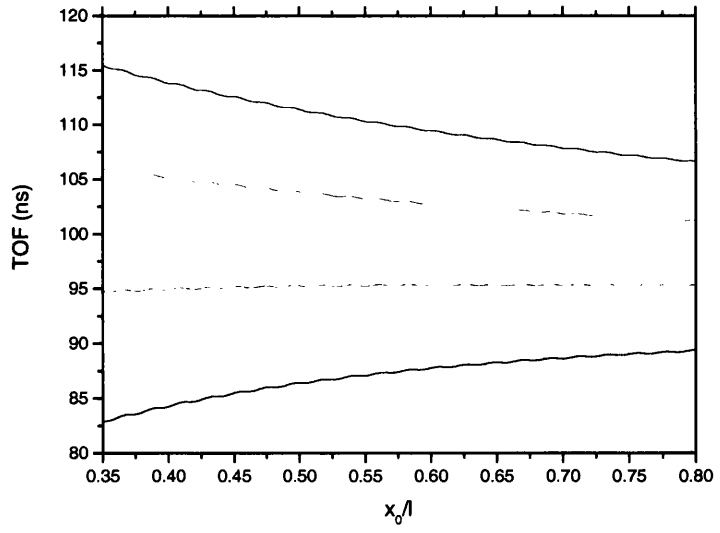

Figure 3.4.3.5: The times of flight for particles, initially situated at various distances along the central axis of the apparatus with 5 eV kinetic energy away from the buncher exit, to reach specific measurement points: 0.2 m before the potential minimum (black line); 0.1 m before potential minimum (red line); the potential minimum (pink line); and 0.1 m after the potential minimum (blue line). A bias pulse propagation delay of 10 ns, and the rise times for the electrodes in the array were considered.

Thus, it has been shown that the particles initially travelling away from the potential minimum when the bunching field is activated do have a focussing point, though it is inside the device itself. It would thus be useful to move this focussing position further along the axis of the device, ideally to a point outside of the bunching region entirely. To accomplish this, the data seen in fig. 3.4.3.5 would have to be skewed towards lowering the times of flight for particles starting at lower x_0/l positions with respect to those starting at higher x_0/l. The only variable described so far which has this effect on the time of flight data is the rise time of the electrodes in the array. It therefore seems that the only way that these particles could really be usefully harnessed outside of the apparatus is if the linear variation of the rise times of the electrodes was increased.

3.4.4 The timing resolution of the output bunch past the potential minimum

It was shown in fig. 3.4.3.5 how the output timing resolution of the particles that are travelling away from the exit of the device when the bunching field is activated is affected by the variation of velocities within this particle pulse, such that the time width of the ensemble varies as it moves towards the potential minimum. This is also the case for the particles which are travelling towards the device exit when the bunching field is activated, though as reported previously [Xu *et al.* (1997)], the focussing point in this case will exist at a position after the potential minimum. By inspecting the time of flight data shown in fig. 3.4.3.1, this idea can be accepted, for it is known that the particles starting at high x_0/l positions will have greater velocity at the potential minimum than those starting at low x_0/l positions, and thus their times of flight to further points will be smaller relative to the low x_0/l

particles. This will further reduce the time width of the bunched output, which implies there must exist some point after the potential minimum where optimum time resolution occurs.

To explore this hypothesis further, simulations were run with the motivation now more concerned with the time of flight of the particles past the potential minimum. As well as considering the rise times of the electrodes, and a bias pulse propagation delay of 10 ns, these simulations also involved far more realistic initial particle dynamics, including randomised pitch angle within a guiding magnetic field, a randomised initial energy within a Gaussian distribution, and a randomised starting position, as will be described below.

The randomised starting conditions for an initialised particle were produced using the standard rejection technique of finding a random number that satisfies a specific distribution function, *f(w)* say, which in this case was Gaussian in nature. The root of the rejection technique is to define another function *g(w)*, which is larger than *f(w)* over the range of interest. The function used for this task within the simulation procedure was of a constant value 1, as shown in fig. 3.4.4.1. This

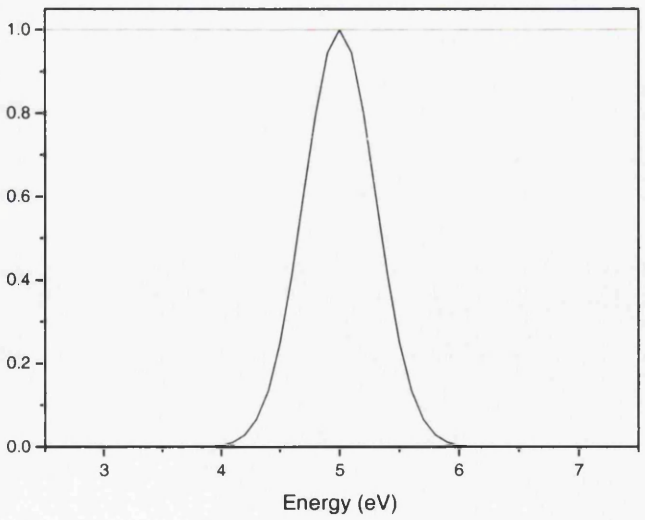

Figure 3.4.4.1: The functions used for the rejection technique method which generated the randomised energies for the simulations described, namely a Gaussian distribution of $\sigma = 0.3$ eV (shown in black), and a function of constant value 1 (shown in red).

selection of a $g(w)$ function was fairly unsophisticated, as will be explained later. A candidate value to be considered for use in the simulation was then randomly selected, within the confines of the energy range $2.5 < w < 7.5$ eV. The relevant values of $f(w)$ and $g(w)$ were then calculated, and the former divided by the latter. The result of this division was then compared to a new random number, and if larger, then the original w value is retained and used. If the random number is larger, then the w value is rejected, and a new w value is generated for consideration. Thus, the probability of a randomly selected w value being retained is Gaussian in nature, and as such, the values selected by this procedure will follow that distribution.

Thus, the condition to be met for a candidate value of starting energy to be retained and subsequently used in the simulation is

$$\frac{f(w)}{g(w)} = \frac{\exp\left[\frac{-(w-w_0)^2}{2\sigma^2}\right]}{1} = \exp\left[\frac{-((2.5+5R)-5)^2}{0.18}\right] < R', \qquad (3.4.4.1)$$

where R and R' are two independent random numbers.

It is clear to see that the efficiency of this technique is measured by the number of candidates which are retained, which is the ratio of the areas under the two distributions. In this case, where $g(w)$ was defined as a constant of 1 across the energy range of interest, the efficiency was ~ 0.15. This highlights that the majority of candidate energy values put forward are rejected, which will thus slow down the simulation procedure. However, as the simulations using this procedure were run overnight, combined with the simplicity of having a constant $g(w)$ value that could be ignored, this rejection technique was used to generate a Gaussian distribution of starting energies.

When a starting energy E had been accepted by the above procedure, it was then converted to a velocity, and resolved into x and y components by combining it with a randomised pitch angle θ_r

$$v_x = v\cos\theta_r = \cos\theta_r\sqrt{\frac{2E}{m}} \quad ; \quad v_y = v\sin\theta_r = \sin\theta_r\sqrt{\frac{2E}{m}}, \qquad (3.4.4.2)$$

where m is the mass of the positron, and the pitch angle is randomly selected between 0 and 30°, a range which is not greatly important due to the pitch angle being markedly reduced when the bunching field is initiated.

All of the particles considered within a single simulation run were started on axis from the same position of $x_0/l = 0.85$, and allowed to drift within the device for a randomised time of up to 650 ns, at which point the bunching field was initiated. The maximum drift time was set at this value for it was the time taken for a typical particle initialised using the above conditions to travel to the restraining wall, and then travel back to the entrance of the device. This drift time procedure was put in place to ensure realistic starting conditions for the simulated particles. A 50 Gauss magnetic field was also added to the simulation procedure, to confine these particles radially.

The timing resolution of the bunched output from the device was thus measured at various points after the potential minimum. This was achieved by recording the times of flight at each point, and placing these times in appropriate bins. The result was then convoluted with a Gaussian distribution (of full width at half height ~ 100 ps), to account for the resolution of the detector used originally at Aarhus. The recovered timing spectra are shown in fig. 3.4.4.2. It is clear to see that

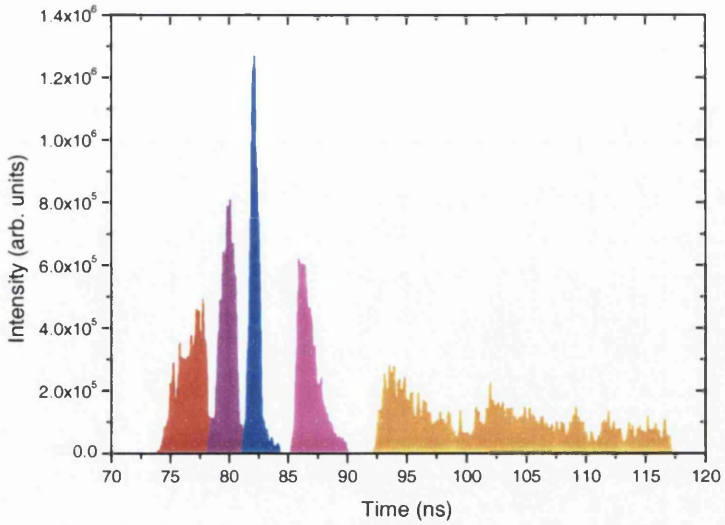

Figure 3.4.4.2: The timing spectra measured at various points: at the potential minimum (red); 0.035 m after the potential minimum (purple); 0.06 m after the potential minimum (blue); 0.11 m after the potential minimum (pink); and 0.21 m after the potential minimum (orange).

an optimum timing resolution is reached at a point in the region after the potential minimum, past which the particles begin to spread apart, since those which started at high x_0/l initial positions have overtaken those which started at lower x_0/l positions. This is highlighted by evaluating the widths of the timing spectrum at each measurement point, namely ~ 2.5 ns (FWHM) at the potential minimum, ~ 1.5 ns (FWHM) at 0.035 m past the potential minimum, ~ 0.8 ns (FWHM) at 0.06 m after the potential minimum, ~ 1.6 ns (FWHM) at 0.11 m after the potential minimum, and ~ 25 ns (full base width) at 0.21 m after the potential minimum. This trend is in line with the 1.2 ns FWHM resolution measured at Aarhus, where the detector was positioned 0.05 m after the potential minimum. However, the positrons initially travelling away from the buncher exit have not been considered here.

3.4.5 Non-harmonic potentials

It was shown in the previous sections that an optimum timing resolution for positrons initially travelling towards or away from the device exit can be found if the region of interest is moved from the ideal focussing point of the bunching potential minimum. This would be of great use within an apparatus which required the bunched positron output to be incident on a target, the axial position of which could be adjusted to allow for the optimum focussing point to be found for that specific device. However, if it is the case that the focussing point has to coincide with the potential minimum, then it would be useful to find a method with which the device could be tuned to achieve this.

With this is mind, the time of flight spectrum shown in fig. 3.4.3.1 for particles starting with a kinetic energy of 5 eV on axis, within a device subject to pulse propagation delay and electrode rise times, was studied. It can be seen that to optimise the timing resolution at this focussing point, the times of flight for particles starting at high x_0/l positions must be reduced in relation to those starting closer to the potential minimum. A possible way of achieving this would be to change the shape of the bunching potential with respect to displacement along the axis. This initially seems counter-intuitive, for the whole bunching effect, in theory, relies on the presence of a harmonic restoring force. It should be noted, however, that the imperfections in the bunching field generated by an array of discrete electrodes delays the high x_0/l particles more than those starting at low x_0/l positions, so these particles need to be subject to greater acceleration in order to focus the ensemble at the potential minimum.

By changing the potential distribution in the buncher, the potential at every point is changed, and thus, particles starting at either end of the device will have a new time of flight. Therefore, a specific part of the spectrum shown in fig. 3.4.3.1 cannot be adjusted independently of the rest of the spectrum, and as such, a measure is required of the change in potential produced.

For this measure, let us only consider the extremes of the time of flight spectrum, namely $x_0/l = 0.3$ and 0.8. If the maximum buncher potential is fixed at 1 kV, and the potential distribution on axis is governed by an exponent a, then the potential at any point x_0 on axis can be defined as

$$V\left(\frac{x_0}{l}\right) = 1000\left(\frac{x_0}{l}\right)^a . \qquad (3.4.5.1)$$

Thus, the variation in potential, ΔV, at any point on the axis from that for a harmonic case can be expressed as

$$\Delta V\left(\frac{x_0}{l}\right) = 1000\left\{\left(\frac{x_0}{l}\right)^a - \left(\frac{x_0}{l}\right)^2\right\}, \qquad (3.4.5.2)$$

and so the difference D between the variations at the two extreme points is defined as

$$D = \Delta V(0.8) - \Delta V(0.3) = 1000\left(0.8^a - 0.3^a\right) - 550 . \qquad (3.4.5.3)$$

If it is assumed that the output timing resolution will be improved when the positive variation in potential in the $x_0/l = 0.8$ case is larger in relation to the variation in the

$x_0/l = 0.3$ case, in other words when this difference D is positive, so that the particles starting further away from the focussing point are given enhanced acceleration in comparison to those starting close to the focussing point, then it would be useful to find when $dD/da = 0$. When calculated, this state was found to be satisfied by $a \sim 1.7$. This is revealed when D is plotted for a range of exponents, as shown in fig. 3.4.5.1, with the function taking a maximum value of ~ 5 at $a \sim 1.7$. These findings suggest that a non-harmonic potential with an exponent a slightly smaller than 2, may result in further enhancement in the timing resolution of the bunched output from the device. To test this prediction, simulations were carried out using such non-harmonic potential distributions. In each case, the first electrode in the chain was biased at 1 kV, the last electrode placed at ground, and those between defined by the distribution described by equation 3.4.5.1. The particles were started on axis with a kinetic energy of 5 eV, with the pulse propagation delay and rise times of the electrodes included as before. The times of flight of the particles to the potential minimum were recorded, generating the data series presented in fig. 3.4.5.2.

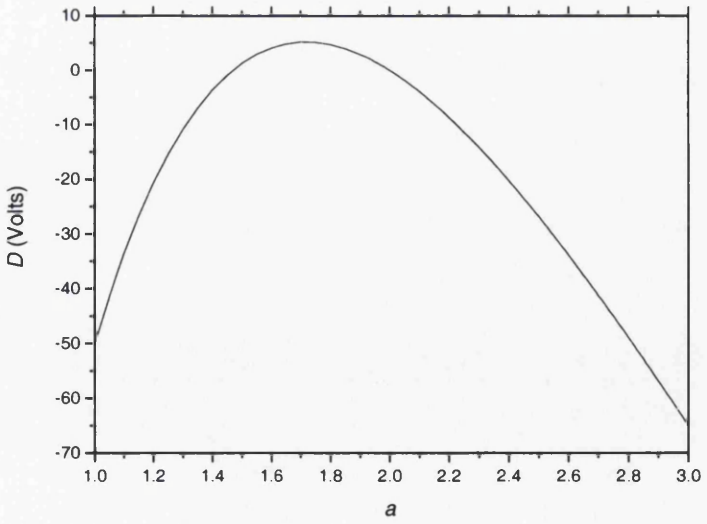

Figure 3.4.5.1: The change in function D with varying exponent a, such that $D(1.7) \sim 5$, and of course $D(2) = 0$.

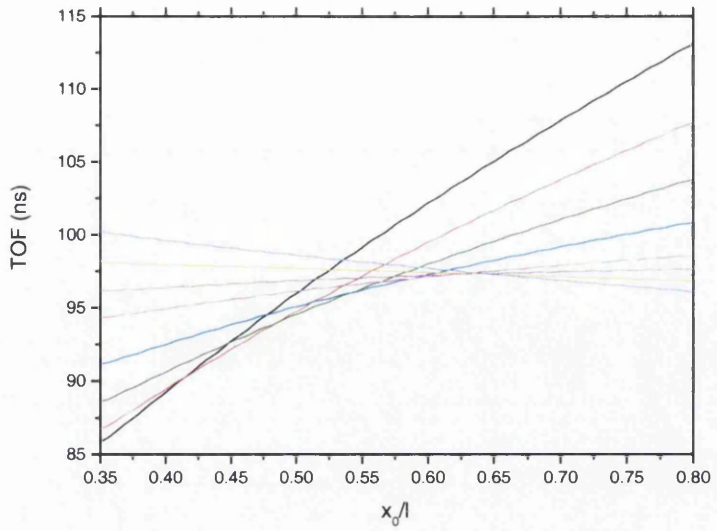

Figure 3.4.5.2: The times of flight for particles repelled from the device by various potential distributions: a = 1 (shown in black), a = 1.2 (red), a = 1.4 (olive), a = 1.6 (blue), a = 1.8 (magenta), a = 1.9 (purple), a = 2 (orange), and a = 2.1 (violet).

It can be seen that the time of flight spectrum in this case does pass through some optimum state when $1.9 < a < 2$. Thus, by careful manipulation of the exponent a in the potential distribution on axis within the device, the focussing point of the particles initially travelling towards the exit may be repositioned.

Chapter 4 : The Simulation, Construction and Testing of a Two-Stage Positron Accumulator

4.1 Introduction

The trapping of charged particles within a fixed volume may be accomplished by using either the Paul trap method, or the Penning trap method, both of which use hyperbolic electrode systems [Ghosh (1995)]. The two systems differ in how they confine the charged particles within their volume. The Paul trap uses electric fields oscillating at radio frequencies, whilst the Penning trap uses a magnetic field superimposed onto a static electric field. For the study of plasmas, a cylindrical Penning trap was developed [Malmberg and deGrassie (1975)], now termed the Penning-Malmberg trap, which was subsequently modified for accumulation of positrons [Surko *et al.* (1989); Murphy and Surko (1992)]. The principle of a rotating electric field (the so-called 'rotating wall') to increase the density of trapped non-neutral plasmas via spatial compression [Huang *et al.* (1997)] has also successfully been applied within positron accumulation devices [Greaves and Surko (2000), (2001); van der Werf *et al.* (2003)]. This effect is achieved by applying sine waves to the electrode, segmented azimuthally, within which the positron plasma is confined.

The trapping and accumulation of positrons using buffer gas cooling within a cylindrical Penning-Malmberg device allows for the production of dense pulses of particles, the population of which, as well as the time and energy width on exit, can be adjusted to suit the need of the experimentation in question. The Penning-Malmberg trap geometry consists of a uniform axial magnetic field used to confine the particles radially, whilst cylindrical electrodes are used to generate static electric

fields to prevent the particles from leaving the trap along the central axis (see fig. 4.2.2). The device is made up of electrode arrays of progressively larger diameter, with a specie of gaseous molecule (typically nitrogen) vented into the volume, to promote energy loss of the positrons via inelastic collisions. Due to the differing diameters of the electrode arrays, a pressure gradient is formed, with progressively lower pressures being experienced as the particles pass through the volume. The biases placed upon the electrode array are thus set up to allow the particles to enter the trap, but to confine them via energy-loss interactions with the buffer gas molecules. The flow rate of the buffer gas into the chamber is adjusted to promote one of these energy-loss interactions occuring during the time it takes a particle to traverse through to the restraining potential wall located at the end of the trap, and back towards the entrance where it may escape. Thus, a particle may become trapped within the device volume, and further interactions quickly reduce its kinetic energy to thermal levels, and confine it in the region of lowest electrostatic potential.

At this point, the ensuing positron ensemble which collects within the potential well of the device may be acted upon as desired. This may include the activation of a rotating electric field, or as described in section 4.4, the adjustment of the potential energy and physical size of the ensemble within the device by careful manipulation of the electrode biases.

4.2 Design, Construction and Control

The design of the accumulator at Swansea was based around the necessity for it to be able to operate at a frequency of 10 Hz. Thus, the long confinement times made possible using three-stage apparatus [Amoretti *et al.* (2004)], in which a

relatively low buffer gas pressure exists in the final stage, were not necessary, for the typical time between initial capture in the first stage to confinement within the second stage is of the order of ms. Thus, electrode pieces with internal diameters large enough to allow high pumping rates through the accumulation apparatus were not required, for steep pressure gradients were not necessary, permitting a miniaturisation of the accumulator dimensions.

The accumulator was required to provide large numbers of particles within each output pulse, to permit adequate positronium production for use in spectroscopy experiments via interaction of the positrons with a porous silica target. The goal was set at forming ~ 10^5 positronium atoms every 100 ms. This therefore placed a lower limit on the efficiency at which the device could operate, given the input flux of positrons was fixed by the ^{22}Na source activity. The timing resolution of the output pulses was fixed also, with a design goal of ~ 10 ns, to ensure they could be used efficiently alongside a pulsed laser source specifically set up to excite positronium atoms into Rydberg states. This would be accomplished by first exciting a 1s→2p transition, and then further exciting the atom using one of the following wavelength ranges: 688 – 780 nm (with a maximum power of 25 mJ at 750 nm), 778 – 911 nm (with a maximum power of 26 mJ at 816 nm), and 833 – 936 nm (with a maximum power of 16 mJ at 923 nm). For further details, please refer to Griffiths (2005).

The accumulator electrodes were to be used to generate electric fields to provide axial confinement of the particles within the system, while the radial confinement of the particles was to be provided by a strong magnetic field generated by a solenoid, through which the evacuated accumulation region would be positioned. The most compact design set-up for the solenoid, the vacuum tube, and accumulator, was to base it around a standard CF64 flange at either end of the

vacuum tube. This allowed the electrode pieces to be large enough to permit the beam to pass through unhindered, but also small enough to keep the system compact. The solenoid was wound onto a water-cooled former of diameter 0.14 m and length 0.68 m, comprising three layers of copper wire, of approximately 170 turns each, which provided a magnetic field on axis of ~ 450 Gauss, when powered at 44 A and 35 V.

The accumulator itself is shown in fig. 4.2.1, and comprised a first stage of 15 electrodes of internal diameter 16mm and length 24mm, and a second stage consisting of 5 larger electrodes, of diameter 41 mm and length 49 mm. Three mounting plates allow the two stages of the device to be held together. The length of the entire accumulator is thus ~ 0.65 m, comparable to that of the solenoid. The buffer gas is delivered into the system via a stainless steel tube, which screws directly into a bored hole in the eighth electrode in the first stage. The electrodes are wired to be biased independently, and are spaced using sapphire balls of 2 mm diameter, which also isolate them electrically.

The system is pumped by a Leybold 340M magnetically levitated turbomolecular pump (400 ls^{-1} N_2 pumping speed) through the first stage, and an APD8 cryopump (800 ls^{-1} N_2 pumping speed) through the second stage. The effect of the differential pumping on the device, generated by the differing internal diameters

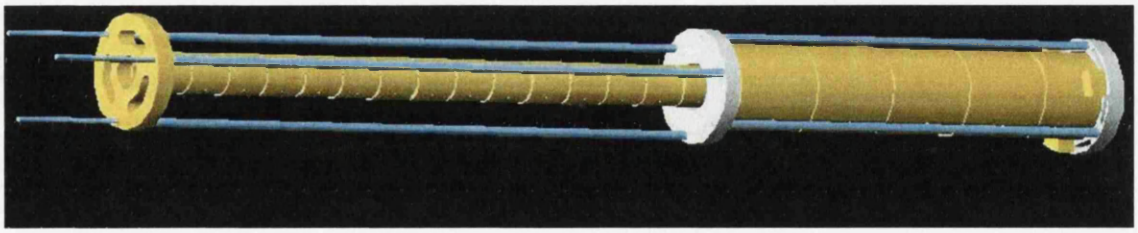

Figure 4.2.1: An AutoCAD technical diagram of the accumulator device as designed and constructed. The positrons enter the system from the left.

of the two stages, was estimated to produce a fall in buffer gas pressure from the value of approximately 10^{-3} mbar set in the first stage, to less than 10^{-4} mbar in the second stage. It should be noted that the buffer gas pressure during experimentation was measured using a cold cathode gauge in the vacuum chamber at the exit of the second stage of the accumulator, and thus no absolute measurement of the pressures within the device itself was possible.

Biasing of the electrodes within the accumulator was performed specifically to produce the four necessary components within the potential distribution in order for the device to work correctly, as shown in fig. 4.2.2. The first of these four components is the potential 'lip' that the particles must traverse in order to enter the accumulator volume. This is produced using the first electrode in the first stage, and is dependant on the bias placed on the neon moderator, for this determines the energy of the particles in the beam incident on the device. The moderator is typically biased at + 50 V, resulting in beam energy of ~ 55.5 eV as stated in section 2.3.2. The first

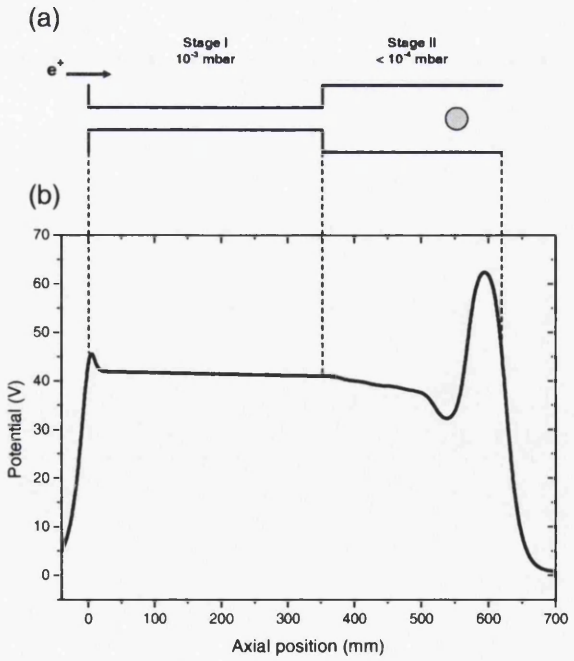

Figure 4.2.2: (a) a schematic diagram of the device; (b) the corresponding potential distribution on axis during the accumulation phase of the 'trap and dump' cycle. The particles were confined radially by an axial magnetic field.

electrode is thus biased at + 49 V, to allow the beam positrons into the trap, but to stop positrons which undergo an inelastic collision with a buffer gas molecule (and lose approximately 9 eV of kinetic energy) from escaping when travelling back through the first stage towards the accumulator entrance.

The second component in the accumulator is the small potential gradient placed over the remaining electrodes in the first stage. This is achieved by placing a + 42 V bias on the second electrode, and + 41 V on the last electrode within this stage, with the biases on the electrodes between falling linearly, accomplished via a series chain of high precision 1 kΩ resistors situated in an external bias box. This was put in place with the intention of studying how the efficiency of transporting positrons from stage one to stage two of the accumulator varied with differing potential gradients. However, this study was not conducted within the time-scale of this PhD scheme, and as such, a potential gradient of 1 V was used throughout experimentation.

The third component in the accumulator is the potential well itself, into which the particles will collect due to loss of energy via the inelastic collisions with buffer gas molecules in the second stage. This is produced by biasing the first three electrodes in the second stage to continue the potential gradient present in the first stage (+ 40 V, + 39 V, and + 38 V respectively), and placing a + 31 V bias on the fourth electrode.

The final component in the accumulator is the restraining wall produced by biasing the final electrode in the device, to ensure any beam positrons which pass through the device without interacting with the buffer gas cannot escape through the second stage into latter parts of the apparatus. This bias thus has a lower limit corresponding to the beam energy, and can be tuned to reduce the spatial distribution

of the particles within the potential well, which would naively be expected to improve the temporal resolution of the output pulse when the particles are released.

The admission of buffer gas to the accumulation volume, and the biases placed upon the electrode structure, were placed under a degree of computer control, using LabVIEW v7.0. This software package is quickly becoming the industry standard within laboratory research, allowing detailed programming capabilities to be executed relatively easily, and with a substantial support network providing software drivers to interface the package with a large number of physical devices.

The LabVIEW package is a G programming language, with coding taking the shape of a flow-diagram structure, instead of the more conventional text-based structure. This provides a far more direct programming interface, reducing coding time, and affording greater debugging simplicity. Two primary LabVIEW programmes were used in the accumulator experimentation, one controlling the introduction of buffer gas to the system, while the other was used to control the steering of the biases on the accumulator electrode structure.

The buffer gas programme was based around a simple PID (Proportional Integral Derivative) algorithm, designed to monitor the pressure measured within the system, and vary the bias across the piezo-electric input valve as appropriate to bring this pressure to that desired, by applying the equation

$$\text{Output} = Pe_{\text{p}} + \left(PI\int e_{\text{p}}dt\right) + PD\frac{de_{\text{p}}}{dt}. \qquad (4.2.1)$$

The variables P, I and D will be explained below, and e_{p} is defined as the error in the measured pressure, calculated by simply subtracting the feedback pressure reading from the setpoint pressure.

The PID algorithm is common in many experimentation devices requiring a forced steady state, and combines three distinct operators. The proportional operator *P*, also referred to as "gain", has a dominant effect on the PID output, and as can be seen from equation (4.2.1), must be non-zero for the algorithm to operate. If only this operator is used, then there must be a non-zero error for the PID control to still function, immediately placing a limit on the success of the algorithm.

The integral operator *I*, also referred to as "reset", is multiplied by the error over time to produce the integral term in the full equation. The addition of the integral term to the proportional term removes the necessity for an error to be present in the feedback pressure reading for the algorithm to still function. This operator is especially important for steady state applications where the error is very small, for it holds the PID output constant, applying slow changes where necessary.

The derivative operator *D*, also referred to as "rate", is multiplied by the rate of change in error over time, allowing this term to respond quickly to rapid changes in the error signal, and adjust the PID output as necessary. This especially helps to minimise overshooting of the setpoint value, by monitoring the quickly decreasing error signal as the true pressure approaches the desired value. During steady state applications, *D* is usually set to zero, to prevent unnecessarily large reactions to small fluctuations in the feedback signal.

The front panel of this "PID Buffer Gas" programme is shown in fig. 4.2.3. For the buffer gas pressures used during accumulation experimentation, the stability of the programme in keeping a constant desired pressure within the range of 0.02 to 3.50×10^{-5} mbar was tuned by adjusting the PID settings until the optimum combination of parameters was found. These are: P = 0.005, I = 0.2 minutes, and D = 0.01 minutes. The inaccuracy in the actual pressure in relation to that desired is

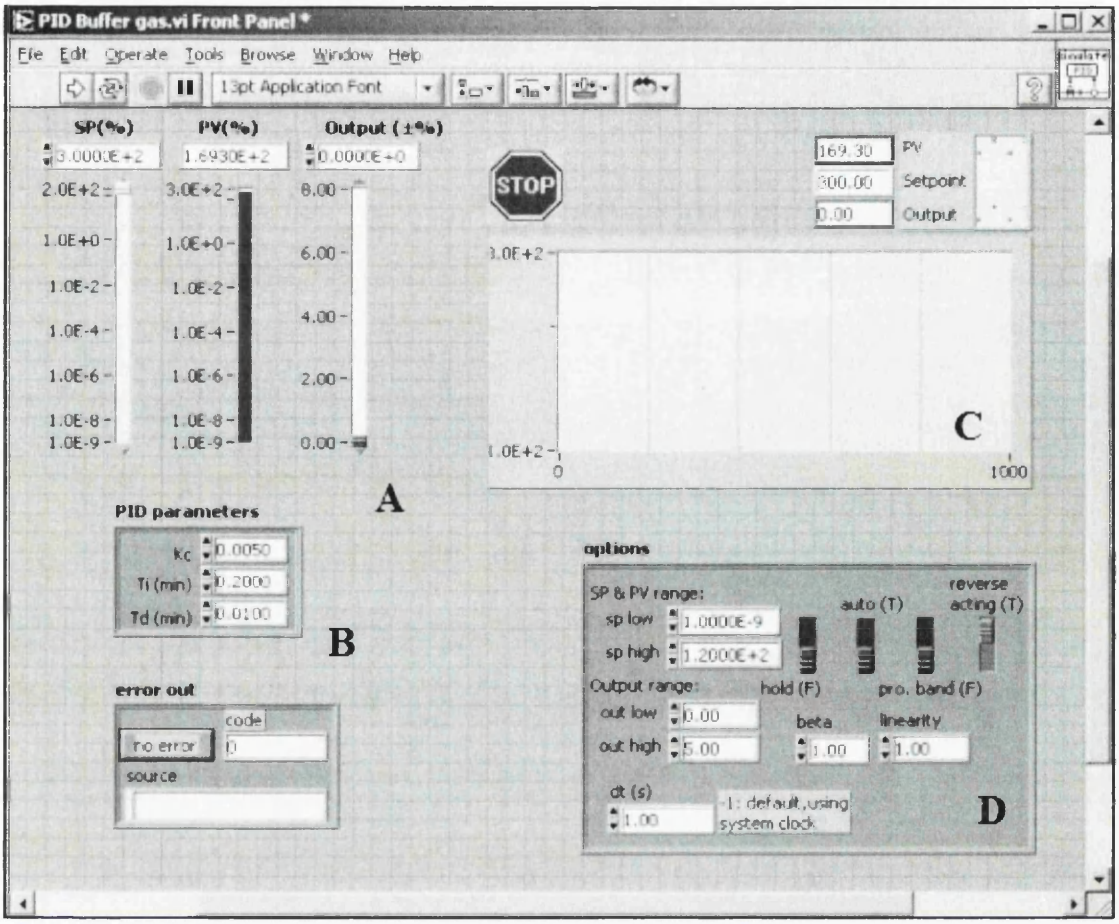

Figure 4.2.3: The front panel of the LabVIEW programme designed to monitor and adjust the pressure within the accumulator as appropriate during experimentation, featuring: (a) gauges showing (from left) desired pressure, actual pressure, and output to piezo-electric valve; (b) the PID settings to bring actual pressure towards desired pressure; (c) plot to show variation of actual pressure with time; and (d) higher settings for the PID calculations (including a manual over-ride).

clearly to be expected to a greater degree at lower pressures. This is an explanation of the large uncertainties obtained in the results taken at these pressures, as featured in section 4.3.

The programme to control the biases on the accumulator electrodes during experimentation was less complicated than that described above, though the application of these biases to the apparatus itself was more complex, as shown in fig. 4.2.4.

The desired bias magnitudes V_d were set within the programme, which then applied a calibrated operation to convert these magnitudes to corresponding signal

ELECTRODE	Front	Grad High	Grad Low	Big1	Big2	Big3	Big4	Big5
ACCUMULATION BIAS (V)	49	42	41	40	39	38	31	70
DUMPING BIAS (V)	100	42	41	40	39	38	31	0

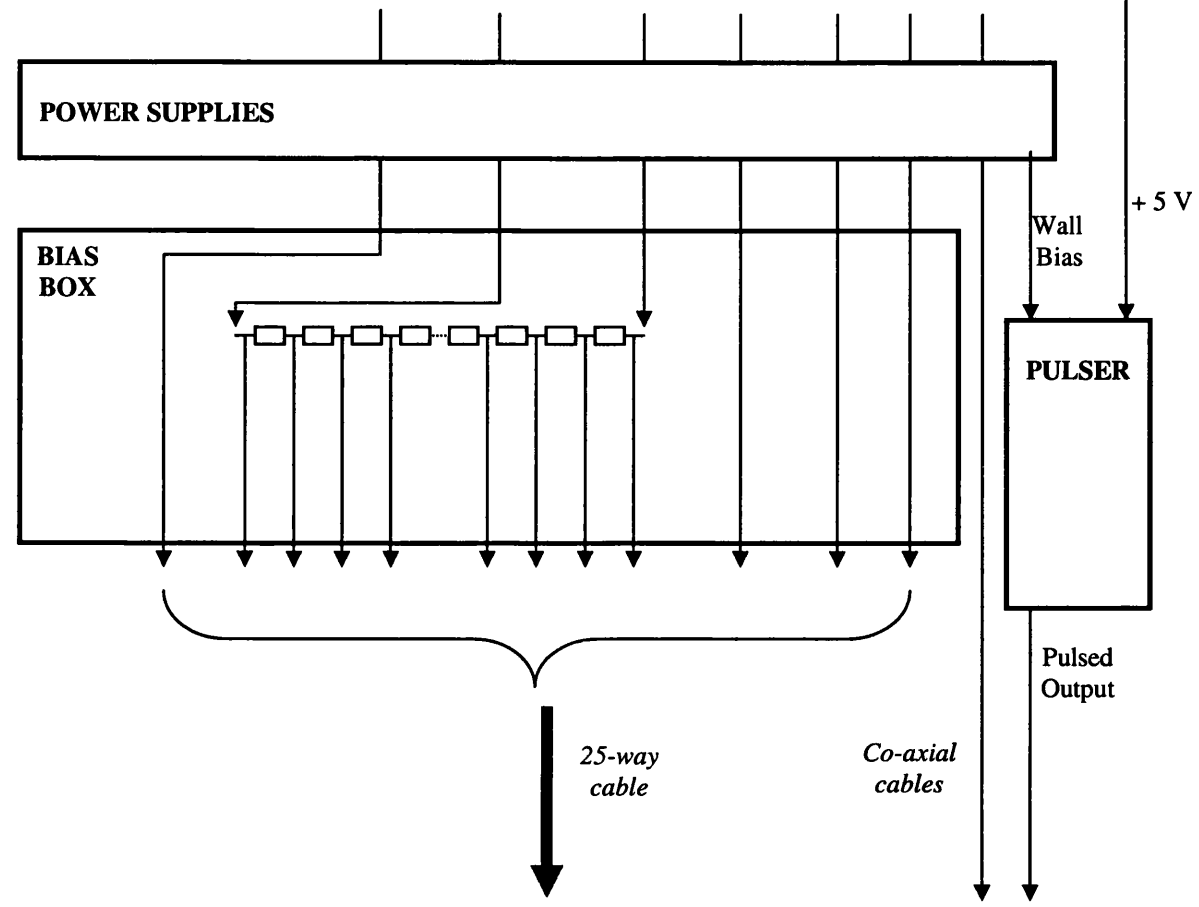

Figure 4.2.4: A simplified diagram showing the application of the biases output from the LabVIEW programme to steer the accumulator electrode system.

voltages V_s of between 0 and 10 V. This was required, for the shielded BNC connector block (National Instruments NI BNC-2110) from which the biases were output was incapable of providing the biases required. These signal voltages were then sent to external power supplies, which converted them back to the desired bias stated within the programme. This was true across all the output channels except for the final electrode, which was to be pulsed, and thus required a slightly different set-up. Here, an arbitrary bias of + 70 V was set within the programme, in order for a + 5 V bias to be output from the shielded connector block. This signal bias was used to

trigger the pulser unit, which provided the desired electrode bias separately, via manual control of one of the power supplies.

The biases from the power supplies for all but the final two electrodes were then sent through the external bias box. Within this box, the "grad high" and "grad low" biases were placed across the series chain of high precision 1 kΩ resistors, from which the biases for the electrodes in the first stage of the accumulator were collected. The output from this bias box was mediated via a 25 channel cable which plugged into a feedthrough flange on the apparatus, from which each individual bias was delivered to the relevant electrode by a kapton-coated single core cable within the system. The biases for the final two electrodes were delivered to the system via standard high voltage BNC coaxial cables, and transmitted to the relevant electrode within the system by kapton-coated coaxial cables.

4.3 Results

Studies of the accumulation capabilities of the two-stage trapping system consisted of a number of lifetime measurements being taken across a broad range of buffer gas pressures. At a fixed buffer gas pressure, the accumulation time was varied from 1 ms, up to times where it was clear that the output yield had converged to some maximum value (i.e. when the rate of trapping had equalled the rate of annihilation). The output yield was calculated by measuring the radiation generated by the output positrons annihilating on a target situated ~ 0.3 m from the end of the accumulator. A CsI photo-diode detector was used to measure this radiation. It was located a sufficient distance away from the point of annihilation to ensure no saturation effects would occur within the detector at a position where the

measurement efficiency was known via the coincidence measurements described in section 2.3.2.

The biases used for initial measurements were, as shown in fig. 4.2.2, with + 65 V bias being placed on the final electrode during the accumulation phase. The lifetime data from one such measurement is shown in fig 4.3.1, where the pressure measured at the top of the cross piece located directly after the accumulator was fixed at 2.5 x 10^{-5} mbar. It can be seen that the positron yield converges to ~ 3 x 10^5 in less than one second. To acquire more precision in these numbers (i.e. $N(\infty)$, the yield at long accumulation times, and τ, the lifetime of the particles in the system), the data were fitted to

$$N(t) = N(\infty)\left(1 - \exp\left(-\frac{t}{\tau}\right)\right), \qquad (4.3.1)$$

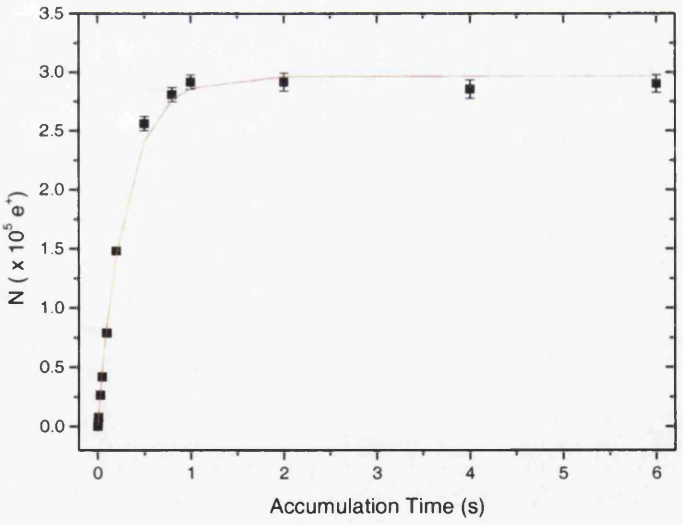

Figure 4.3.1: The lifetime data gained from successive accumulations of differing lengths of time, at a fixed buffer gas pressure of 2.5 x 10^{-5} mbar. The fit to this data is shown in red, with fitting parameters $N(\infty)$ = (2.97 ± 0.04) x 10^5, and τ = 0.297 (± 0.009) s.

with

$$N(\infty) = R\tau, \qquad (4.3.2)$$

where R is the rate of trapping of the positrons within the accumulator volume.

The same measurement and fitting procedure was carried out at a number of different pressures, allowing several studies to be made into the accumulation efficiency and characteristics of this two-stage system. One such study is the behaviour of $N(\infty)$ with varying pressure. The behaviour of this maximum yield with varying pressure would be expected to be characterised by

$$N(\infty) = \frac{fI_0(1-\exp(-DP))}{BP}, \qquad (4.3.3)$$

where: f is the branching ratio of the electronic excitation cross section of a N_2 molecule in a positron- N_2 collision (the positron energy loss mechanism responsible for trapping), to other processes which result in losses of the positron (e.g. positronium formation); I_0 is the number of moderated positrons entering the accumulator volume per unit time; the (1 - exp(-DP)) term describes the probability of a positron- N_2 collision within the first stage of the accumulator, whose behaviour dictates a rapid loss of capture efficiency at reduced buffer gas pressures, and the $\frac{1}{BP}$ term expresses the lifetime of the positrons which are captured within the accumulator, which is a simplified form of the full expression

$$\frac{1}{\tau} = BP + u, \qquad (4.3.4)$$

where the term BP characterises the annihilation rate of positrons on the N_2 molecules, and the constant u characterises all N_2 pressure independent losses of positrons. It is assumed in equation (4.3.3) that $u = 0$, which will later be shown to be valid. The $\frac{1}{BP}$ term predominantly describes the behaviour of the positrons in the second stage, where they spend the majority of the accumulation time.

However, equation (4.3.3) fails to fit the behaviour displayed in the $N(\infty)$ measured data. It can be shown why this is so by considering the output yields from the ideal accumulator characterised by equation (4.3.3), as shown in fig 4.3.2, constructed using the fitting parameters shown later in fig 4.3.4. It is clear that both the ideal and measured data plots show similar behaviour at high pressures, but are very different at lower pressures. From equation (4.3.3), we see that the ideal behaviour tends towards a constant value of $\frac{fI_0D}{B}$ at low pressures, while fig. 4.3.4 shows the real data display a linear increase. This implies some loss mechanism occurring within the accumulator not previously considered.

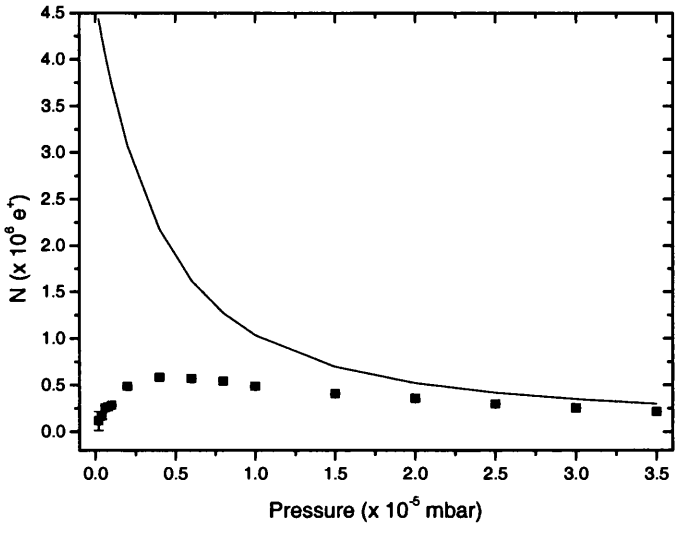

Figure 4.3.2: A comparison plot between the real output yield measured in accumulator (points), and that of an ideal accumulator (black line).

If we reconsider equation (4.3.3), we see terms describing initial capture of low energy positrons in the first stage of the accumulator, and the eventual loss of the thermalised positrons in the second stage. However, there has been no mention of the transfer of the particles from the first to the second stage in this scheme, which has been implicitly assumed as being of unit efficiency. If we consider that this is not the case, and instead explore the effect of a pressure independent loss between the two stages, parameterised by some constant F, then a further branching ratio may be added to equation (4.3.3) of the form

$$\frac{EP}{(EP+F)}, \tag{4.3.5}$$

where E is also a constant, and the term EP characterises the transfer efficiency of positrons from the first to the second stage. This extra term modifies equation (4.3.3) to become

$$N(\infty) = \frac{fI_0E(1-\exp(-DP))}{B(EP+F)}. \tag{4.3.6}$$

It can be shown by inspection that both equations (4.3.3) and (4.3.6) have the same high pressure limit of $\frac{fI_0}{BP}$, as exhibited in fig. 4.3.2, but that the introduction of the extra branching ratio to equation (4.3.3) now alters the low pressure limit to $\frac{fI_0EDP}{BF}$, which shows linear pressure dependence as observed in fig. 4.3.4.

Thus, the data were also fitted using the simplified form of equation (4.3.6) shown below, to investigate whether this extra loss mechanism could account for the unexpected $N(\infty)$ behaviour, in other words

$$N(\infty) = \frac{a(1-\exp(-bP))}{c+P}, \qquad (4.3.7)$$

where $a = \frac{fI_0}{B}$, $b = D$, and $c = \frac{F}{E}$. The constant B can be obtained independently by applying equation (4.3.4) to the positron lifetimes at various pressures, found previously by fitting the positron yields measured at fixed pressures (and varying accumulation times) to equation (4.3.1). The gradient of the expected linear behaviour would give the constant B, and the y-axis intercept the constant u. The magnitude of u would possibly give an indication as to the levels of impurities in the vacuum within which the accumulation experiments were conducted. The vacuum condition within the apparatus is an important consideration, for even trace amounts of large molecules can lead to pronounced positron loss. Examples of such molecules include hydrocarbons, because of the large interaction cross-section due to the possible excitation of low-energy vibrational modes [Surko *et al.* (1988); Marler *et al.* (2004)], and water, due to the polar nature of the molecule resulting in a dipole interaction with longer range than that for a non-polar alternative [Iwata *et al.* (1995)]. The relevant lifetime plot is shown in figure 4.3.3, showing that a good fit is found to equation (4.3.4), and that the constant u is negligible at typical (high) accumulation pressures used. The data seems to diverge from linearity at higher pressures, suggesting the lifetimes are larger than that expected within this region.

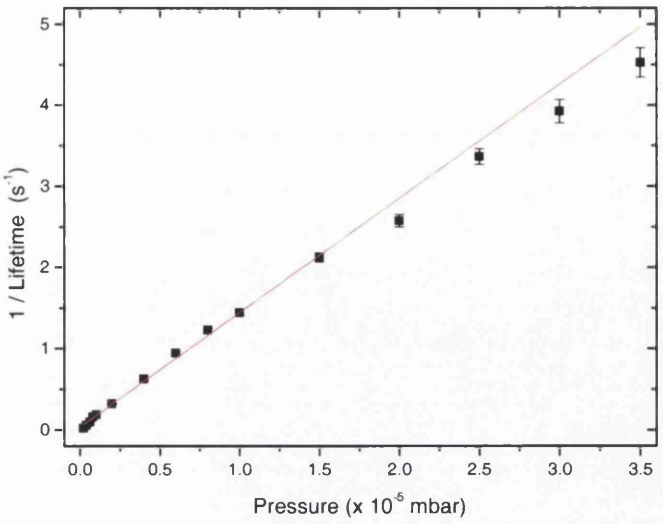

Figure 4.3.3: The variation of $1/\tau$ with pressure. The data was fitted linearly to equation (4.4.4), giving $B = (1.409 \pm 0.015) \times 10^5$ mbar^{-1}s^{-1}, and $u = 0.0397 (\pm 0.005)$ s^{-1}.

A fit of the $N(\infty)$ data to equation (4.3.7) was performed, with no constraints placed on the three fitting parameters, the result of which is shown in fig. 4.3.4. A good fit to the data is seen, showing that the revised expression has shed some light on the source of the unexpected behaviour of the accumulator. The two constants a and B can now be used to calculate the branching ratio of trapping cross sections to cross sections of other processes which resulted in losses of the positrons from the

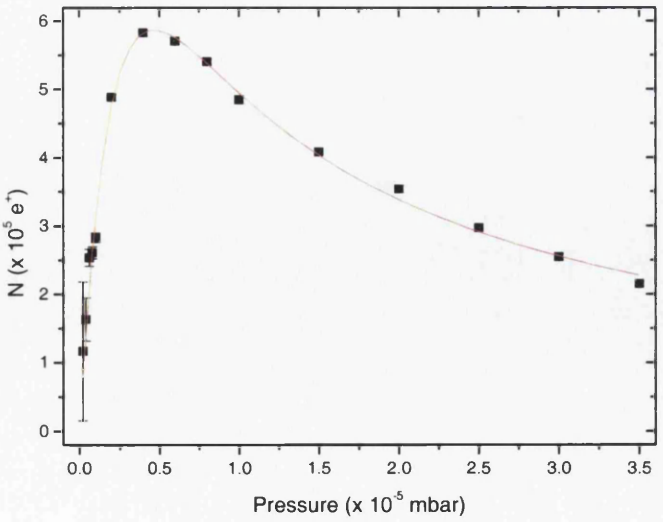

Figure 4.3.4: A plot of N(∞) against P, fitted using equation (4.4.7) with parameters a = 10.477 (± 0.186) mbar, b = 4.42 (± 0.15) x 10^5 mbar^{-1}, and c = 1.00 (± 0.04) x 10^{-5} mbar.

system, giving $f = 0.43$ ($\pm$ 0.01). Thus, nearly one half of the particles that enter the first stage of the trap undergo an inelastic collision with a N_2 molecule, and are thus captured by the system. This is clearly a strong confirmation of the feasibility of a two-stage positron accumulator.

The source of the extra loss mechanism was not located explicitly, though one strong candidate is misalignment of the electrodes and/or the guiding magnetic fields, which may force the positrons to drift to the inner walls of the accumulator during their multiple passes through the system at lower buffer gas pressures.

The positron yield was not the only important parameter of the accumulator output to be considered however. For later uses of the positrons further down the beam-line, the energy and time resolutions of the output pulse needed to be known, and optimised.

The CsI photo-diode detector was not useful for the time resolution measurements, for its μs response time rendered it incapable of resolving the expected positron pulse width of ~ ns. Therefore, a channeltron electron multiplier (CEM) installed within the final chamber of the apparatus (see fig. 5.2.1 for the location of this chamber) was used for these experiments. It was also found that the CEM was preferable for the energy resolution experiments to the CsI photo-diode detector, due to a superior signal-to-noise ratio.

The timing resolution of the output pulse was measured by directly transferring the oscilloscope signal trace to a data file using the LabVIEW v7.0 software package. These data series are plotted alongside one another in fig. 4.3.5. The presence of two peaks is seen in the timing spectra of the output pulse, with a re-distribution of counts between the peaks seemingly taking place as the bias of the final electrode used for accumulation is lowered. The possibility that the shape of the

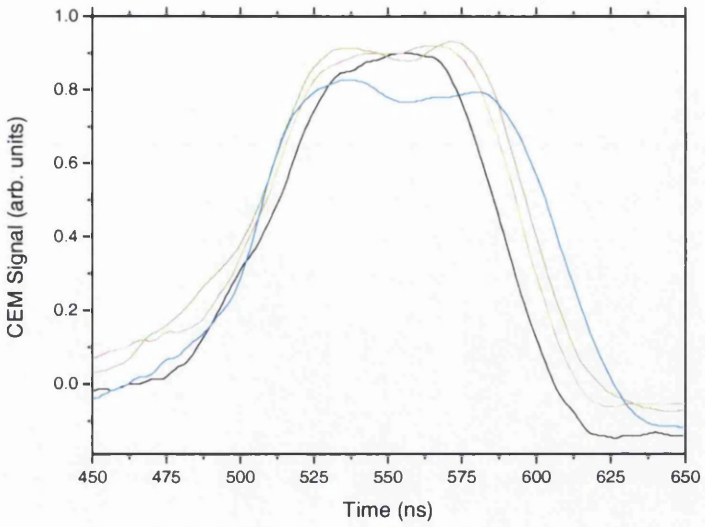

Figure 4.3.5: The timing spectra of the output pulse after 1 s accumulation, with varying bias on the final electrode: 139.7 V (blue), 130 V (green), 120 V (red), and 110 V (black).

potential well was affecting these spectra was further explored by adapting the electrode biases to produce a wider well, as shown in Table 4.3.1. The timing resolution of the output pulse of positrons from this modified voltage distribution was then measured, as well as that for the original potential distribution, as shown in fig. 4.3.6. It can be clearly seen that modifying the potential distribution within the accumulator to widen the well has the effect of moving the two peaks apart. This phenomenon may be understood by considering the motion of the particles within the potential well, which may be approximated by simple harmonic motion along the axis of the apparatus. Thus, at the moment of initialisation of the dump phase, a

TABLE 4.3.1: THE BIASES ON THE ELECTRODES USED TO PRODUCE A WIDER WELL FOR ACCUMULATION AND SUBSEQUENT PULSING.

ELECTRODE	Front	Grad High	Grad Low	Big1	Big2	Big3	Big4	Big5
ACCUMULATION BIAS (V)	49	42	41	40	39	32	32	139.7
DUMPING BIAS (V)	100	42	41	40	39	32	32	0

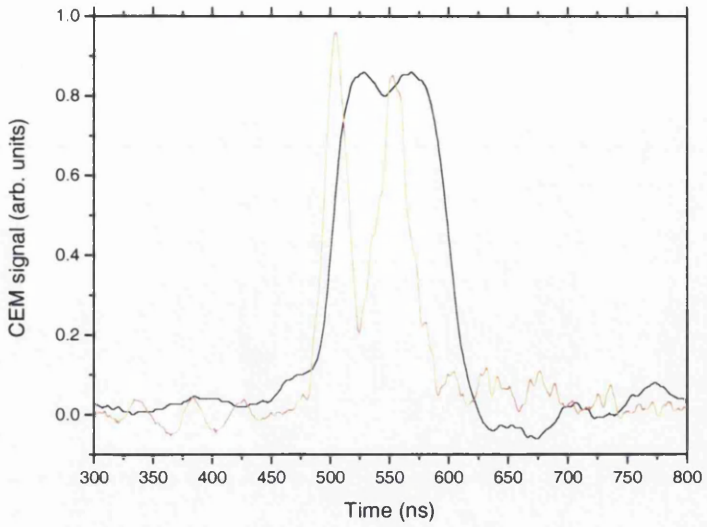

Figure 4.3.6: The timing spectra of the output pulse after 1 s accumulation, with varying numbers of electrodes used to produce the potential well: one electrode of bias + 31 V (black), and two electrodes of bias + 32 V (red).

particle would most likely be near the walls, rather than the central region, of the well. This may explain why widening the potential well would result in the increase in the spacing of the peaks. There may therefore be two distinct distributions of positrons leaving the system, with their spacing in time dependant on their axial spacing (i.e. the apparent width of the potential well seen by the thermalised particles). This phenomenon suggests that a plasma state is not formed within the potential well during the accumulation cycle, for single particle behaviour is seemingly being displayed. This suggestion can be checked by estimating whether a positron plasma would be formed within the two-stage accumulator. The Debye screening length λ_D [Debye and Hückel (1923)] of such an ensemble, the distance over which the positrons would screen electric fields in the plasma, is given by

$$\lambda_D = \sqrt{\frac{\varepsilon_0 kT}{ne^2}}, \qquad (4.3.8)$$

where ε_0 is the permittivity of free space, k is Boltzmann's constant, T is the temperature of the heat bath within which the positrons are located (which will be assumed to be room temperature), n is the particle density, and e is the elementary charge of the particles. If we assume that the ~ 6 x 10^5 positrons confined in the second stage of the apparatus occupy a cylindrical volume of a radius and height of ~ 5 mm, then the resulting particle density is ~ 10^{12} m^{-3}. The subsequent Debye length for this system is then ~ 1 mm. The width of the potential well was found by simulating the potential on axis within the device during the accumulation phase, using a similar method to that described in section 3.4.1, and is presented in fig. 4.3.7. Thus, the Debye length is of the same order as the width of the well. However, a requirement for a plasma state to exist is that the Debye length must be much smaller than the shortest ensemble dimension, which is not the case here, though the conditions are close to that of the plasma domain. Therefore, it is unlikely that a plasma state is being formed within the accumulator.

The energy spectrum of the output positron pulse from the accumulator was

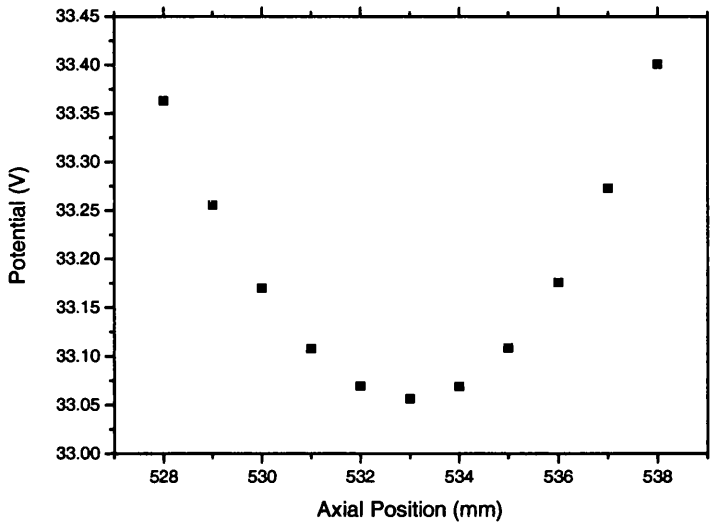

Figure 4.3.7: The simulated potential well on axis, present during the accumulation phase of the device. It suggests that a positron of ~ 0.1 eV would experience an effective well width of ~ 5 mm.

TABLE 4.3.2: THE BIASES ON THE ELECTRODES USED WHILE MEASURING THE ENERGY SPECTRUM OF THE OUTPUT POSITRON PULSES.

ELECTRODE	Front	Grad High	Grad Low	Big1	Big2	Big3	Big4	Big5
ACCUMULATION BIAS (V)	49	42	41	40	39	38	31	139.7
DUMPING BIAS (V)	100	42	41	40	39	38	31	0

measured by placing a known bias onto a grid specially mounted in front of the CEM detector. As this bias was varied, so would the number of positrons within the pulse retarded from the detector, and back towards the accumulator. The signal output of the CEM resulting from those positrons which overcame the retarding bias was fed into the oscilloscope, from which a signal height could be measured for each corresponding retarding bias. An accumulation time of 100 ms was used at a fixed buffer gas pressure, with the biases placed upon the electrodes within the accumulator for these measurements shown in Table 4.3.2. The last electrode was pulsed.

The results from this experiment are shown in fig. 4.3.8. The data show a clear drop from the full signal height at low retarding biases, to a background signal

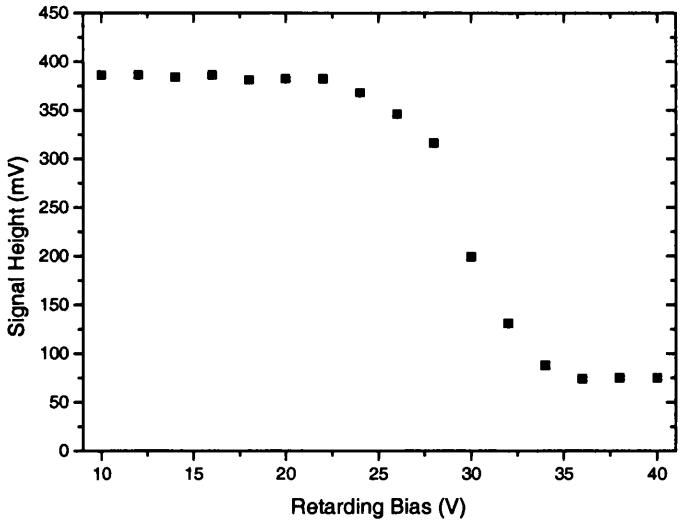

Figure 4.3.8: The change in signal height as measured from the CEM detector via an oscilloscope, with varying retarding bias, after an accumulation of positrons for 100 ms.

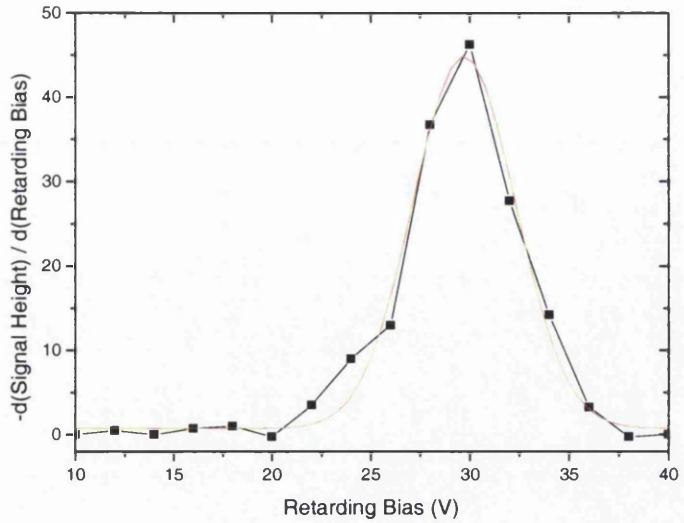

Figure 4.3.9: The outcome of differentiating the signal height results shown in fig. 4.3.8 with respect to retarding bias. A Gaussian fit to this data is shown in red. The connecting line between points is included only to aid the eye.

height at high retarding biases. Using the Origin v7.0 software package, these signal data were differentiated with respect to the varying retarding bias, to produce a spectrum of the particle kinetic energy parallel to the guiding magnetic fields. This spectrum is shown in fig. 4.3.9, with a Gaussian fit to the data shown in red. This fit is centred at ~ 29.7 V, with a full width at half maximum height (FWHM) of ~ 6.1 V. This width is a factor of ~ 10 larger than expected, which may suggest that there are significant space charge effects occurring within the potential well during accumulation. It can be clearly seen that a shoulder seems to be present on the low retarding bias side. To investigate this effect, the signal height data series was measured again for a final electrode accumulation bias of 139.7 V, and extended with measurements being taken for biases of 130 V, 120 V, and 110 V also. These data, each containing more measurements than the data plotted in fig. 4.3.9, were then differentiated with respect to retarding bias as before, the results of which are shown in fig. 4.3.10.

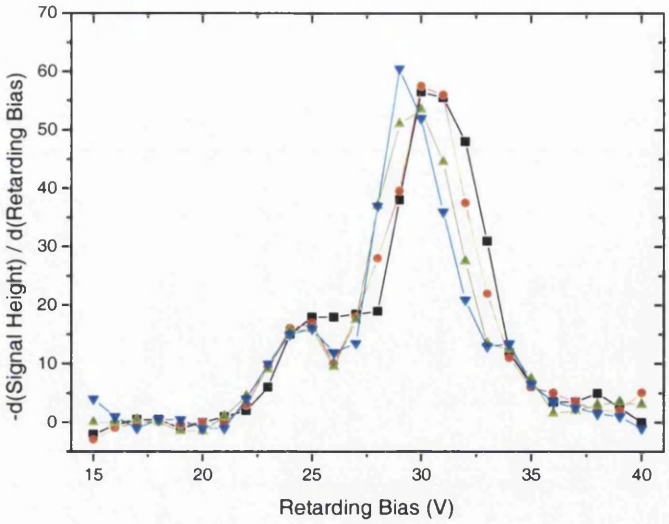

Figure 4.3.10: The energy spectra of the output pulse after 1 s accumulation, with varying bias on the final electrode: 139.7 V (blue), 130 V (green), 120 V (red), and 110 V (black). The connecting lines are included only to aid the eye.

It can be clearly seen that a second peak is present within these spectra, the magnitude and position of which remain relatively independent of the final electrode bias. This behaviour may be explained in part by the possibility of two distinct distributions of particles being present within the potential well at the moment of ejection, as suggested in fig. 4.3.7. When the final electrode bias is lowered to ground, the trapped positrons are acted upon by a simple potential gradient, and are able to escape from the accumulator. The two distributions would have distinct axial positions at this moment, and thus will have differing effective potentials. This may explain why we see two distinct energy peaks in fig. 4.3.10. Another explanation may be a non-ideal characteristic of the physical accumulator, such as field misalignment.

The peak shown in fig. 4.3.6 has FWHM resolution of approximately 100 ns, which is an order of magnitude larger than desired for use with the proposed 10 Hz pulsed laser spectroscopy experiments. Thus, an extra stage was added to the simple 'trap and dump' accumulation cycle, in an attempt to reduce the size of the potential

TABLE 4.3.3: THE REVISED BIASES PLACED ON THE ACCUMULATOR ELECTRODE ARRAY.

ELECTRODE	Front	Grad High	Grad Low	Big1	Big2	Big3	Big4	Big5
ACCUMULATION BIAS (V)	49	42	41	40	39	38	31	139.7
SQUEEZE BIAS (V)	109	102	101	100	99	98	80	139.7
DUMPING BIAS (V)	109	102	101	100	99	98	80	0

well even further, and thus also reduce the time width of the output positron pulse. The extra stage is highlighted in Table 4.3.3. The testing and optimisation of the biases used for the squeeze phase were conducted within a 100 ms accumulation cycle, 99 ms of which was the accumulation itself, with the squeeze phase held for 1 ms, before the particles were released. The result of the addition of this extra phase was to improve the resolution of the annihilation peak by a factor of 6, as shown in fig. 4.3.11. This resolution was perfectly acceptable for use in the 10 Hz laser spectroscopy measurements, especially since the time width of the laser pulses to be used had been under-estimated, and was measured to be closer to 20 ns.

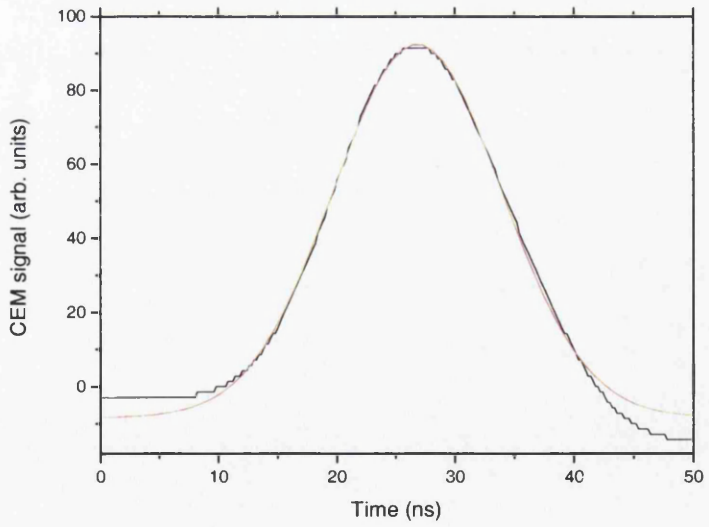

Figure 4.3.11: The timing spectra of the output pulse from the modified accumulation cycle (shown in black), fitted by a Gaussian distribution with FWHM = 16.73 ns (shown in red).

5.1 10 Hz pulsed positron source

As described in section 4.3, the two-stage positron accumulator could be operated at a range of frequencies, and a range of buffer gas pressures. The focus of that section was of the maximum output yield at varying buffer gas pressures, as shown in fig. 4.3.4. However, for the experiments in which a 10 Hz laser source would be used to irradiate positronium atoms, it was more important to focus on the output yield of the accumulator when it was run at 10 Hz. These data could be taken from that used in section 4.3, and subsequently compared with the output of an ideal accumulator. To calculate this ideal output, equations (4.3.1) and (4.3.3) must be combined to give

$$N(t) = \left(\frac{fI_0(1-\exp(-DP))}{BP} \right)(1-\exp(-t/\tau)), \qquad (5.1.1)$$

which reduces to

$$N(t) = \left(\frac{a}{P} \right)(1-\exp(-bP))(1-\exp(-tBP)), \qquad (5.1.2)$$

where a = 10.477 mbar, b = 4.42 x 10^5 mbar^{-1}, and B = 140881 mbar^{-1}s^{-1} as before. This expression could then be evaluated for the same buffer gas pressure range over which experimentation was conducted, and the two cases compared, as shown in fig.

5.1.1. It can be seen that the maximum output from the ideal accumulator is achieved at a buffer gas pressure of ~ 10^{-5} mbar, with the real accumulator only providing ~ 44 % of that yield at the same pressure. The low pressure limit for the ideal case described by equation (5.1.2) is proportional to P, whilst the corresponding equation for the non-ideal case, found by combining equations (4.3.1) and (4.3.6),

$$N(t) = \left(\frac{aE}{(EP+F)}\right)(1-\exp(-bP))(1-\exp(-tBP)), \qquad (5.1.3)$$

has a low pressure limit proportional to P^2, which explains the difference in output yields in this pressure range.

This is a far more positive result than that shown in fig. 4.3.2, and suggests that the loss of accumulated positrons within the device when it is operated at 10 Hz does not rule out the future experiments on the laser spectroscopy of positronium.

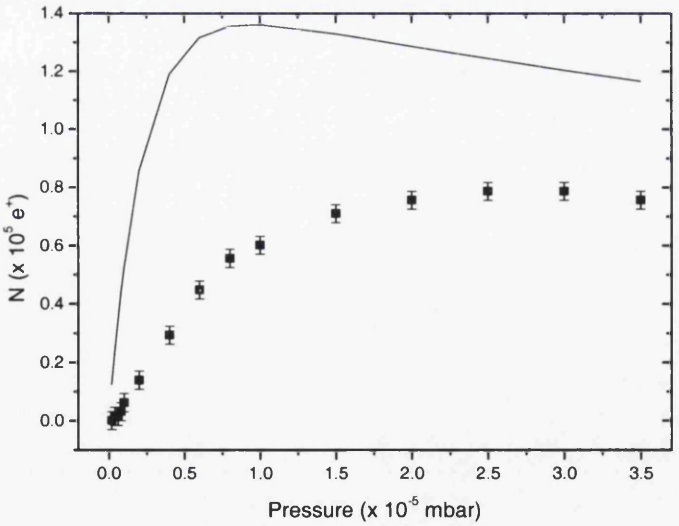

Figure 5.1.1: A comparison plot between the 10 Hz accumulator output yield (points), and that of an ideal accumulator (black line).

5.2 Positronium formation

To conduct experimentation to investigate the behaviour of positrons when they are incident on a number of differing target materials, additional apparatus had to be added to that shown in fig. 2.2.1, as detailed in fig. 5.2.1. The chosen target was mounted on a special actuator rod, such that its position could be adjusted in both x and y directions (where the z axis is set as that of the positron travel through the apparatus). This actuator device was mounted on the top flange of a specially fabricated cross piece, which had six window ports through which the laser beams would propagate during later experimentation. The plate onto which the target was fixed was able to be biased as desired. Images of the front and back of the target assembly are shown in fig. 5.2.2.

To test for the formation of positronium, a porous silica sample [Vallery *et al.* (2003)] was mounted on the target plate. The sample was then irradiated with low

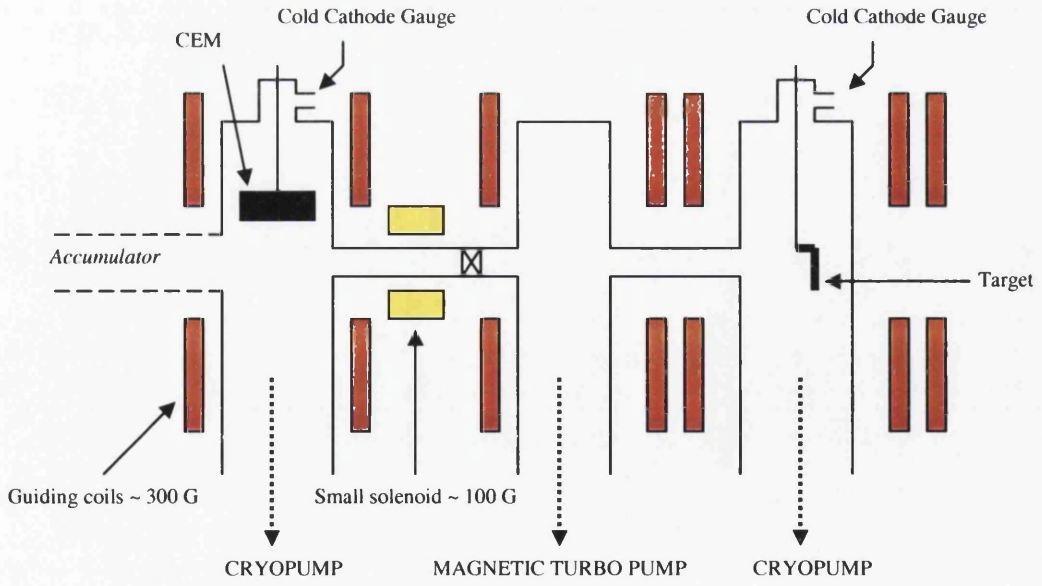

Figure 5.2.1: A schematic diagram of the second stage of the apparatus used at Swansea to investigate the behaviour of pulsed positrons incident on selected targets.

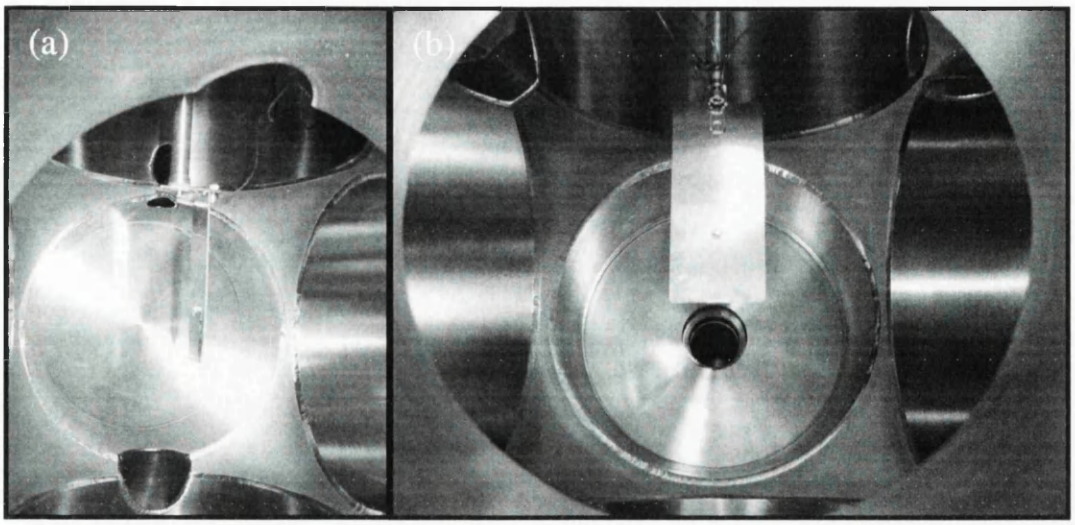

Figure 5.2.2: (a) an image of the front of the target assembly; and (b) an image of the back of the target assembly. The laser ports in the cross piece can be clearly seen in both images.

energy positrons, by grounding all of the accumulator electrodes, and moving the CEM detector out of the path of the particles. The target plate was biased at – 950 V, so that the effective positron implantation energy was ~ 1 keV. The gamma ray spectrum resulting from the annihilation events occurring was measured using a germanium crystal detector, whose output was processed by the Maestro software package, as in the case of the coincidence measurements. The spectrum was measured for five minutes of live time, and saved, after which the target was moved to a new position in the cross-piece by using the actuator device, and a new measurement run started. The resulting spectra were then inspected for signs of positronium formation [e.g. Canter *et al.* 1974], which would show itself by characteristic rearrangement of counts from the 511 keV photo-peak generated by the 2γ annihilation of individual positrons, to the channels making up the trough found at lower energies, because of the 3γ annihilation of ortho-positronium. The spectra measured when the target was in a position where the majority of the beam was incident upon the sample, and one where the majority of the beam was not, can be

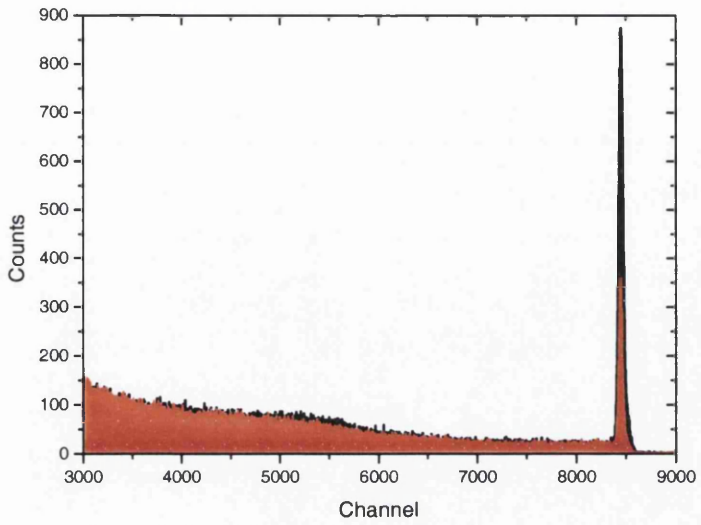

Figure 5.2.3: The gamma ray spectra resulting from 1 keV positron implantation into the porous silica target, which is positioned with few positrons incident upon it (shown in black), and with the majority of the beam incident upon it (shown in red).

seen in fig. 5.2.3. By summing the counts $C(i)$ within the trough found between channels i = 5300 and 8350, and dividing by the counts found within the photo-peak, a measure M can be made, to characterise the amount of positronium being formed, such that

$$M = \sum_{i=5300}^{i=8350} C(i) \Big/ \sum_{i=8351}^{i=8600} C(i), \qquad (5.2.1)$$

where it is assumed that M would be maximised when the target is positioned such that the greatest fraction of the positron beam is incident upon the sample. The quantity M was calculated for a number of target positions in the (x,y) plane, and a contour plot constructed to show the resulting change, as presented in fig. 5.2.4. It can clearly be seen that the maximum value of M does not correspond with the centre of the cross-piece, suggesting beam misalignment. This was particularly important,

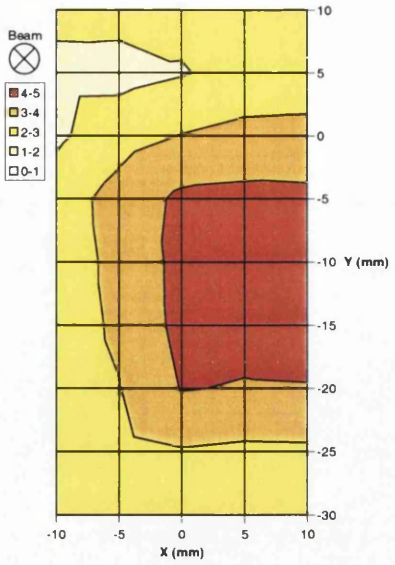

Figure 5.2.4: A contour plot to show the variation of *M* when the target is moved in the (x,y) plane, with light yellow denoting small values, through to red denoting high values. The centre of the cross-piece corresponds with the (0,0) co-ordinate.

for the future experiments planned required the laser irradiation admitted to the cross-piece to be incident with positronium atoms leaving the target surface. As described earlier, the cross-piece had been specially designed for this purpose, and could not be subsequently altered to allow realignment of the laser beams with respect to the positronium atoms. After exhaustive investigation of the apparatus, several stray magnetic fields were found to be drawing the positron particles off axis as they passed from the accumulator region through to the final cross-piece of the apparatus. This was quickly remedied, and the positrons were then found to stay on axis as required, allowing future experimentation with laser beams to remain feasible.

It should be noted that the characteristic re-arrangement of counts (i.e. between peak and trough) detailed above is not observed in the data presented in fig. 5.2.3, even though the contour plot shown in fig. 5.2.4 does give an accurate diagnostic of beam position. To further study this apparent contradiction, the ratio of the counts found in the photo-peak to the counts found in the whole measured

spectrum, at each measurement position, was calculated, as was the ratio of counts found in the trough to total counts. This data was processed as a contour plot, as shown in fig. 5.2.5. It can be seen that when the target was moved from the (-5, 5) co-ordinate to the (10, -10) co-ordinate, the photo-peak decreased in size by a factor of ~ 4.5, which was not matched by a similar increase in the number of counts found in the trough region. Indeed, the number of counts within the trough region actually decreased slightly. This raises doubts on whether positronium was indeed formed within this experiment, for the accurate mapping of the beam position seems to be made possible instead by the loss of 2γ annihilation events measured by the detector only. It is not likely that positronium is being formed, and transported away from the detection region before annihilation within the possible timescales.

A series of measurements were also made to ascertain the effect on the *M* parameter when the implantation energy of the positrons incident on the target, and

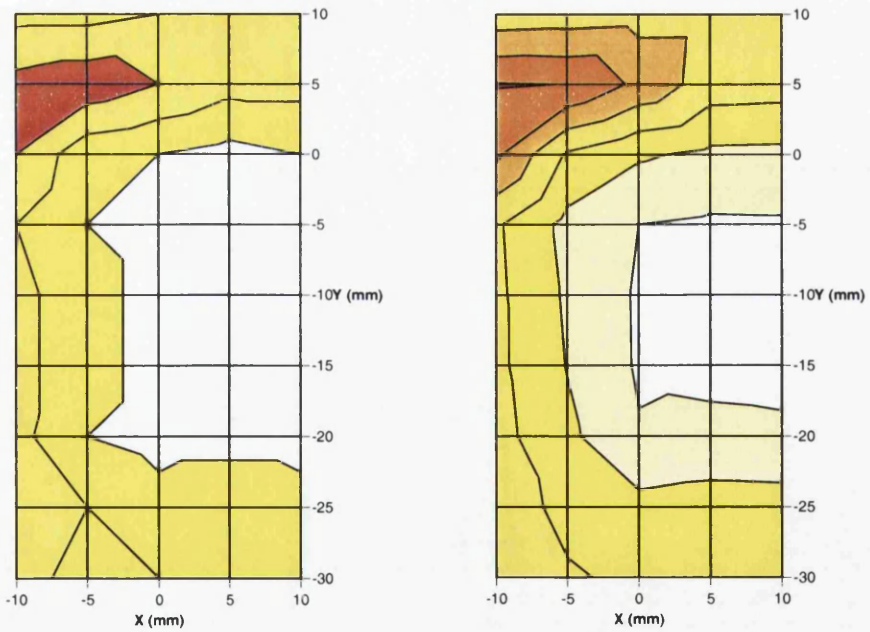

Figure 5.2.5: (left) a contour plot to show the variation of (trough counts / total counts) when the target is moved in the (x,y) plane, with white representing ~ 0.122 through to red representing ~ 0.134; (right) a contour plot to show the variation of (peak counts / total counts) when the target is moved in the (x,y) plane, with white representing ~ 0.02 through to red representing ~ 0.09.

on the bare stainless steel plate, was varied. This variation was accomplished by changing the bias on the target/plate itself. The positions of the target/plate assembly necessary for each case were found via fig. 5.2.4. The resulting output values for *M* in each case are presented in normalised form in fig. 5.2.6. It is clear to see that *M* increases when the implantation energy of the positrons into the target is increased. This is consistent with the positrons being implanted further into the dense silica bulk, and thus undergoing more interactions from which positronium may be formed. The resulting epithermal positronium may then be ejected into the pores, and cooled via interactions with the pore walls. In the case of stainless steel however, the *M* parameter is reduced with increased positron implantation energy. This is due to the diffusion length of a thermalised positron within the stainless steel being independent of the energy that the same positron was implanted with. The increase in implantation energy effectively increases the implantation depth of the positron into the material, which then has a constrained diffusion time within which to travel towards the sample surface, and possibly escape. Therefore, increasing the implantation depth of the positron will decrease the probability of it being able to

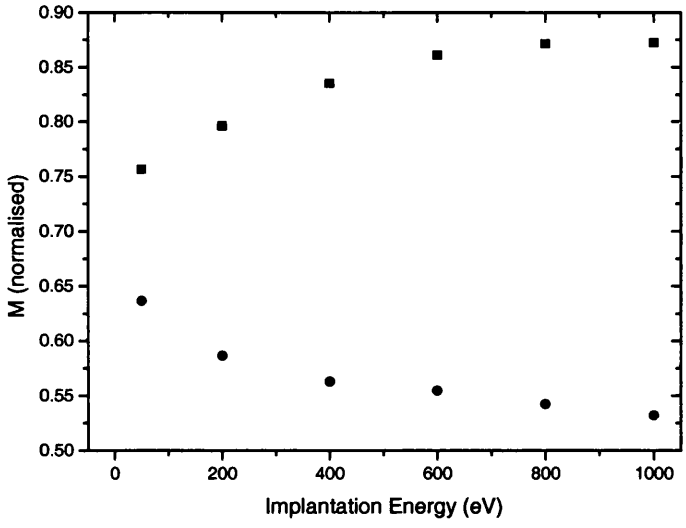

Figure 5.2.6: The change in parameter *M*, as described by equation (5.2.1), with varying implantation energy into the porous silica target (squares), and the stainless steel plate (circles).

diffuse to the surface of the sample and escape back into the vacuum. Those positrons which do escape may propagate away from the sample, and annihilate at a different point in the apparatus, which would subsequently not be measured by the detector. These 'lost' particles reduce the number of counts measured within the 511 keV photo-peak, generated by 2γ annihilation of positrons within the sample. Therefore, increasing the implantation energy of the positrons within the stainless steel, and consequently reducing the number of the particles able to diffuse back to the surface and escape, will increase the size of the denominator in equation (5.2.1), and thus decrease M, as seen in fig. 5.2.6.

5.3 Reverse Accumulation

The method of accumulating positrons described so far has relied on the particles entering the device through the high pressure region. This is strictly not necessary however, for the biases of the electrodes may be set up in a new geometry to allow accumulation of particles entering through the low pressure region of the device. This method would be useful in the diagnostics of the laser spectroscopy of positronium, where any positrons ionised from the bound state could be collected within the accumulator, and subsequently ejected for analysis. This idea was tested by replacing the silica target with a thin sheet of annealed tungsten. The choice of tungsten as a target was made due to its ability to moderate incident positrons and subsequently re-emit them, which would provide a source of particles able to enter the accumulator through the low pressure region.

The electrode biases used in an attempt to accumulate positrons entering the trap from the source end, to pulse them out towards the tungsten target and then re-

TABLE 5.3.1: THE ELECTRODE BIASES USED TO TRY AND RE-TRAP POSITRONS RE-EMITTED FROM THE TUNGSTEN FILM.

ELECTRODE	Front	Grad High	Grad Low	Big1	Big2	Big3	Big4	Big5
TRAP FORWARD BIAS (V)	49	42	41	40	39	38	31	139.7
SQUEEZE BIAS 1 (V)	109	102	101	100	99	98	91	139.7
DUMPING BIAS 1 (V)	109	42	41	40	39	38	31	0
TRAP BACKWARD BIAS (V)	109	42	41	40	39	38	31	45
SQUEEZE BIAS 2 (V)	109	102	101	100	99	98	91	139.7
DUMPING BIAS 2 (V)	109	102	101	100	99	98	91	0

accumulate those which are re-emitted back into the device, are given in Table 5.3.1. It should be noted that the potential distribution on axis for the backward accumulation phase is essentially the reverse of that of the forward accumulation phase. When this set-up was utilised, there was no second annihilation peak corresponding to the dump of backward trapped positrons measured by the CsI detector, which was positioned on the outer wall of the final cross-piece on the apparatus.

This may be understood when the time of flight of the positrons from the accumulator to the target, and then back to the accumulator, is considered. If the spiralling of the particles on the magnetic field lines is assumed to be negligible, then the time of flight for the particles of kinetic energy ~ 91 eV in their journey of ~ 0.6 m between the accumulator and the target when first pulsed out of the device may be calculated as ~ 100 ns. The time scale of the implantation of the particles in the tungsten target and their ensuing re-emission is of the order of ps. The particles which are re-emitted with kinetic energy ~ 50 eV will then take ~ 140 ns to propagate back to the accumulator. Those particles which pass through the accumulator to the restraining potential generated by the front electrode, brought to

rest, and repelled back out of the device without undergoing an interaction with a buffer gas molecule will take ~ 180 ns to do so. This therefore sets a limit of how slowly the last electrode in the device may be switched from + 139.7 to + 45 V, as shown in Table 5.3.1. If it takes longer than ~ 420 ns to accomplish this, then the positrons can simply escape from the accumulator and not be re-trapped. The drop time of the electrode between these two biases was found to be ~ 1.5 μs, far longer than that required. The pulser unit could not be used to reduce this time in this case, for it could only pulse between the load bias placed upon it, and 0 V, which made it unsuitable for use in the scheme described by Table 5.3.1.

An effort was made however to modify this scheme, to allow for the use of the pulsing unit, as shown in Table 5.3.2. The final electrode in the accumulator was pulsed up to + 45 V during the first particle dump phase, to be sure that a restraining field was present by the time the positrons returning from the tungsten target would be passing into the trap. There was no evidence that the positrons had been successfully retrapped however.

It was later found that significant modifications were required in the software and hardware which were being used to steer the electrode biases, in order for this

TABLE 5.3.2: THE MODIFIED ELECTRODE BIAS COMBINATION USED TO TRY AND RE-TRAP POSITRONS RE-EMITTED FROM THE TUNGSTEN FILM.

ELECTRODE	Front	Grad High	Grad Low	Big1	Big2	Big3	Big4	Big5
TRAP FORWARD BIAS (V)	49	42	41	40	39	32	100	0
SQUEEZE BIAS 1 (V)	109	102	101	100	99	92	130	0
DUMPING BIAS 1 (V)	109	49	48	48	47	47	46	45
TRAP BACKWARD BIAS (V)	100	42	41	40	39	32	46	45
SQUEEZE BIAS 2 (V)	135	102	101	100	99	92	105	45
DUMPING BIAS 2 (V)	100	42	41	40	39	32	0	0

form of retrapping procedure to be feasible. These modifications included the time step procedure that the LabVIEW electrode steering program used to allow for selection of time spans for each phase of the accumulation process. The unit of time step that had been used successfully in the accumulation experiments described in section 4.4.2 was 1 ms in length, which in this case immediately places a time delay of similar length between the first dumping phase, and the adjustment of the electrode biases for trapping in the backward direction. As has been shown, the positron time of flight between the accumulator and target is far shorter than this, and thus retrapping will be negligible. The unit time step could be reduced to ~ μs, but this then increased the number of time steps necessary for the accumulation phases, which resulted in computer memory usage problems. It is likely that a unit time step of ~ μs would still be too long, which requires the use of computer hardware with ~ ns timing capability, which was not immediately available. With a combination of additional pulser units, software development, and hardware with ~ ns timing capability, this form of trapping procedure would be feasible, but within the scope of the experiment at the time, it was not achievable.

A measure of the re-emission probability of a positron incident on the tungsten surface was, however, achievable. An estimate could be found by comparing the annihilation signals measured when beam positrons accumulated in the forward direction, and the backward direction, were pulsed onto the tungsten target, as shown in fig. 5.3.1. It should be noted that this scheme is not the desired reverse accumulation described earlier, where positrons accumulated in the forward direction would be pulsed out, and those subsequently emitted back towards the device re-accumulated. In the forward loading case, the number of accumulated positrons N_f pulsed into the tungsten target must equal the sum of the number of

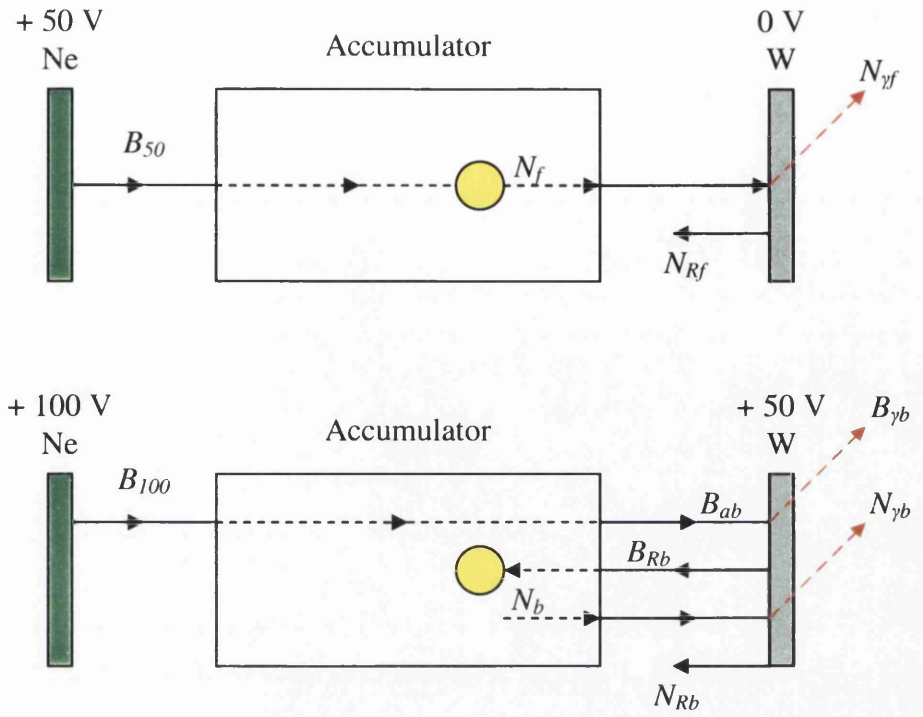

Figure 5.3.1: A schematic diagram showing accumulation of positrons in the forward direction (top), and the backward direction (bottom).

positrons $N_{\gamma f}$ which annihilate within the target, and the number of positrons N_{Rf} which are re-emitted from the target, in other words

$$N_f = N_{Rf} + N_{\gamma f}. \qquad (5.3.1)$$

If we denote the re-emission probability of a positron implanted into the target as α, then it follows that the number of positrons re-emitted from the target when the positrons are pulsed onto it is simply αN_f, and thus

$$N_{\gamma f} = N_f(1-\alpha). \qquad (5.3.2)$$

In the backward loading case, the positron beam of kinetic energy > 100 eV is able to pass through the accumulator set up to accumulate 50 eV particles, and be

incident on the target. The attenuation of the particles as they pass through the buffer gas has been considered, such that the beam flux exiting the accumulator, B_{ab}, is less than or equal to the beam flux entering the accumulator, B_{100} (see fig. 5.3.1). The re-emitted positrons from the target thus form a beam of kinetic energy ~ 50 eV, and of intensity B_{Rb}, which is equivalent to αB_{ab}. These particles propagate into the accumulator region, and are subsequently trapped. Those which are successfully accumulated, N_b, are then pulsed back towards the target, where $N_{\gamma b}$ annihilate within the target, and N_{Rb} are re-emitted, such that

$$N_b = N_{Rb} + N_{\gamma b}, \tag{5.3.3}$$

which can be simplified by using similar logic to that for the forward loading case to

$$N_{\gamma b} = N_b(1-\alpha). \tag{5.3.4}$$

This simplification contains the assumption that the positrons in the backward case are incident on the target with the same energy as those in the forward case. If we assume that B_{50} is approximately equal to B_{ab}, then it follows that the beam loading the accumulator in the backward case is approximated by αB_{50}. Thus, if we assume comparative trapping efficiencies within the accumulator in both cases, we may say that $N_b \approx \alpha N_f$. Therefore, α may be calculated from the number of gamma counts measured in each case

$$\frac{\varepsilon N_{\gamma b}}{\varepsilon N_{\gamma f}} = \frac{\alpha N_f(1-\alpha)}{N_f(1-\alpha)} = \alpha, \tag{5.3.5}$$

TABLE 5.3.3: THE ELECTRODE BIASES USED FOR THE FORWARD LOADING CASE.

ELECTRODE	Front	Grad High	Grad Low	Big1	Big2	Big3	Big4	Big5
ACCUMULATION BIAS (V)	49	42	41	40	39	38	31	105
SQUEEZE BIAS (V)	109	102	101	100	99	98	91	105
DUMPING BIAS (V)	109	102	101	100	99	98	91	0

TABLE 5.3.4: THE ELECTRODE BIASES USED FOR THE BACKWARD LOADING CASE.

ELECTRODE	Front	Grad High	Grad Low	Big1	Big2	Big3	Big4	Big5
ACCUMULATION BIAS (V)	49	42	41	40	39	38	31	45
SQUEEZE BIAS (V)	109	102	101	100	99	98	91	105
DUMPING BIAS (V)	109	102	101	100	99	98	91	0

where ε is the efficiency of the detector, which does not need to be considered assuming the same measurement conditions are present in the two cases.

The electrode biases used in each case are presented in Tables 5.3.3 and 5.3.4, with the final electrode not being pulsed in both cases, and the squeeze and dump phases being spaced in time by 1 ms. The buffer gas pressure in both cases was 3×10^{-6} mbar. A number of accumulation times for both cases were considered. The results for α are presented in fig. 5.3.2, which gives an overall estimate for the

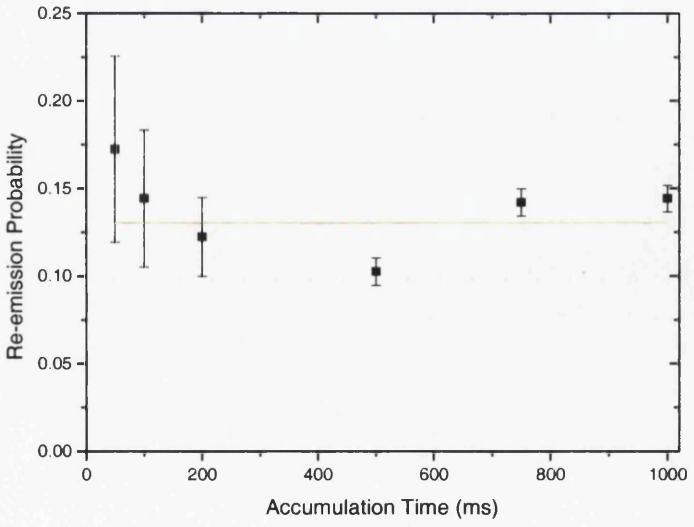

Figure 5.3.2: The output values of the re-emission probability α for varying accumulation times. A weighted average of this data gives 0.130 (± 0.004), as shown by the red line.

re- emission probability as 0.130 (± 0.004).

An alternative method of calculating α that does not entail the accumulation of positrons entering the device through the low pressure region is presented in fig. 5.3.3. The device was operated in the conventional sense, with the electrode biases being described by Table 4.3.3, at a buffer gas pressure of 3 x 10^{-6} mbar. The final accumulator electrode in this case was pulsed. The positrons accumulated were pulsed onto the + 50 V biased target, and the fraction α that were re-emitted back towards the device were subsequently repelled back towards the target by the + 80 V bias that was held on the penultimate electrode. As such, these positrons were incident on the target once more, and a fraction α of these particles was re-emitted. If the number of positrons incident on the target initially is denoted by N, then it follows that the number of annihilations from the first interaction of the particles with the target, N_1, is described by

$$N_1 = N(1-\alpha), \qquad (5.3.6)$$

with the number of re-emitted particles being αN. If it assumed that none of these re-emitted particles are lost during their transit to and from the accumulator, then αN

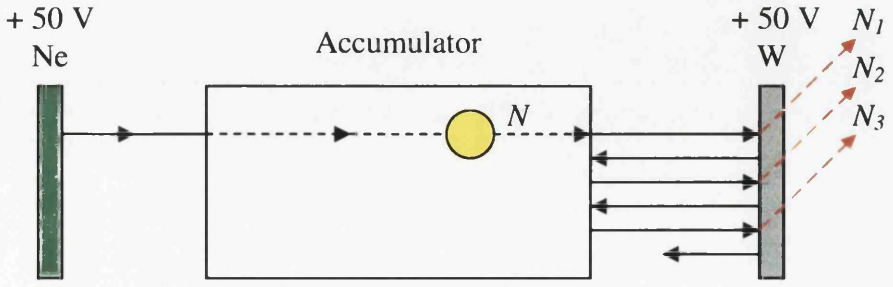

Figure 5.3.3: A schematic diagram showing an alternative method of calculating the re-emission probability α.

positrons are subsequently incident on the target. The number of annihilations from this interaction, N_2, is therefore described by

$$N_2 = \alpha N(1-\alpha). \qquad (5.3.7)$$

Thus, α may be found from N_2/N_1. If the number of annihilations occurring when the remaining positrons encounter the target for the third time, N_3, is considered, then it also follows that

$$\frac{N_3}{N_2} = \frac{\alpha^2 N(1-\alpha)}{\alpha N(1-\alpha)} = \alpha. \qquad (5.3.8)$$

Once again, if it assumed that the detection efficiency of the annihilation photons is the same in each measurement, then it factors out, and need not be considered. To achieve ~ ns resolution in these measurements, a plastic scintillation crystal was used, mounted on a long light guide of length 0.7 m. The annihilation peaks measured resulting from differing accumulation times are shown in fig. 5.3.4.

It is clear that there are three distinct peaks in each case, spaced in time by ~ 220 ns, which is comparable with the ~ 2 x 140 ns calculated earlier. From this data, the mean value for N_2/N_1 is 0.265, with standard deviation 0.042, while the mean value for N_3/N_2 is 0.323, with standard deviation 0.047. This is a factor of two larger than the estimate calculated from equation (5.3.5), which assumes in its derivation that B_{Rb} is equal to αB_{50}. This assumption presumes that the same beam intensity exists at the entrance to the high pressure region of the accumulator when

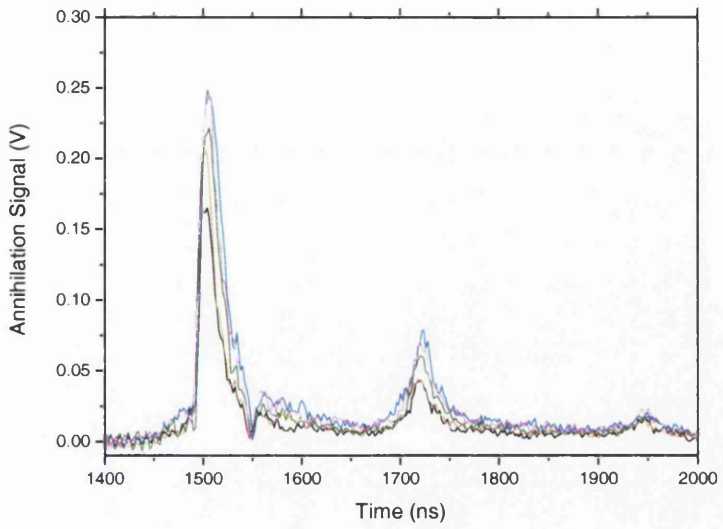

Figure 5.3.4: The annihilation peaks resulting from accumulated positrons undergoing multiple interactions with a tungsten target. The accumulation times used were 2 seconds (black), 3 seconds (red), 4 seconds (green), 5 seconds (blue) and 10 seconds (magenta).

the neon moderator is biased at + 50 V, and at the exit of the accumulator when the moderator is biased at + 100 V. This could easily not be the case, which means that more trust should be placed in the second method of calculating α. Within this method, the N_2/N_1 calculation contains less uncertainty than that of the N_3/N_2 calculation, and as such, the estimate of α = 0.265 seems likely to be the most reliable.

This method was repeated, but now for varying positron energy with a fixed accumulation time of 1 second. The implantation energy of the particles was varied by changing the amount that the electrode biases were lifted by during the squeeze phase, as described in Table 4.3.3. The annihilation signals was recorded for a number of dump energies between 61 and 131 eV, with those for the two extreme cases shown in fig. 5.3.5. If we assume that the energy of the re-emitted positrons is independent of the energy with which they arrive, then the ~ 42 ns spacing in time between the first annihilation peaks from each case shown must be due to the difference in time of flight of the particles in their initial transit from the accumulator

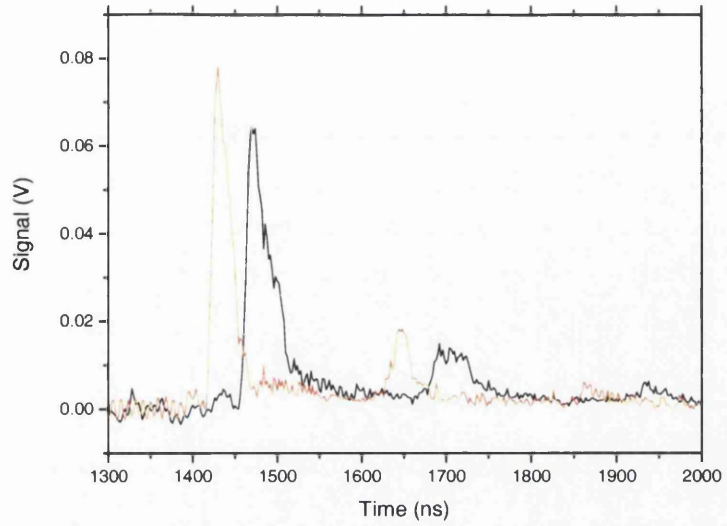

Figure 5.3.5: The annihilation peaks resulting from accumulated positrons undergoing multiple interactions with a tungsten target, with initial implantation energy of ~ 11 eV (shown in black), and ~ 81 eV (shown in red).

to the target. This is confirmed when the times of flight are calculated, the 61 eV particles being found to take ~ 130 ns to complete the journey, whilst the 131 eV particles will take ~ 88 ns. The mean value for N_2/N_1 across the implantation energies is 0.274, with standard deviation 0.040, with the mean value for N_3/N_2 being 0.355, with standard deviation 0.059.

These estimates for α are in line with the general assumption made by Frieze *et al.* (1985) that the probability of positron emission from such a surface would be in the range 20 – 30 %, though it was there assumed that the incident energy was of the order of keV.

The field of positron physics has greatly expanded in the space of a few decades, and this acceleration in research has been fuelled by advances in positron generation and manipulation within a laboratory environment. In its 75 years lifetime, the role of the positron has developed from a brave theoretical postulate, to a unique, irreplaceable tool within cutting-edge scientific research and technology. At the dawn of the twenty-first century, the positron is playing diverse roles, in complex scientific experimentation such as the first production of low energy anti-atoms [Amoretti *et al.* (2002); Gabrielse *et al.* (2002)], as well as being a vital medical tool in positron emission tomography [Nutt (2002)]. With the possible further development of positron devices as commercial products for the industrial sector [Coleman (2002)], the importance of the particle seems set to increase even further.

It has been presented here how a powerful new positron device has been constructed and tested at the University of Wales, Swansea, using now standard principles within a modest timescale. At the time of writing, it stands as the most potent positron beam line within the U.K., and one of few worldwide with the capability of accumulating large numbers of the particle.

These achievements are founded on the mechanisms described within section 2.1, from which high energy β^+ particles emitted from a ^{22}Na radioactive source may be slowed to form a beam of low energy positrons, with physical properties as reported in section 2.3.2. An interesting observation of fluctuations in the positron beam yield during the adsorption of neon atoms onto the cold conical copper assembly was presented in section 2.3.1. This phenomenon does not seem to have

been reported by any other group in the field, yet was reproducible enough not to be discounted as a unique quirk of this apparatus. A number of limited studies of this phenomenon were made, though no firm explanation of its origin was achieved. The work was presented however in the possibility that it may prove a useful reference for future workers in the development of positron moderation.

The application of bunching devices to slow positron beams was described in chapter 3, with specific reference to the apparatus tested at the University of Aarhus, Denmark. The effects of non-ideal characteristics of this apparatus were presented, and the possible use of these to improve the output timing resolution of such a device put forward. This future work could implement into the design stage of such a device the possibility of varying the propagation time of the bias pulse down the electrode chain, the rise times of the electrodes, and the variation in electrode bias down the chain. This would allow for precise fine tuning of the device, for example the bunching focus point, for the specific needs of experimentation. With the increasing use of focussed positron pulses, these practical improvements may be of great benefit for future bunching equipment.

The trapping and accumulation of low energy positrons within a modified Penning-Malmberg device was described within chapter 4, with specific details of the development of a two-stage system, instead of the usual three-stage scheme. It was shown that by careful study of the properties of the pulse of particles output from such an accumulator, internal processes within the device performance may be characterised, and simple descriptions of particle behaviour within the potential well may be offered. With the expected commercialisation of compact positron beam apparatus, the diagnostic tools here presented may be of use for future workers developing compact accumulation devices. A divergence from linearity was seen in

fig. 4.3.3 at higher buffer gas pressures, which suggested that the positrons had longer lifetimes within this regime than expected. This divergence has not been refuted by subsequent experimentation, which also tested for a non-linear relationship between the pressure measured at the gauge to that existing within the device itself. It may be possible that field misalignment is in some way generating the departure from linearity seen in fig. 4.3.3, though this is nothing more than a suggestion.

Finally, a number of simple applications of a low energy positron beam-line with accumulation capabilities were presented. The ability of the Swansea apparatus to serve as a 10 Hz source of positrons will be put to use in future experiments probing the Rydberg states of positronium using laser systems. The likely scheme of the formation of this positronium was also presented, and its use in the diagnosis of a beam misalignment in the latter stages of the apparatus shown. Also, a simple experiment to measure the re-emission probability of low energy positrons incident on an annealed tungsten target was reported.

The scope of this thesis has covered the construction, testing, and application of the low energy positron beam-line at Swansea, which now stands ready for use as a user-friendly front-end apparatus in many possible cutting-edge research experiments. The author hopes that this will indeed be the case, and that the reader has gleaned useful knowledge concerning the field of positron physics in general.

Appendices

The simulation of a physical device using the SIMION software package began with the writing of a geometry file, to define the electrode structure of the apparatus. The geometry file used for the simulation of the buncher device used at the University of Aarhus was as follows:

```
PA_Define(1400,60,1,C,Y,E,40)                ; defining the Potential Array characteristics.
e(0){Fill{within{Box(2,58,1156,60)}}}        ; defining the grounded regions neighbouring
e(0){Fill{within{Box(0,25,2,60)}}}           ; the device.
e(0){Fill{within{Box(1157,10,1159,60)}}}
locate(100){e(1){include(Elec.gem)}}         ; defining the adjustable electrodes all of
locate(121){e(2){include(Elec.gem)}}         ; physical size characterised by the Elec.gem
locate(142){e(3){include(Elec.gem)}}         ; blueprint. The e(...) command here is taken by
locate(163){e(4){include(Elec.gem)}}         ; SIMION to designate a number to that
locate(184){e(5){include(Elec.gem)}}         ; electrode, which will be used within the user
locate(205){e(6){include(Elec.gem)}}         ; program to define the unique potential on each
locate(226){e(7){include(Elec.gem)}}         ; of the adjustable electrodes at every time step.
locate(247){e(8){include(Elec.gem)}}
locate(268){e(9){include(Elec.gem)}}
locate(289){e(10){include(Elec.gem)}}
locate(310){e(11){include(Elec.gem)}}
locate(331){e(12){include(Elec.gem)}}
locate(352){e(13){include(Elec.gem)}}
locate(373){e(14){include(Elec.gem)}}
locate(394){e(15){include(Elec.gem)}}
locate(415){e(16){include(Elec.gem)}}
locate(436){e(17){include(Elec.gem)}}
locate(457){e(18){include(Elec.gem)}}
```

```
locate(478){e(19){include(Elec.gem)}}
locate(499){e(20){include(Elec.gem)}}
locate(520){e(21){include(Elec.gem)}}
locate(541){e(22){include(Elec.gem)}}
locate(562){e(23){include(Elec.gem)}}
locate(583){e(24){include(Elec.gem)}}
locate(604){e(25){include(Elec.gem)}}
locate(625){e(26){include(Elec.gem)}}
locate(646){e(27){include(Elec.gem)}}
locate(667){e(28){include(Elec.gem)}}
locate(688){e(29){include(Elec.gem)}}
locate(709){e(30){include(Elec.gem)}}
locate(730){e(130.83){include(Elec.gem)}}      ; here the e(...) command will be taken by
locate(751){e(115.88){include(Elec.gem)}}      ; SIMION as the potential to be put upon these
locate(772){e(101.85){include(Elec.gem)}}      ; static electrodes.
locate(793){e(88.73){include(Elec.gem)}}
locate(814){e(76.50){include(Elec.gem)}}
locate(835){e(65.18){include(Elec.gem)}}
locate(856){e(54.78){include(Elec.gem)}}
locate(877){e(45.27){include(Elec.gem)}}
locate(898){e(36.68){include(Elec.gem)}}
locate(919){e(28.97){include(Elec.gem)}}
locate(940){e(22.18){include(Elec.gem)}}
locate(961){e(16.30){include(Elec.gem)}}
locate(982){e(11.32){include(Elec.gem)}}
locate(1003){e(7.25){include(Elec.gem)}}
locate(1024){e(4.07){include(Elec.gem)}}
locate(1045){e(1.82){include(Elec.gem)}}
locate(1066){e(0.45){include(Elec.gem)}}
locate(1087){e(0){include(Elec.gem)}}
```

```
locate(1160){e(-33.3){Include(Elecs.gem)}}      ; the acceleration stage located after the
locate(1163){e(-66.6){Include(Elecs.gem)}}      ; bunching region within the Aarhus apparatus.
locate(1166){e(-100){Include(Elecs.gem)}}       ; This stage is made up of an array of electrodes
locate(1169){e(-133.3){Include(Elecs.gem)}}     ; following the Elecs.gem blueprint.
locate(1172){e(-166.6){Include(Elecs.gem)}}
locate(1175){e(-200){Include(Elecs.gem)}}
locate(1178){e(-233.3){Include(Elecs.gem)}}
locate(1181){e(-266.6){Include(Elecs.gem)}}
locate(1184){e(-300){Include(Elecs.gem)}}
locate(1187){e(-333.3){Include(Elecs.gem)}}
locate(1190){e(-366.6){Include(Elecs.gem)}}
locate(1193){e(-400){Include(Elecs.gem)}}
locate(1196){e(-433.3){Include(Elecs.gem)}}
locate(1199){e(-466.6){Include(Elecs.gem)}}
locate(1202){e(-500){Include(Elecs.gem)}}
locate(1205){e(-533.3){Include(Elecs.gem)}}
locate(1208){e(-566.6){Include(Elecs.gem)}}
locate(1211){e(-600){Include(Elecs.gem)}}
locate(1214){e(-633.3){Include(Elecs.gem)}}
locate(1217){e(-666.6){Include(Elecs.gem)}}
locate(1220){e(-700){Include(Elecs.gem)}}
locate(1223){e(-733.3){Include(Elecs.gem)}}
locate(1226){e(-766.6){Include(Elecs.gem)}}
locate(1229){e(-800){Include(Elecs.gem)}}
locate(1232){e(-833.3){Include(Elecs.gem)}}
locate(1235){e(-866.6){Include(Elecs.gem)}}
locate(1238){e(-900){Include(Elecs.gem)}}
locate(1241){e(-933.3){Include(Elecs.gem)}}
locate(1244){e(-966.6){Include(Elecs.gem)}}
```

```
locate(1247){e(-1000){Include(Elecs.gem)}}
locate(1250){e(-1033.3){Include(Elecs.gem)}}
locate(1253){e(-1066.6){Include(Elecs.gem)}}
e(-1100){Fill{within{Box(1255,10,1257,40)}}}      ; the end stage of the Aarhus apparatus as
e(-1100){Fill{within{Box(1257,38,1358,40)}}}      ; simulated.
e(-1100){Fill{within{Box(1358,0,1360,40)}}}
```

The Elec.gem file consisted of the program instruction: `Fill{within{Box(0,27,20,25)}}`

The Elecs.gem file consisted of the program instruction: `Fill{within {Box(0,10,2,12)}}`

The program file for the buncher simulations in general took the form as shown below. The programming was deliberately made quite "long-hand", to aid the user when modifications to the simulation procedure needed to be made, and to allow for easy monitoring of the calculation procedures used.

```
defa rise_time 0                    ; initialising the rise_time parameter
defa propagation_time 10e-3         ; initialising the propagation_time parameter
defa POW 2                          ; initialising the exponent parameter
defa rantime 0                      ; initialising the rantime parameter
defa temptime 0                     ; initialising the temptime parameter
defa Xlow  150                      ; initialising the lowest X position considered
defa Xhigh 680                      ; initialising the highest X position considered
defa Ylow  0                        ; initialising the lowest Y position considered
defa Yhigh 0                        ; initialising the highest Y position considered
defa templow  0                     ; initialising the templow parameter
defa temphigh 0                     ; initialising the temphigh parameter
defa temppos  0                     ; initialising the temppos parameter
defa N 1000                         ; initialising the number of particles considered
defa voltin   0                     ; initialising the voltin parameter
```

```
defa voltout  0                          ; initialising the voltout  parameter
defa PT     0                            ; initialising the PT parameter
defs no_electrodes 47                    ; initialising the number of electrodes
defs Max_Volt 1000                       ; initialising the maximum bunching potential
defa V1  0  defa V2  0  defa V3  0  defa V4  0  defa V5  0        ; initialising the parameters
defa V6  0  defa V7  0  defa V8  0  defa V9  0  defa V10 0        ; that will be used to define
defa V11 0  defa V12 0  defa V13 0  defa V14 0  defa V15 0        ; the electrode biases
defa V16 0  defa V17 0  defa V18 0  defa V19 0  defa V20 0
defa V21 0  defa V22 0  defa V23 0  defa V24 0  defa V25 0
defa V26 0  defa V27 0  defa V28 0  defa V29 0  defa V30 0
defa P1  0  defa P2  0  defa P3  0  defa P4  0  defa P5  0        ; initialising the parameters
defa P6  0  defa P7  0  defa P8  0  defa P9  0  defa P10 0        ; that will be used to define
defa P11 0  defa P12 0  defa P13 0  defa P14 0  defa P15 0        ; the delay time before each
defa P16 0  defa P17 0  defa P18 0  defa P19 0  defa P20 0        ; electrode bias is initiated
defa P21 0  defa P22 0  defa P23 0  defa P24 0  defa P25 0
defa P26 0  defa P27 0  defa P28 0  defa P29 0  defa P30 0
defa R1  0  defa R2  0  defa R3  0  defa R4  0  defa R5  0        ; initialising the parameters
defa R6  0  defa R7  0  defa R8  0  defa R9  0  defa R10 0        ; that will be used to define
defa R11 0  defa R12 0  defa R13 0  defa R14 0  defa R15 0        ; the rise times of the
defa R16 0  defa R17 0  defa R18 0  defa R19 0  defa R20 0        ; electrodes
defa R21 0  defa R22 0  defa R23 0  defa R24 0  defa R25 0
defa R26 0  defa R27 0  defa R28 0  defa R29 0  defa R30 0


seg Initialize
47 LN rcl POW * E^X 1/X 1000 * sto temp1     ; the calculation of the bias for
47 LN rcl POW * E^X rcl temp1 * sto V1       ; each electrode using the
46 LN rcl POW * E^X rcl temp1 * sto V2       ; exponent defined earlier
45 LN rcl POW * E^X rcl temp1 * sto V3
44 LN rcl POW * E^X rcl temp1 * sto V4
43 LN rcl POW * E^X rcl temp1 * sto V5
```

```
42 LN rcl POW * E^X rcl temp1 * sto V6
41 LN rcl POW * E^X rcl temp1 * sto V7
40 LN rcl POW * E^X rcl temp1 * sto V8
39 LN rcl POW * E^X rcl temp1 * sto V9
38 LN rcl POW * E^X rcl temp1 * sto V10
37 LN rcl POW * E^X rcl temp1 * sto V11
36 LN rcl POW * E^X rcl temp1 * sto V12
35 LN rcl POW * E^X rcl temp1 * sto V13
34 LN rcl POW * E^X rcl temp1 * sto V14
33 LN rcl POW * E^X rcl temp1 * sto V15
32 LN rcl POW * E^X rcl temp1 * sto V16
31 LN rcl POW * E^X rcl temp1 * sto V17
30 LN rcl POW * E^X rcl temp1 * sto V18
29 LN rcl POW * E^X rcl temp1 * sto V19
28 LN rcl POW * E^X rcl temp1 * sto V20
27 LN rcl POW * E^X rcl temp1 * sto V21
26 LN rcl POW * E^X rcl temp1 * sto V22
25 LN rcl POW * E^X rcl temp1 * sto V23
24 LN rcl POW * E^X rcl temp1 * sto V24
23 LN rcl POW * E^X rcl temp1 * sto V25
22 LN rcl POW * E^X rcl temp1 * sto V26
21 LN rcl POW * E^X rcl temp1 * sto V27
20 LN rcl POW * E^X rcl temp1 * sto V28
19 LN rcl POW * E^X rcl temp1 * sto V29
18 LN rcl POW * E^X rcl temp1 * sto V30

rcl propagation_time 29 / sto temp2          ; calculating the delay times
rcl temp2 0  * sto P1   rcl temp2 1  * sto P2
rcl temp2 2  * sto P3   rcl temp2 3  * sto P4
rcl temp2 4  * sto P5   rcl temp2 5  * sto P6
```

```
rcl temp2 6  * sto P7   rcl temp2 7  * sto P8
rcl temp2 8  * sto P9   rcl temp2 9  * sto P10
rcl temp2 10 * sto P11  rcl temp2 11 * sto P12
rcl temp2 12 * sto P13  rcl temp2 13 * sto P14
rcl temp2 14 * sto P15  rcl temp2 15 * sto P16
rcl temp2 16 * sto P17  rcl temp2 17 * sto P18
rcl temp2 18 * sto P19  rcl temp2 19 * sto P20
rcl temp2 20 * sto P21  rcl temp2 21 * sto P22
rcl temp2 22 * sto P23  rcl temp2 23 * sto P24
rcl temp2 24 * sto P25  rcl temp2 25 * sto P26
rcl temp2 26 * sto P27  rcl temp2 27 * sto P28
rcl temp2 28 * sto P29  rcl temp2 29 * sto P30


30e-3 sto R1                                ; calculating the rise times
rcl R1 0.63e-3 - sto R2
rcl R2 0.63e-3 - sto R3
rcl R3 0.63e-3 - sto R4
rcl R4 0.63e-3 - sto R5
rcl R5 0.63e-3 - sto R6
rcl R6 0.63e-3 - sto R7
rcl R7 0.63e-3 - sto R8
rcl R8 0.63e-3 - sto R9
rcl R9 0.63e-3 - sto R10
rcl R10 0.63e-3 - sto R11
rcl R11 0.63e-3 - sto R12
rcl R12 0.63e-3 - sto R13
rcl R13 0.63e-3 - sto R14
rcl R14 0.63e-3 - sto R15
rcl R15 0.63e-3 - sto R16
rcl R16 0.63e-3 - sto R17
```

```
rcl R17 0.63e-3 - sto R18
rcl R18 0.63e-3 - sto R19
rcl R19 0.63e-3 - sto R20
rcl R20 0.63e-3 - sto R21
rcl R21 0.63e-3 - sto R22
rcl R22 0.63e-3 - sto R23
rcl R23 0.63e-3 - sto R24
rcl R24 0.63e-3 - sto R25
rcl R25 0.63e-3 - sto R26
rcl R26 0.63e-3 - sto R27
rcl R27 0.63e-3 - sto R28
rcl R28 0.63e-3 - sto R29
rcl R29 0.63e-3 - sto R30

rcl Xlow sto templow rcl Xhigh sto temphigh gsb randpos rcl tempos        ; calculating the
sto Ion_Px_mm                                                            ; starting position
rcl Ylow sto templow rcl Yhigh sto temphigh gsb randpos rcl temppos       ; for the initialised
sto Ion_Py_mm                                                            ; ion

lbl randpos                          ; the calculation of the starting position for the
rcl temphigh rcl templow - rcl Ion_Number *   ; initialised ion. Here, the ions are incremented
rcl N /                              ; between the lower and upper limits as
rcl templow +                        ; appropriate
sto temppos
rtn

seg Tstep_Adjust                     ; defining the time step used by SIMION at 50
5e-5 sto Ion_Time_Step               ; ps
```

```
seg Fast_Adjust                          ; adjusting the electrode biases for each time
                                         ; step
rcl P1  sto PT rcl V1  sto voltin rcl R1 sto rise_time gsb Calc rcl voltout sto Adj_Elect01
rcl P2  sto PT rcl V2  sto voltin rcl R2 sto rise_time gsb Calc rcl voltout sto Adj_Elect02
rcl P3  sto PT rcl V3  sto voltin rcl R3 sto rise_time gsb Calc rcl voltout sto Adj_Elect03
rcl P4  sto PT rcl V4  sto voltin rcl R4 sto rise_time gsb Calc rcl voltout sto Adj_Elect04
rcl P5  sto PT rcl V5  sto voltin rcl R5 sto rise_time gsb Calc rcl voltout sto Adj_Elect05
rcl P6  sto PT rcl V6  sto voltin rcl R6 sto rise_time gsb Calc rcl voltout sto Adj_Elect06
rcl P7  sto PT rcl V7  sto voltin rcl R7 sto rise_time gsb Calc rcl voltout sto Adj_Elect07
rcl P8  sto PT rcl V8  sto voltin rcl R8 sto rise_time gsb Calc rcl voltout sto Adj_Elect08
rcl P9  sto PT rcl V9  sto voltin rcl R9 sto rise_time gsb Calc rcl voltout sto Adj_Elect09
rcl P10 sto PT rcl V10 sto voltin rcl R10 sto rise_time gsb Calc rcl voltout sto Adj_Elect10
rcl P11 sto PT rcl V11 sto voltin rcl R11 sto rise_time gsb Calc rcl voltout sto Adj_Elect11
rcl P12 sto PT rcl V12 sto voltin rcl R12 sto rise_time gsb Calc rcl voltout sto Adj_Elect12
rcl P13 sto PT rcl V13 sto voltin rcl R13 sto rise_time gsb Calc rcl voltout sto Adj_Elect13
rcl P14 sto PT rcl V14 sto voltin rcl R14 sto rise_time gsb Calc rcl voltout sto Adj_Elect14
rcl P15 sto PT rcl V15 sto voltin rcl R15 sto rise_time gsb Calc rcl voltout sto Adj_Elect15
rcl P16 sto PT rcl V16 sto voltin rcl R16 sto rise_time gsb Calc rcl voltout sto Adj_Elect16
rcl P17 sto PT rcl V17 sto voltin rcl R17 sto rise_time gsb Calc rcl voltout sto Adj_Elect17
rcl P18 sto PT rcl V18 sto voltin rcl R18 sto rise_time gsb Calc rcl voltout sto Adj_Elect18
rcl P19 sto PT rcl V19 sto voltin rcl R19 sto rise_time gsb Calc rcl voltout sto Adj_Elect19
rcl P20 sto PT rcl V20 sto voltin rcl R20 sto rise_time gsb Calc rcl voltout sto Adj_Elect20
rcl P21 sto PT rcl V21 sto voltin rcl R21 sto rise_time gsb Calc rcl voltout sto Adj_Elect21
rcl P22 sto PT rcl V22 sto voltin rcl R22 sto rise_time gsb Calc rcl voltout sto Adj_Elect22
rcl P23 sto PT rcl V23 sto voltin rcl R23 sto rise_time gsb Calc rcl voltout sto Adj_Elect23
rcl P24 sto PT rcl V24 sto voltin rcl R24 sto rise_time gsb Calc rcl voltout sto Adj_Elect24
rcl P25 sto PT rcl V25 sto voltin rcl R25 sto rise_time gsb Calc rcl voltout sto Adj_Elect25
rcl P26 sto PT rcl V26 sto voltin rcl R26 sto rise_time gsb Calc rcl voltout sto Adj_Elect26
rcl P27 sto PT rcl V27 sto voltin rcl R27 sto rise_time gsb Calc rcl voltout sto Adj_Elect27
rcl P28 sto PT rcl V28 sto voltin rcl R28 sto rise_time gsb Calc rcl voltout sto Adj_Elect28
```

```
rcl P29 sto PT rcl V29 sto voltin rcl R29 sto rise_time gsb Calc rcl voltout sto Adj_Elect29
rcl P30 sto PT rcl V30 sto voltin rcl R30 sto rise_time gsb Calc rcl voltout sto Adj_Elect30
lbl Calc
rcl voltin sto voltout
rcl Ion_Time_of_Flight rcl PT rcl rise_time + -
x>0 rtn
0 sto voltout
rcl Ion_Time_of_Flight rcl PT -
x<0 rtn
rcl rise_time / rcl voltin *
sto voltout
rtn

seg terminate
```

The geometry file used to simulate the second stage of the accumulator device developed at Swansea was as follows:

```
PA_Define(1400,40,1,C,Y,E,40)
e(0){Fill{within{Box(50,33,1000,34)}}}          ; defining the grounded regions neighbouring
e(0){Fill{within{Box(1005,0,1015,40)}}}         ; the device
locate(100){e(1){include(ShortElec.gem)}}       ; the end electrode of the first stage
locate(106){e(2){include(BigElec.gem)}}         ; the five larger electrodes in the second stage
locate(156){e(3){include(BigElec.gem)}}
locate(206){e(4){include(BigElec.gem)}}
locate(256){e(5){include(BigElec.gem)}}
locate(306){e(6){include(BigElec.gem)}}
```

The ShortElec.gem file consisted of the program instruction:

```
Fill{within {Box(0,8.75,6,24.5)}}
```

The BigElec.gem file consisted of the program instruction:

```
Fill{within {Box(0,20.5,49,24.5)}}
```

The program file for the accumulator pulsing simulations took the general form as shown below, with the programming again being deliberately made quite "long-hand", to aid the user when modifications to the simulation procedure needed to be made, and to allow for easy monitoring of the calculation procedures used.

```
defa voltfivemin 31                ; the bias settings for the penultimate electrode
defa voltfivemax 31                ; before and after pulsing
defa voltsixmin 0                  ; the bias settings for the last electrode in the
defa voltsixmax 139.7              ; accumulator before and after pulsing
defa rise_time_five 3e-3           ; the rise time of the penultimate electrode
defa drop_time_six 3e-3            ; the drop time of the last electrode
defa voltfiveout 0                 ; initialising the voltfiveout parameter
defa voltsixout 0                  ; initialising the voltsixout parameter
defa BunchTime 0                   ; initialising the bunchtime parameter
defa bum 0                         ; initialising the bum parameter
defa rantime 0                     ; initialising the rantime parameter
defa Xlow  268.3                   ; initialising the lowest X position considered
defa Xhigh 268.3                   ; initialising the highest X position considered
defa Ylow  0                       ; initialising the lowest Y position considered
defa Yhigh 5                       ; initialising the highest Y position considered
defa templow  0                    ; initialising the templow parameter
defa temphigh 0                    ; initialising the temphigh parameter
defa temppos  0                    ; initialising the temppos parameter
defa N 1000                        ; initialising the number of particles considered
```

```
ADEFA RanNum 1000 ; "random2.dat"          ; import array of random numbers

seg Initialize
0 sto bum
rcl Ion_Number ARCL RanNum                 ; generate random drift time for particle
0.50 *                                     ; considered
sto rantime

RAND 90 * sto theta                        ; generate randomised angle theta
RAND 90 * sto phi                          ; generate randomised angle phi

lbl sowet
0.025 3.516e5 * SQRT sto vel               ; convert starting energy to a velocity
rcl theta 0.01744444 * sto radthet         ; conversion of theta from degrees to radians
rcl phi 0.01744444 * sto radphi            ; conversion of phi from degrees to radians
rcl radthet COS rcl vel * sto duck
rcl radphi SIN rcl duck * sto Ion_Vx_mm    ; a randomised velocity in the x direction
rcl radthet SIN rcl vel * sto buck
rcl radphi SIN rcl buck * sto Ion_Vy_mm    ; a randomised velocity in the y direction
rcl radphi COS rcl vel * sto Ion_Vz_mm     ; a randomised velocity in the z direction

rcl Xlow sto templow rcl Xhigh sto temphigh gsb randpos rcl tempos      ; calculating the
sto Ion_Px_mm                                                          ; starting position
rcl Ylow sto templow rcl Yhigh sto temphigh gsb yrandpos rcl temppos    ; for the initialised
sto Ion_Py_mm                                                          ; ion

lbl randpos                                ; calculation of the initial starting position in the
rcl temphigh rcl templow - rcl Ion_Number * ; x direction of the ion
rcl N /
rcl templow +
```

```
sto temppos
rtn

lbl yrandpos                          ; calculation of the initial starting position in the
rcl temphigh rcl templow - sto tempdiff   ; y direction of the ion
rcl Ion_Number ARCL RanNum
rcl tempdiff *
rcl templow +
sto temppos
  rtn

seg Init_P_Values                     ; setting the initial biases placed upon the
41.00 sto Adj_Elect01                 ; electrodes
40.00 sto Adj_Elect02
39.00 sto Adj_Elect03
38.00 sto Adj_Elect04
rcl voltfivemin sto Adj_Elect05
rcl voltsixmax sto Adj_Elect06

seg Tstep_Adjust                      ; setting the length of each time step to 50 ps
5e-5 sto Ion_Time_Step

seg Fast_Adjust
rcl Ion_Number ARCL RanNum
0.5 *
sto rantime

rcl Ion_Time_of_Flight rcl rantime - sto dif      ; to check if the ion's time of flight has
rcl dif X<0 goto kyuss                           ; passed the designated drift time
rcl Ion_Time_of_Flight rcl rantime - sto BunchTime
```

```
gsb Calcfive rcl voltfiveout sto Adj_Elect05        ; the calculation of the modified biases
gsb Calcsix rcl voltsixout sto Adj_Elect06          ; to be placed on the electrodes
goto kyuss

lbl calcfive
rcl BunchTime rcl rise_time_five -
x>0 gsb dope
rcl BunchTime rcl rise_time_five -
x>0 rtn
rcl BunchTime rcl rise_time_five / sto wizard
rcl voltfivemax rcl voltfivemin -
rcl wizard *
rcl voltfivemin +
sto voltfiveout
rtn

lbl calcsix
rcl BunchTime rcl drop_time_six -
x>0 gsb throne
rcl BunchTime rcl drop_time_six -
x>0 rtn
rcl BunchTime rcl drop_time_six / sto electric
rcl voltsixmax rcl voltsixmin -
rcl electric *
-1 *
rcl voltsixmax +
sto voltsixout
rtn

lbl dope
```

```
rcl voltfivemax sto voltfiveout
rtn

lbl throne
rcl voltsixmin sto voltsixout
rtn

lbl kyuss

seg Other_Actions
305 rcl Ion_Px_mm X<Y GSB resetbum          ; resetting the bum flag when the ion is ejected
rcl Ion_Px_mm 855 X<Y GSB midelectrode      ; activating the time of flight output
goto missit

lbl resetbum
0 sto bum
rtn

lbl midelectrode
rcl bum 1 X<=Y rtn
rcl Ion_Time_of_Flight MESS ;TOF #
1 sto bum
rtn

lbl missit

seg terminate
0 sto tempnum
lbl whirlpool                               ; the output of the random numbers used
rcl tempnum 1 + sto tempnum
```

```
rcl tempnum ARCL RanNum

0.5 *

MESS ;rantime #

rcl tempnum 1000 X<Y goto outplease

goto whirlpool


lbl outplease
```

References

- Amoretti, M. *et al.*, (the ATHENA collaboration). (2002). *Nature (London).* **419**, 456.
- Amoretti, M. *et al.*, (the ATHENA collaboration). (2004). *Nuc. Instrum. Meth. A* **518**, 679.
- Anderson, C. D. (1933). *Phys. Rev.* **43**, 491.
- Bell, R. E. and Graham, R. L. (1953). *Phys. Rev.* **90**, 644.
- Blackett, P. M. S. and Occhialini, G. P. S. (1933). *Proc. Roy. Soc. (London) A* **139**, 699.
- Branauer, S., Emmett, P. H. and Teller, E. J. (1938). *Am. Chem. Soc.*, **60**, 309.
- Branauer, S., Copeland, L. E. and Kantro, D. L. (1967). In *The Solid-Gas Interface (vol. 1)*, ed. E. Alison Flood (Edward Arnold Publishers Ltd., London) pp. 77-103.
- Canter, K. F., Coleman, P. G., Griffith, T. C. and Heyland, G. R. (1972). *J. Phys. B: At. Mol. Phys.* **5**, L167.
- Canter, K. F., Mills Jr., A. P. and Berko, S. (1974). *Phys. Rev. Lett.* **33**, 1 7.
- Charlton, M. (1998). *Nucl. Instrum. Meth. B* **143**, 11.
- Charlton, M. and Humberston, J. W. (2001). *Positron Physics* (Cambridge University Press).
- Cherry, W. H. (1958). Ph.D. Dissertation, Princeton University.
- Coleman, P. G. (2000). ed. *Positron Beams and their Applications* (World Scientific).
- Coleman, P. G. (2002). *Nucl. Instr. and Meth. In Phys. Res. B* **192**, 83-89.

- Dahl, D. A. (2000). *SIMION v7.0*, MS 2208, Idaho National Engineering and Environmental Laboratory, P.O. Box 1625, Idaho Falls, ID 83415.
- DeBenedetti, S., Cowan, C. E. and Konneker, W. R. (1949). *Phys. Rev.* **76**, 440.
- DeBenedetti, S., Cowan, C. E., Konneker, W. R. and Primakoff, H. (1950). *Phys. Rev.* **77**, 205.
- Debye, P. and Hückel, E. (1923). *Physikalische Zeitschrift.* **24**, 9, 185.
- Deutsch, M. (1951a). *Phys. Rev.* **82**, 455.
- Deutsch, M. (1951b). *Phys. Rev.* **83**, 866.
- Dirac, P. A. M. (1930). *Proc. Roy. Soc. Lond. A.* **126**, 360.
- DuMond, J. M. W., Lind, D.A. and Watson, B. B. (1949). *Phys. Rev.* **75**, 1226.
- Frieze, W. E., Gidley, D. W. and Lynn, K. G. (1985). *Phys. Rev. B* **31**, 5628.
- Gabrielse, G. *et al.*, (the ATRAP collaboration). (2002). *Phys. Rev. Lett.* **89**, 213401.
- Ghosh, P. K. (1995). *Ion Traps* (Clarendon Press, Oxford).
- Greaves, R. G. and Surko, C. M. (1996). *Can. J. Phys.* **74**, 445.
- Greaves, R. G. and Surko, C. M. (2000). *Phys. Rev. Lett.* **85**, 1883.
- Greaves, R. G. and Surko, C. M. (2001). *Phys. Plasmas* **8**, 1879.
- Griffiths, B. (2005). Ph.D. Dissertation (in preparation), University of Wales Swansea.
- Huang, X., Anderegg, F., Hollmann, E., Driscoll, C. and O'Neil, T. (1997). *Phys. Rev. Lett.* **78**, 875.
- Hugenschmidt, C., Straßer, B. and Schreckenbach, K. (2002). *Appl. Surf. Sci.* **194**, 283.
- Hulett Jr., L. D., Donohue, D. L. and Lewis, T. A. (1991). *Rev. Sci. Instrum.* **62**, 2131.

- Iwata, K., Greaves, R. G., Murphy, T. J., Tinkle, M. D. and Surko, C. M. (1995). *Phys. Rev. A* **51**, 473.
- Jääskeläinen, J., Laine, T., Fallström, K., Saarinen, K. and Hautojärvi, P. (1997). *Appl. Surf. Sci.* **116**, 73.
- Joliot, F. (1933). *Compt. Rend.* **197**, 1622.
- Joliot F. (1934). *Compt. Rend.* **198**, 81.
- Khatri, R., Charlton, M., Sferlazzo, P., Lynn, K. G., Mills Jr., A. P. and Roellig, L. O. (1990). *Appl. Phys. Lett.* **57**, 2374.
- Klemperer, O. (1934). *Proc. Cambridge Phil. Soc.* **30**, 347.
- Langmuir, I. (1918). *J. Am. Chem. Soc.*, **40**, 1361.
- Malmberg, J. H. and deGrassie, J. S. (1975). *Phys. Rev. Lett.* **35**, 577.
- Marler, J. P., Barnes, L. D., Gilbert, S. J., Sullivan, J. P., Young, J. A. and Surko, C. M. (2004). *Nucl. Instrum. Meth. B* **221**, 84.
- Massoumi, G. R., Hozhabri, N., Lennard, W. N., Schultz, P. J., Baert, S. F., Jorch, H. H. and Weiss, A. H. (1991). *Rev. Sci. Instrum.* **62**, 1460.
- Matsumoto, T., Chiba, M., Hamatsu, R., Hirose, T., Yang, J. and Yu, J. (1996). *Phys. Rev. A* **54**, 1947.
- Merrison, J. P., Charlton, M., Deutch, B. I. and Jørgensen, L.V. (1992). *J. Phys.: Condens. Matter* **4**, L207.
- Merrison, J. P., Charlton, M., Deutch, B. I. and Jørgensen, L.V. (1993). *Hyperfine Interactions* **76**, 305.
- Merrison, J. P., Charlton, M., Aggerholm, P., Knudsen, H., van der Werf, D. P., Clarke, J. and Poulsen, M. R. (2003). *Rev. Sci. Instrum.* **74**, 3284.
- Mills Jr., A. P. (1980). *Appl. Surf. Sci.* **22**, 273.

- Mills Jr., A. P. (1983). In *Positron Solid-State Physics, Proc. Int. School of Physics 'Enrico Fermi', Course 83*, ed. W. Brandt and A. Dupasquier (North-Holland) pp. 432.
- Mills Jr., A. P. and Gullikson, E. M. (1986). *Appl. Phys. Lett.* **49**, 1121.
- Mills Jr., A. P. (2002). *Nucl. Instrum. Meth. B* **192**, 107.
- Mohorovičić, S. (1934). *Astron. Nachr.* **253**, 93.
- Murphy, T. J. and Surko, C. M. (1992). *Phys. Rev. A* **46**, 5696.
- Niebel, K. F. and Venables, J. A. (1976). In *Rare Gas Solids (vol. 1)*. ed. M. L. Klein and J. A. Venables (Academic Press Inc., London) pp. 558.
- Nutt, R. (2002). *Mol. Imag. Biol.* **4**, 11.
- Oberthaler, M. K. (2002). *Nucl. Instrum. Meth. B* **192**, 129.
- Schultz, P. J. and Lynn, K. G. (1988). *Rev. Mod. Phys.* **60**, 3, 701.
- Stoeffl, W., Asoka-Kumar, P. and Howell, R. (1999). *Appl. Surf. Sci.* **149**, 1.
- Surko, C. M., Passner, A., Leventhal, M. and Wysocki, F. J. (1988). *Phys. Rev. Lett.* **61**, 1831.
- Surko, C. M., Leventhal, M. and Passner, A. (1989). *Phys. Rev. Lett.* **62**, 901.
- Surko, C. M. and Greaves, R. G. (2003). *Rad. Phys. and Chem.* **68**, 419.
- Sutton, L. E. (1965). (ed.) in *Table of interatomic distances and configuration in molecules and ions*, Supplement 1956-1959, Special publication No. 18, Chemical Society, London, UK.
- Thibaud, J. (1933). *Compt. Rend.* **197**, 1629.
- Thibaud, J. (1934). *Phys. Rev.* **45**, 781.
- Triftshäuser, W., Kögel, G., Sperr, P., Britton, D. T., Uhlmann, K. and Willutzki, P. (1997). *Nucl. Instrum. Meth. B* **130**, 264.

- Vallery, R. S., Zitzewitz, P. W. and Gidley, D. W. (2003). *Phys. Rev. Lett.* **90**, 203402.
- van der Werf, D. P. *et al.*, (the ATHENA collaboration). (2003). In *Non-Neutral Plasma Physics V*, edited by M. Schauer, T. Mitchell, and R. Nebel, AIP Conference Proceedings 692, American Institute of Physics, New York, p. 172.
- Weng, H. M., Ling, C. C., Hui, I. P., Beling, C. D. and Fung, S. (2002). *Appl. Surf. Sci.* **194**, 24.
- Wolfenstein, L. and Ravenhall, D. G. (1952). *Phys. Rev.* **88**, 279.
- Xu, J., Suzuki, R., Hulett Jr., L. D. and Lewis, T. A. (1997). *Appl. Surf. Sci.* **116**, 34.
- Yang, C. N. (1950). *Phys. Rev.* **77**, 242.

Bibliography

- *Films on Solid Surfaces,* J. G. Dash (Academic Press Inc., London, 1975).
- *Free atoms and the simplest atomic crystals*, A. M. Ratner, *Physics Reports* **269** (1996) pp. 197-332.
- *Fundamentals of Physics Extended (Fifth Edition)*, ed. D. Halliday, R. Resnick and J. Walker (John Wiley and Sons, Inc., 1997).
- *Non-Neutral Plasma Physics V*, ed. M. Schauer, T. Mitchell, and R. Nebel (AIP Conference Proceedings 692, American Institute of Physics, New York, 2003).
- *Positron Annihilation*, ed. A. T. Stewart and L. O. Roellig (Academic Press Inc., London, 1967).
- *Positron Beams and their applications*, ed. P. Coleman (World Scientific, 2000).
- *Positron Physics*, M. Charlton and J. W. Humberston (Cambridge University Press, 2001).
- *Rare Gas Solids (vol. 1)*, ed. M. L. Klein and J. A. Venables (Academic Press Inc., London, 1976).
- *The Interaction of Gases with Solid Surfaces (The International Encyclopedia of Physical Chemistry and Chemical Physics, Topic 14, Volume 3)*, W. A. Steele (Pergamon Press Ltd., 1974).
- *The Solid-Gas Interface (volume 1)*, ed. E. Alison Flood (Edward Arnold Publishers Ltd., London, 1967).
- *The Wordsworth Dictionary of Science and Technology*, Wordsworth Editions Ltd., 1995.